

# DISSERTATION

## **Vanadium and palladium surface oxides: A structural analysis**

*ausgeführt zum Zwecke der Erlangung des akademischen Grades eines Doktors der  
technischen Wissenschaften unter der Leitung von*

**Ao. Univ. Prof. Dr. Peter Varga**

E 134

Institut für Allgemeine Physik, Technische Universität Wien

*eingereicht an der*

*Technischen Universität Wien*

*Fakultät für Technische Naturwissenschaften und Informatik*

*von*

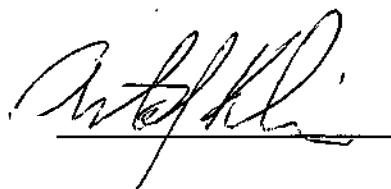
**Dipl.-Ing. Christof Klein**

Matr.-Nr.: 9225760

Bastiengasse 40/9

A-1180 Wien

Wien, am 28. Mai 2003



## Kurzfassung

Trotz der Tatsache, dass Palladium als vielversprechender Katalysator für Abgase von Verbrennungsmotoren gilt, sind überraschend wenige Informationen über die strukturellen Details der verschiedenen Phasen, die sich während eines Oxidationsprozesses auf Palladiumoberflächen bilden, verfügbar. So wurden zum Beispiel einige ungewöhnliche Effekte bei der mittels Pd katalysierten Oxidation von CO beobachtet, die zunächst dem periodischen Auffüllen/Entleeren von Sauerstoffplätzen unter der Oberfläche zugeschrieben wurden, was sich im Laufe dieser Arbeit als eher zweifelhaft herausstellte. Um ein wenig Licht in das Dunkel der bisher wenig verstandenen Abläufe bei mittels Pd katalysierten Reaktionen zu bringen wurde daher die Oxidation von Pd(III) Oberflächen mittels Rastertunnelmikroskopie (STM), Beugung niederenergetischer Elektronen (LEED) und oberflächensensitiver Röntgenbeugung (SXR) näher untersucht.

Bei Raumtemperatur führt das Dosieren von molekularem Sauerstoff immer zur Ausbildung einer chemisorbierten  $(2 \times 2)$  Überstruktur sobald die Sättigungsbedeckung von 0.25 ML erreicht ist. Es stellte sich heraus, dass sich in diesem Fall alle Sauerstoffatome in dreifach-koordinierten fcc Muldenplätzen befinden. Höhere Sauerstoffbedeckungen konnten allerdings nur bei höheren Temperaturen und einem Sauerstoffhintergrunddruck von mehr als  $4 \times 10^{-6}$  mbar erreicht werden. Nach Dosierung von 5000 Langmuir (L)  $O_2$  bei  $320^\circ C$  wurde schließlich die Bildung eines inkommensurablen, zweidimensionalen Oberflächenoxids entdeckt. Das Beugungsbild dieser neuartigen Phase ist komplex und konnte als das Ergebnis einer Superposition von drei äquivalenten Domänen einer quadratischen Überstruktur auf einem hexagonalen Substrat identifiziert werden. Die Seitenlänge einer quadratischen Einheitszelle konnte mittels STM und LEED zu 6.74 Å bestimmt werden. Des Weiteren stellte sich heraus, dass eine Diagonale kommensurabel bezüglich des Substrats ausgerichtet ist, während die andere inkommensurabel ist. Dieses Oberflächenoxid konnte sowohl durch die Dosierung von 20 L CO gefolgt von kurzzeitigem Erwärmen auf  $150^\circ C$ , als auch durch längeres Ausheizen im Ultrahochvakuum bei  $400^\circ C$  vollständig reduziert werden. Dabei entstanden hexagonale, eine Monolage tiefe, Löchern in der Oberfläche, die eine direkte Folge der reduzierten Pd-Dichte des Oberflächenoxids waren. Dies wiederum ermöglichte die experimentelle Bestimmung der Anzahl der Palladiumatome pro Überstrukturzelle. Während des Reduktionsvorganges konnte die Koexistenz des Oberflächenoxids mit der chemisorbierten  $(2 \times 2)$  Phase in mehreren STM-Bildern beobachtet werden, was sich gut mit einem Desorptionsmechanismus vereinbaren läßt, bei dem die Desorption vorzugsweise von der  $(2 \times 2)$  Phase stattfindet, während das Oberflächenoxid ausschließlich als Sauerstofflieferant dient. Letztendlich war die exakte Strukturbestimmung des Oberflächenoxids allerdings nur auf Grund der Zusammenarbeit aller

oben erwähnter Methoden und der zusätzlichen Berücksichtigung von Resultaten aus Dichtefunktionaltheorie(DFT)-Rechnungen möglich. Das Ergebnis wird sowohl durch die ausgezeichnete Übereinstimmung zwischen der durch SXRD ( $\chi^2 = 0.48$ ) und der durch DFT bestimmten Struktur, als auch durch den optischen Vergleich der simulierten und gemessenen STM-Bilder bestätigt. Eine quadratische Elementarzelle des Oberflächenoxids besteht demnach aus 5 Pd- und 4 O-Atomen, welche zwei weitere Quadrate in der Zelle bilden, die wiederum um  $45^\circ$  gegeneinander verdreht sind. Die Atome liegen dabei fast koplanar und bilden dementsprechend ein zweidimensionales Oberflächenoxid, das sich von allen bekannten Festkörperoxiden von Pd unterscheidet. Dieses zweidimensionale Oxid könnte allerdings unter realistischen Arbeitsbedingungen eines Pd-Katalysators eine wichtige Rolle spielen, da es eine thermodynamisch stabile Phase zwischen der (2 x 2) Sauerstoffüberstruktur und dem Festkörperoxid PdO darstellt.

In dieser Arbeit wurde aber auch eine zweite Art von Oberflächenoxiden untersucht und zwar ultradünne Vanadiumoxidstrukturen, die sich auf Pd(111) Oberflächen ausbilden können. Dieses System ist vor allem deswegen interessant, weil es ein Modellsystem für einen "inverse strong metal support interaction" (SMSI) Katalysator darstellt und sehr interessante Eigenschaften - im Speziellen im Bereich geringer Bedeckungen - aufweist. Es wurde gefunden, dass das Aufdampfen von Vanadium in einem Sauerstoffhintergrunddruck von  $2 \times 10^{-7}$  mbar und bei einer Proben temperatur von  $250^\circ\text{C}$  zunächst zur Ausbildung einer nicht-periodischen, wabenförmigen Struktur führt, die von den Stufenkanten zu wachsen beginnt und sich ab einer Bedeckung von ca. 0.2 ML in eine geordnete Phase umzuwandeln anfängt. Bei 0.31 ML ist schließlich die gesamte Oberfläche mit dieser perfekt geordneten, sehr offenen, p(4 x 4) Struktur bedeckt. Das Ausheizen dieser Struktur in  $\text{H}_2$  Atmosphäre transformiert sie in ein geordnetes  $\text{V}_2\text{O}_3$  Oberflächenoxid, das eine (2 x 2) Periodizität aufweist und dessen optimale Oberflächenbedeckung bei 0.5 ML erreicht ist. Es wurden zunächst Modelle für die beiden geordneten Strukturen basierend auf Ergebnisse von ab initio DFT Rechnungen erstellt, die letztendlich im Rahmen dieser Arbeit eindeutig durch quantitative LEED Analysen bestätigt wurden. Es stellte sich heraus, dass in der hochsymmetrischen, sauerstoffreichen p(4 x 4) Phase jedes Vanadiumatom von 4 Sauerstoffatomen in einer ungewöhnlichen tetragonalen Koordination umgeben ist. Diese spezielle Koordination erlaubt es dem Oxid offene zwei- bzw. eindimensionale Strukturen auszubilden, die durch die Wechselwirkung zwischen Substrat und Oxid stabilisiert werden. In dieser Hinsicht können auch die nicht-periodischen Strukturen, die sich im Bereich niedriger Bedeckungen ausbilden, mittels Verkettung der oben beschriebenen tetragonalen Einheiten aufgebaut werden. Die katalytischen Eigenschaften eines solchen unkonventionell koordinierten p(4 x 4) Netzwerkes bzw. der  $\text{VO}_4$  Einheiten sind allerdings noch unbekannt und erfordern weitere Untersuchungen.

thermodynamically stable, intermediate phase between an oxygen overlayer and the bulk oxide PdO.

The second type of surface oxides investigated in this work concerns vanadium oxides grown on Pd(111), which represent a model system for an inverse strong metal support interaction (SMSI) catalyst and show very interesting properties especially in the low coverage regime. Evaporation of V at an oxygen background pressure of  $2 \times 10^{-7}$  mbar and elevated sample temperature (250 °C) was found to result in the formation of a non-periodic honeycomb-like structure growing from the steps, which starts to transform into an ordered phase at a vanadium coverage of  $\sim 0.2$  ML. At 0.31 ML the entire surface is covered by this well ordered open p(4 x 4) structure. Annealing this structure in H<sub>2</sub> atmosphere transforms the phase into a V<sub>2</sub>O<sub>3</sub> surface oxide with (2 x 2) periodicity, whose optimal coverage is reached at 0.5 ML. Models for both ordered structures have been suggested as a result of molecular dynamics simulations based on ab initio DFT calculations and are unambiguously confirmed by quantitative LEED analyses in the present work. In the oxygen rich, highly symmetric, p(4 x 4) phase, the V atoms were found to be surrounded by 4 oxygen atoms in an unusual tetrahedral coordination. This tetrahedral coordination allows the oxide to adopt open loosely packed 2D and 1D structures, which are stabilized by the surface-oxide interface energy. In this respect, also the non-periodic structures observed in the ultra-low coverage regime can be constructed using the above described building blocks. The catalytic properties of the unconventionally coordinated p(4 x 4)-V<sub>5</sub>O<sub>14</sub> network and the VO<sub>4</sub> units in particular, however, are still unknown and have to be investigated in the future.

## 1 Introduction

One of the most important motivations for research in surface science is certainly heterogeneous catalysis, i.e. a solid catalyst mediating and facilitating reactions between adsorbed molecules [1]. Actually, most of today's chemical or pharmaceutical products can only be obtained by the use of appropriate catalysts. Prominent examples for the application of heterogeneous catalysis in industrial processes are e.g. the synthesis of ammonia or sulfuric acid. But also in environmental chemistry, applied for example in automotive combustion, catalysis plays a crucial role. Modern, industrial catalysts, however, are very complex, usually consisting of metal particles finely dispersed on an oxidic substrate (powder) of rather poorly known composition and morphology. Consequently, in order to obtain some knowledge on the interaction of adsorbates with the surface, the modification of their properties due to adsorbate-surface interactions and interactions between adsorbed molecules, and therefore an understanding of technologically important catalytic processes, one has to start at first by treating simple model systems, as e.g. single crystals of the metal in use. Of course, since various crystal planes of different orientation occur in real catalysts, such model systems are only crude approximations of the real situation. This discrepancy is often called "material gap". Although there are several experimental techniques available, which are suitable for investigating the above described model systems, another drawback has to be dealt with: Most of these methods can only be applied in ultra high vacuum (UHV) chambers with base pressures below  $10^{-9}$  mbar. This "pressure gap" between the experimental situation and real working-conditions for catalysts, which are at atmospheric pressure or even higher, extends over  $\sim 10$  orders of magnitude and consequently further separates the analyzable systems from the ones encountered in reality. Nevertheless, vital information on basic, but important, reaction mechanisms as well as on the electronic and structural properties of metal surfaces can be obtained already from rather "simple" systems. However, as a consequence of this situation, the catalytic activity of metal surfaces has been attributed to the clean metal regions, ignoring the influence of oxides that might form under realistic conditions.

In contrast to the extensive research performed on metal and semiconductor surfaces, comparatively few works have been done on oxide surfaces [2]. Nevertheless, oxide surfaces are more relevant than metal surfaces for a number of important processes that occur in the terrestrial environment, since the oxidizing effect of ambient air typically causes the vast majority of all "real-world" metals to be covered by a thin film of a native oxide. In these cases, it is the oxide skin that governs the surface reactivity of the metal rather than the surface properties of the metal itself, contrary to the assumption made above. Furthermore, certain oxides are - as already mentioned - also used as support for metal catalysts. The metal/oxide interfacial interactions that occur in

such structures can have profound effects on the performance of the catalyst as in the strong metal support interaction (SMSI) effect [3]. The reasons, however, why, despite of their fundamental importance, oxide surfaces have not been studied in greater detail so far, are manifold. First of all, it is not easy to prepare a homogeneous, high-quality oxide surface consisting of just one ordered phase. Second of all, the insulating nature of oxides causes some problems for some of the most common experimental techniques, such as e.g. electron spectroscopies and scanning tunneling microscopy (STM). Third of all, oxidic surface structures are in the majority of cases highly complex, requiring very large unit cells for a correct description, additionally complicating the situation. Last but not least, due to the high oxygen partial pressure needed for the formation of some of the oxides encountered in reality, such oxides are very hard to prepare in conventional setups used in surface science.

In any case, for a thorough understanding of the catalytic properties of a metal/metal-oxide, a detailed knowledge of the atomic structure is indispensable. A very good example, confirming this statement, concerns the catalytic activity of palladium. Although it is rather well-known that Pd is a very promising candidate for a three-way catalyst in automotive combustion, especially due to its ability to operate at higher temperatures (closer to the exhaust manifold) compared to conventional Pt/Rh catalysts [4], some strange effects in its catalytic behavior have delayed implementation so far. Since in catalytic converters, the key reactions include the complete oxidation of any hydrocarbon in the exhaust gas stream as well as the simultaneous oxidation of CO and reduction of NO, high and stable catalyzing properties for these reactions are required. At high oxygen to CO/CH<sub>4</sub> ratios, however, not understood oscillations in the CO/CH<sub>4</sub> oxidation rates have been discovered for Pd-catalyzed reactions [5]. Obviously, these phenomena have to be caused by some unknown, oxygen-induced changes and have been attributed to the periodic filling and depletion of subsurface oxygen by several groups [6, 7]. This model, however, has been challenged in the following [8] and eventually proved wrong for Pd(110), where the oscillations have been found to be caused by the formation and deformation of palladium oxide [9]. In other words, changes in the surface structure are responsible for the observed, peculiar catalytic behavior. Due to this finding and due to the fact that even less information was available concerning Pd(111) surfaces, an intensive structural analysis of different phases encountered in the oxidation process of Pd(111) was started and the obtained results are presented in this work, including the description of a novel, strictly two-dimensional surface oxide, that shows no resemblance to any bulk oxide of palladium, but can, nevertheless, play a role in real Pd-catalysts.

The other main topic of this work, however, deals with ultrathin vanadium oxide layers that can form on a Pd(111) surface under appropriate conditions. Vanadium oxide is known to be a very versatile catalyst mainly due to vanadium's wide range of possible

very well. Using this additional information it was therefore possible to experimentally confirm the structure model proposed by DFT. The sixth chapter deals with vanadium surface oxides grown on Pd(111), starting with the discussion of rather unordered, non-periodic phases at very low vanadium coverages, followed by a thorough analysis of two very well ordered phases, i.e. a  $p(2 \times 2)$  and a  $p(4 \times 4)$  phase. Also in this case the parameter space had to be considerably reduced at first in order to be able to perform a quantitative LEED analysis (especially for the highly complex  $p(4 \times 4)$  structure). This was again achieved by testing only some variations of a structural model proposed by DFT. Finally, in the last chapter a summary of the obtained results is presented and some of the gained insights on the special structural properties of surface oxides and their possible influence on catalysis are discussed.

This work is a result of the Joint Research Program "Gas-Surface Interactions", which was supported by the Austrian Science Foundation (project S81).

## 2 Low energy electron diffraction (LEED)

### 2.1 The development of LEED to a standard tool in surface science

One of the first successful experimental validations of predictions made by the, at those days very controversial, quantum theory were done by Davisson and Germer [12] in the 1920s, already involving the diffraction of low-energy electrons from the surface of a, more or less, single-crystalline solid. This direct demonstration of the wave-particle duality of electrons paved the ground for the general acceptance of quantum mechanics. Although it was quickly realized that scattered electrons of an incident energy between  $\approx 20$  and 600 eV carry a lot of information concerning the atomic structure of the surface region, due to their rather small penetration depth of 5-10 Å, several difficulties had to be overcome until quantitative LEED got applicable. The reasons for that were manifold. Firstly, a lot of experimental problems became obvious. The preparation of a clean, reproducible, single-crystalline surface was the first obstacle that had to be surmounted. Moreover, due to the strong interaction of low-energy electrons with matter, the space between the electron source and the target had to be evacuated. However, the most demanding requirement concerning the vacuum quality stemmed from the fact that the sample under consideration had to stay free from contaminations for the whole duration of the measurement. To ensure that, an ultra high vacuum (UHV) chamber, operating at a residual gas pressure below  $10^{-10}$  mbar, was necessary, which was not available until the 1960s. Secondly, the theoretical description of a conventional LEED experiment turned out to be very difficult. Although X-ray diffraction theory was well established at this time, its adaptation to LEED was doomed to fail. It turned out that multiple scattering of those low energetic electrons had to be taken into account to enable a theoretical understanding of the experimental results. This led, in contrast to the existing kinematic theories, to the development of dynamical theories, incorporating all the consequences resulting from the large cross-section of the electron-atom scattering. Important ingredients of a successful LEED-theory were an atomic scattering potential represented by a  $t$ -matrix, an inelastic mean free path (realized by the introduction of an imaginary component of the scattering potential) and a temperature correction. Different formalisms, which included those ingredients, resulted in an essentially good agreement with experiment and - even more importantly - a very similar atomic structure [13, 14]. Having working theories established started the era of structure determination by LEED in the 1970s. A lot of effort was put into streamlining and speeding up of the computational codes, enabling the treatment of semiconductors, alloys and even adsorbates. As the computing power increased larger unit cells and therefore more complex structures became theoretically feasible. How-

ever, due to the measurement of intensities in the LEED experiments and the involved loss of essential phase information, it is not possible to retrieve the investigated crystal structure directly from the experimental results. The crucial point of every quantitative LEED analysis is therefore a comparison of the theoretical outcome of a trial-structure calculation with the according experiment, which is done by means of a reliability factor (short: *R*-factor) [15, 16] measuring the quality of agreement. One obvious result of the increasing complexity of the investigated structures was that the corresponding number of structural parameters increased accordingly, causing an overwhelming amount of possible trial-structures. To tackle that problem the tensor-LEED method was developed [17, 18], which basically uses one trial-structure as reference, treating minor deviations from the reference structure as perturbations. This tensor-LEED method helped to reduce the computational costs considerable, allowing the structure determination of very complex structures by using automated search-algorithms probing a given parameter space. Eventually, LEED was established as the standard tool for structure determination in modern surface science.

## 2.2 The LEED experiment

### 2.2.1 General aspects

As described above, several preconditions have to be fulfilled in order to be able to conduct a high quality LEED experiment. The most important basic equipment is an UHV chamber which is maintained at pressures well below  $10^{-10}$  mbar. This is an indispensable prerequisite since a typical LEED measurement takes about 45 min and within this time no change of the investigated surface due to adsorption from the residual gas is acceptable. Secondly, the crystal under consideration has to be of sufficient quality. That means it has to be oriented well within  $1^\circ$  of the desired crystallographic orientation and cleaned by standard procedures used in surface science to get rid of impurities and defects (cf. Sec. 4.2). This crystal has to be mounted on a high-precision manipulator for optimal positioning with a precision of at least  $\pm 0.1^\circ$  with respect to the electron gun. The e-gun in use has to be capable of maintaining a steady, low beam current ( $\approx 10^{-9}$  A) and to accelerate the emitted electrons to energies between 30 and 600 eV - a higher beam flux could modify the surface structure, for example by dissociating molecular overlayers. Since low-energy electrons can easily be deflected by the magnetic field of the earth, this field has to be either compensated by a set of Helmholtz coils or, as in the chamber used throughout this work, isolated by a  $\mu$ -metal shield. Last but not least a display system is needed to visualize the obtained LEED pattern, which is realized in our case by a 2-grid retarding-field energy analyzer from which the elastically scattered electrons are accelerated towards a fluorescent

lying in the surface plane (Fig. 2.2.3). A rotation about the surface normal was not possible. Due to this fact symmetry among diffracted beams could only be achieved by aligning the angle of incidence parallel to the surface normal. Although a high symmetry is very desirable, due to its facilitation of the dynamical calculations and the experimental advantage of being able to average over equivalent beams, there was also another reason for performing all the LEED experiments at normal incidence: Using this setup it was simply not possible to determine any other angle with sufficient accuracy.

Out of three variable parameters the distance between the sample and the screen was the least sensitive and important one and kept constant for every measurement. The horizontal angle of the sample, however, was very critical and had to be adjusted within  $\pm 0.1^\circ$ . Also the vertical orientation had to be as perfect as possible. A preliminary positioning of the sample could already be done shortly after the final preparation step, but due to the sensitivity of the manipulator to temperature variations, the final adjustment had to be made at a sample temperature close to the designated temperature of measurement. In the case of a perfectly mounted sample a rotation about the surface normal would just cause the diffraction image to turn accordingly, which would bear the advantage of being able to move certain beams out of the shadow of the e-gun, but this additional degree of freedom is by no means a necessity for a LEED measurement at normal incidence.

During the actual positioning process several symmetry equivalent beams were monitored at a certain energy of the incident electrons. Since those beams should show the same intensities at all energies, the angles were changed until a nearly perfect agreement was obtained. This process worked best when the most sensitive energies, with regard to the influence of the position of the sample on the monitored beams, were chosen for optimization. Most of the time one is not able to guess the optimal positioning energies during the first alignment procedure, but they can easily be extracted from the data of a complete LEED measurement. Accordingly, a second run after a re-optimization of the sample position is strongly recommended.

#### **2.2.2.2 Measurement**

After sample preparation and positioning, the measurement itself runs completely computer controlled. Every diffraction pattern is stored as an 8-bit image, resulting in an image-stack of  $\sim 150$  MB. The chosen energy range and the desired energy step width are the only essential parameters that have to be given to the program. Before starting a measurement, however, one should make sure that the highest intensity of every beam stays below 255 (cf. 8-bit resolution), since otherwise saturation effects occur, which

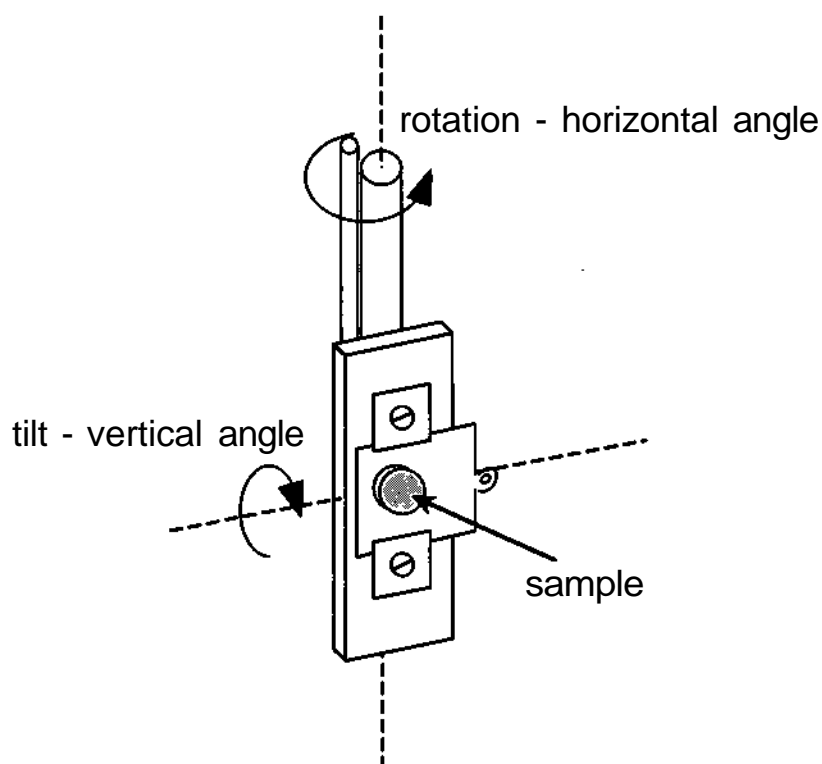


Figure 2.2.3: Schematic of the manipulator and its degrees of freedom.

inevitably lead to a loss of information. Sometimes it can be reasonable to exceed the resolution range given by the camera, though. This is the case if one wants to investigate very weak superstructure beams, which would otherwise be hard to evaluate. By performing two measurements - a normal one optimized for the basic beams and an overexposed one for the superstructure beams - the actual resolution of the camera is virtually increased, thus improving the quality of the analysis.

The big advantage of video-LEED is the availability of every experimental detail of the measurement at any subsequent time, making an optimization of the data evaluation procedure possible.

### 2.2.3 Data evaluation

For the extraction of the final  $I$ - $V$  spectra out of the data obtained by a video-LEED measurement, a macro written for the image processing software NIH Image was used. This LEED-macro automatically recorded the  $I$ - $V$  curves for every desired beam depending on some input parameters. Although the next few paragraphs are devoted to the evaluation of the experimental results, only the basic ideas are presented, since a

detailed description of the functionality of this routine can be found elsewhere [19].

### 2.2.3.1 Beam tracing and intensity determination

In order to automatically gain the energy dependent intensity (in other words the  $I$ - $V$  spectrum) of every single visible beam, one has to know the position of each spot in all the images of a given LEED-stack. To accomplish that, some characteristic properties of electron diffraction are used. Firstly, due to the 2-dimensional translational periodicity of the surface of a single crystal every beam can be directly related to a vector of the according 2-dimensional reciprocal lattice (cf. Sec. 2.3) and therefore characterized by a pair of Miller indices ( $hk$ ). Consequently, the definition of the position of four integer order beams (reflections caused by the substrate) in one arbitrary LEED-image is sufficient to extrapolate all other beam positions for that particular diffraction pattern, as long as the instrumental errors are taken into account. In case of a superstructure, the type of reconstruction (i.e. the periodicity with respect to the basic lattice) contains all the additional information needed to calculate the according beam positions as well. Secondly, due to the energy-momentum relation every beam moves, with increasing energy, directly towards the specular reflex (00). The distance between an arbitrary beam and the specular reflex thereby changes proportional to  $1/\sqrt{E}$ . The tracing algorithm therefore always predicts the beam positions in the successive image at first, checks within a predefined radius for the highest intensity and chooses the right positions following some sophisticated rules, including the consideration of other symmetry equivalent beam positions, the intensity level with respect to the background and the positions of the other integer order beams. This procedure nearly totally eliminates the occurrence of artifacts caused by incorrect beam-tracing, for example due to some inhomogeneities of the fluorescent screen.

Although tracing of the beams is an important part of the data evaluation process, the according determination of the correct intensities is even more crucial for the success of the analysis. For the optimization of this determination two parameters were available. The first parameter defined the radius of integration around a given beam-center. The second one had to be a slightly larger radius, since the difference between those two parameters defined the area within which the background intensity was integrated. The subtraction of the mean background intensity from the mean beam intensity resulted in the final intensity value. Since Pendry's  $R$ -factor was used throughout this work the absolute intensity values did not matter, but the regions of zero intensity had to be determined with the highest possible accuracy, due to their valuable structural information and their influence on the  $R$ -factor. Hence it was important to obtain the best possible local background values. Of course beams at the very border of the LEED screen or close to the shadow of the e-gun were omitted in the evaluation procedure,

since their analysis, following the procedures described above, would have resulted in unphysical intensities.

### 2.2.3.2 Data processing

After the determination of the intensities of all chosen beams for every image of the measurement, the resulting  $I$ - $V$  spectra have to be analyzed. Since every measurement is prone to some noise, this is especially true for the evaluation of the  $I$ - $V$  curves of some low-intensity reflexes. Of course this problem can be reduced by some experimental techniques like the previously described performance of an additional over-saturated measurement and the use of a post-measurement image processing macro (cf. Sec. 2.2.4). Also the implementation of a camera with higher resolution and light sensitivity would lead to a further noise reduction. However, one can never completely get rid of some residual noise. Consequently, the  $I$ - $V$  curves of all symmetry equivalent beams were averaged at first. After this step the spectra of beams with a high signal to noise ratio could already be used for a comparison with calculated results. For low-intensity reflexes, however, further treatment is necessary, since the noise-amplitudes are partly larger than the corresponding "true" signals. Nevertheless, those noisy curves often contain important structural information, which can be essential for the analysis. To enable the extraction of all of the valuable features, a variable Fourier-smoothing of every  $I$ - $V$  spectrum was performed. The amount of smoothing had to be a free parameter, since great care had to be taken to remove all the additional shoulders and other modifications of the spectra, which were purely noise-induced. On the other hand, small maxima and minima that were caused by the crystal structure had to be kept, since they were reproduced by the calculation and therefore necessary for a good agreement - especially as long as the amount of agreement was determined by Pendry's  $R$ -factor (cf. Sec. 2.7).

### 2.2.4 Image processing

For further improvement of the quality of the measurement the recorded image-stacks could be processed using another macro, which was also written for the image processing software NIH Image. The basic goal was to get rid of disturbing effects caused by inhomogeneities of the LEED optics (grid, screen) as well as by pixel errors of the CCD camera. To achieve that aim a procedure was implemented, which was inspired by the processing of astronomical CCD-images [20]. As a prerequisite some *dark frame* and *flat field* images had to be taken during a measurement. A *dark frame* image is obtained by simply capturing an image of the screen without any post-acceleration of the diffracted electrons, whereas a *flat field* image is defined as a LEED pattern of a

polycrystalline area of the target holder. The actual image processing started with a subtraction of the averaged *dark frame* image from every LEED image of the stack, which corresponds to a background-subtraction. The following division by the averaged *flat field* image, from which the *dark frame* was also subtracted, eliminates all effects caused by imperfections of the setup, i.e. the LEED screen, the grids and the CCD camera. As a result, data evaluation of a processed image-stack shows a profoundly reduced noise, better agreement of the relative intensities of the symmetry equivalent beams and consequently better results for faint superstructure reflexes. The complete program code of the macro can be found in the appendix.

## 2.3 Basic principles

The physical origin of a LEED pattern lies in very fundamental properties of the crystal structure. Every perfectly ordered single crystal can be built up by the periodic arrangement of a basic building block called unit cell. Consequently, due to this translational symmetry, the definition of three (linearly independent) lattice vectors is sufficient to describe the whole crystal, as long as the unit cell is known. At the surface, however, this three-dimensional periodicity is destroyed, leading to a similar, but two-dimensional, problem. Accordingly, every surface - as a matter of fact, even every atomic layer of a crystal - can be built up by two-dimensional unit cells as indicated in the following equation:

$$\vec{r}_{mn} = m\vec{a}_1 + n\vec{a}_2 \quad m, n \in \mathbb{Z} \quad (2.3.1)$$

Here, the vector  $\vec{r}_{mn}$  is pointing at the origin of an arbitrary unit cell in the two-dimensional lattice. For simplicity, the following paragraphs will deal with elementary unit cells (comprised by one atom) only, the basic arguments, however, are valid for every arbitrary periodic surface structure.

Every two-dimensional unit cell in real space can be assigned a two-dimensional cell in reciprocal space, with corresponding reciprocal lattice vectors  $\vec{a}_1^*$  and  $\vec{a}_2^*$ . The relation between the real-space lattice vectors  $a_1, a_2$  and the vectors of the reciprocal lattice  $\vec{a}_1^*, \vec{a}_2^*$  is defined by Eq. (2.3.2), wherein  $\vec{n}$  is a unity vector perpendicular to the surface.

$$\vec{a}_1^* = 2\pi \left( \frac{\vec{a}_2 \times \vec{n}}{\vec{a}_1 \cdot (\vec{a}_2 \times \vec{n})} \right), \quad \vec{a}_2^* = 2\pi \left( \frac{\vec{n} \times \vec{a}_1}{\vec{a}_2 \cdot (\vec{n} \times \vec{a}_1)} \right) \quad (2.3.2)$$

As a result of these definitions it is obvious that the following relations are fulfilled:

$$a_1 \cdot \vec{a}_1^* = 2\pi \quad a_1 \cdot \vec{a}_2^* = 0 \quad (2.3.3)$$

$$a_2 \cdot \vec{a}_2^* = 2\pi \quad a_2 \cdot \vec{a}_1^* = 0 \quad (2.3.4)$$

Consequently, in analogy to Eq. (2.3.1) an arbitrary reciprocal lattice vector  $\vec{G}$  is given as

$$\vec{G}(h,k) = h\vec{a}_1^* + k\vec{a}_2^* \quad h, k \in \mathbf{Z} \quad (2.3.5)$$

### 2.3.1 The formation of a LEED pattern

Based on these very basic ideas and definitions concerning the description of the surface of a single crystal one can already try to understand the diffraction of an electron beam from a perfect, two-dimensional surface, whose unit cell consists of one single atom (see Fig. 2.3.1). Assuming that the electron source is sufficiently far away from the crystal allows the description of the impinging beam as plane wave, whose wave function is given by Eq. (2.3.6).

$$\Psi(\vec{r}) = \Psi_0 \cdot e^{i\vec{k} \cdot \vec{r}} \quad (2.3.6)$$

Since, according to the kinematic model proposed by Huygens, every atom can be interpreted as point-like scattering center of a certain strength  $f$  (atomic form factor), which is the origin of a corresponding spherical wave, the resulting scattered wave function  $\Psi'$  at a distance  $R \gg r_{mn}$  is given by Eq. (2.3.7).

$$\Psi'(\vec{R}) = \sum_{m,n} \Psi_0 \cdot e^{i\vec{k} \cdot \vec{r}_{mn}} \cdot f \cdot \frac{e^{ik\rho}}{P} \quad (2.3.7)$$

Hence, due to  $R \gg r_{mn}$  follows

$$\rho = |\vec{R} - \vec{r}_{mn}| \approx R - \frac{\vec{R}}{R} \cdot \vec{r}_{mn}, \quad \rho^{-1} \approx R^{-1} \quad (2.3.8)$$

which yields with the definition of the wave-vector of the elastically scattered wave  $\vec{k}' = \vec{k} - \frac{1}{R}\vec{R}$

$$\Psi'(\vec{R}) = \Psi_0 \cdot \frac{e^{ikR}}{R} \cdot f \cdot \underbrace{\sum_{m,n} e^{i(\vec{k} - \vec{k}') \cdot \vec{r}_{mn}}}_{S(\vec{k}')} \quad (2.3.9)$$

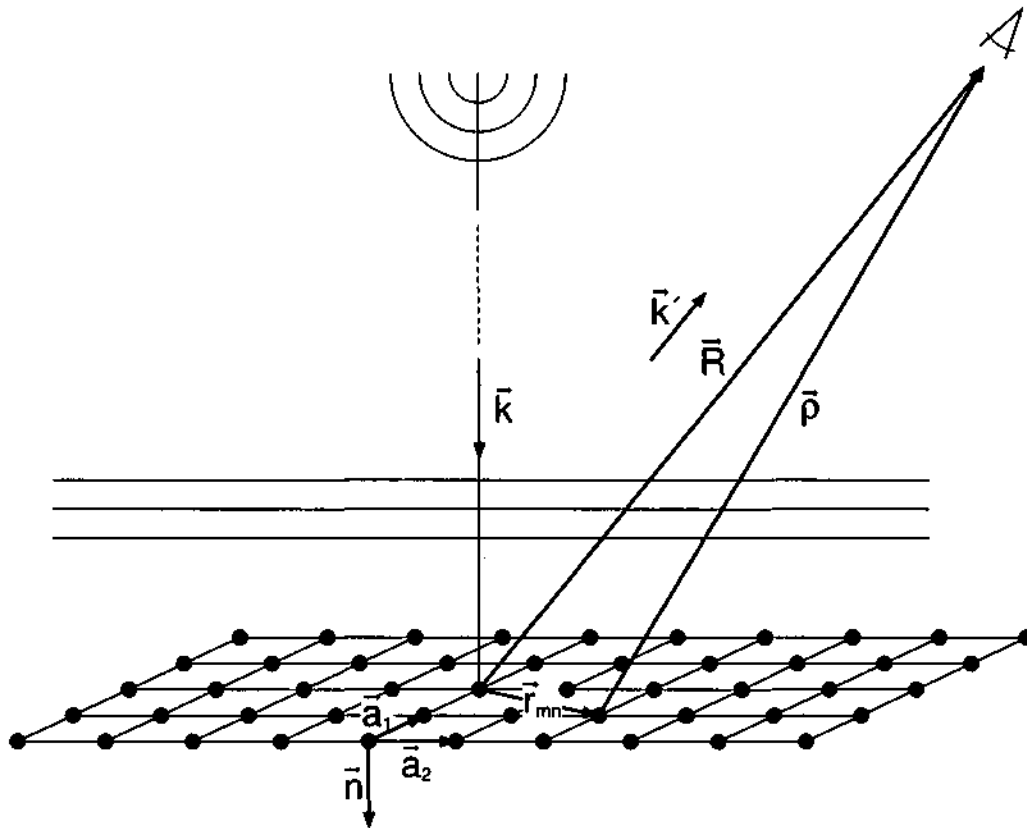


Figure 2.3.1: Schematic of the diffraction process from a two-dimensional surface. The incident wave, originating from a source far away from the surface, arrives at the lattice as a plane wave of wave vector  $\vec{k}$  causing the creation of spherical waves in every lattice point  $r_{mn}$ . The interference of these spherical waves at a large distance  $R$  results in intensity maxima and minima depending on the scattered wave vector  $\vec{k}'$ .

Obviously the diffracted wave-function is equivalent to a spherical wave originating from the surface, which is modulated by an angle-dependent structure factor  $S(\vec{k}')$ . Since the intensity of the diffracted beam is proportional to the square of the absolute value of this structure factor, it is worthwhile to investigate it thoroughly and to analyze its consequences. Choosing the coordinate system in such a way that the  $z$ -axis is parallel to the surface normal, it is clear that the  $z$ -component of  $(\vec{k} - \vec{k}')$  has no influence on the diffracted intensity, since the surface lattice vectors have no  $z$ -component. Generally speaking, it is sufficient to consider the parallel component of the momentum transfer with regard to the surface, which can be written in a general form using the reciprocal lattice vectors:

$$(\vec{k} - \vec{k}')_{\parallel} = \vec{G}(h, k) + \alpha \vec{a}_1^* + \beta \vec{a}_2^* \quad |\alpha|, |\beta| < 1 \quad (2.3.10)$$

Using Eq. (2.3.10) together with Eq. (2.3.1) and Eq. (2.3.4) results in

$$S(\vec{k}') = f \cdot \sum_{m,n} e^{i(\vec{k}-\vec{k}') \cdot \vec{r}_{mn}} = f \cdot \sum_m e^{-2\pi i \alpha m} \cdot \sum_n e^{-2\pi i \beta n} \quad (2.3.11)$$

Considering Eq. (2.3.11) it is clear that the structure factor strongly depends on the deviation of the parallel component of the momentum transfer from a vector of the reciprocal lattice. This becomes even more obvious if one looks at the intensities resulting from the evaluation of Eq. (2.3.11) for a lattice of the size ( $M \times N$ ).

$$I \propto |S(\vec{k}')|^2 \propto \frac{\sin^2(\pi \alpha M)}{\sin^2(\pi \alpha)} \cdot \frac{\sin^2(\pi \beta N)}{\sin^2(\pi \beta)} \quad (2.3.12)$$

Although the resulting intensity is an oscillating function depending on the size of the perfectly ordered ( $M \times N$ ) area, for a realistic domain size of  $\sim 1000 \times 1000 \text{ \AA}^2$  the only visible maxima are located at the positions corresponding to a parallel momentum transfer which exactly matches a reciprocal lattice vector (cf. Fig. 2.3.2). This can easily be seen in Eq. (2.3.11) directly, since in the limit of a perfect infinite surface the sums turn into integrals, which describe the two-dimensional  $\delta$ -function. Hence, the sharpness of the LEED spots, which corresponds to a certain parallel momentum transfer  $\vec{G}(h, k)$ , is a direct measure of the quality of a surface. Electrons diffracted from regions without any periodicity just contribute to the elastic background, which is eventually subtracted in the data evaluation process (cf. Section 2.2.3).

Summarizing the previous results one has to stress the fact that the formation of a LEED pattern is simply a consequence of the two-dimensional periodicity of the surface lattice. Due to this translational symmetry maxima can only be observed at those angles  $\vartheta$ , which correspond to a parallel momentum transfer equal to a reciprocal lattice vector  $\vec{G}(h, k)$ :

$$\vartheta = \arctan \frac{|\vec{k}_\parallel + \vec{G}(h, k)|}{|k'_\perp|}, \quad k'_\perp = \sqrt{\gamma m e^{\Phi} - \dots + (hk)^2} \quad (2.3.13)$$

Consequently, the observed LEED spots are moving towards the specular reflex with increasing electron energies  $E$ . However, since no restriction concerning the perpendicular component of the momentum transfer for the observation of maxima on the LEED screen exists, a LEED pattern occurs at every electron energy. That is a direct consequence of the two-dimensionality of a surface, since due to the missing restriction in the third dimension the allowed vectors  $(\vec{k} - \vec{k}')$  build up a "forrest" of rods - called crystal truncation rods (CTR) - in reciprocal space. This two-dimensionality is highly

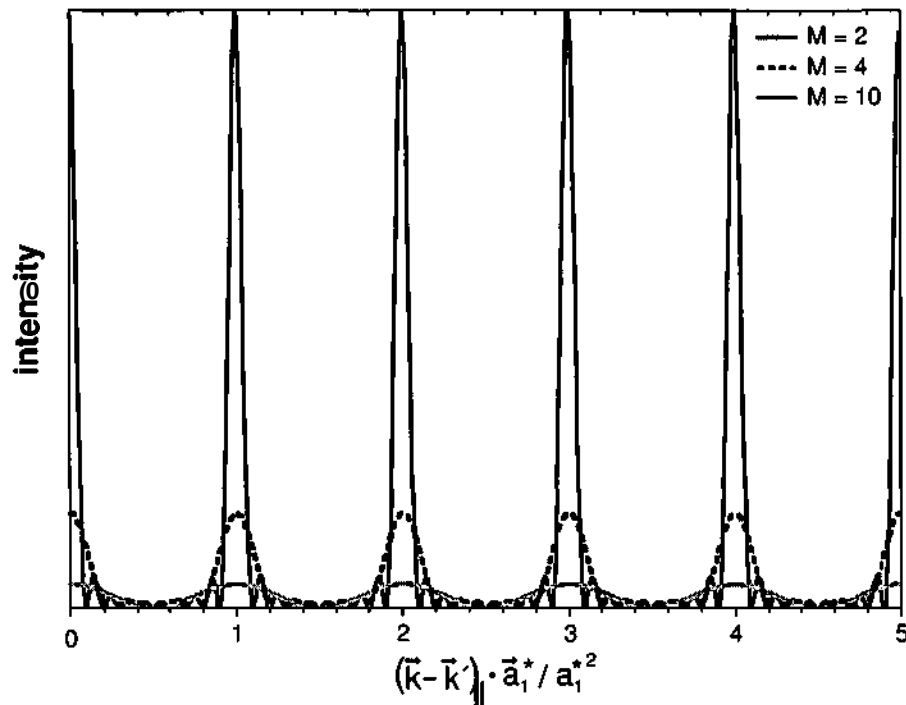


Figure 2.3.2: Intensity distribution in dependence of the momentum transfer parallel to the surface (one-dimensional case:  $k_\beta = 0$ ).

pronounced as long as the electron energy stays low, with increasing penetration depth of the electrons, however, bulk-induced effects result in a concentration of the observed maxima around the corresponding points of the three-dimensional reciprocal lattice (cf. Laue selection rules).

Another consequence resulting from Eq. (2.3.13) is that for a parallel component of the diffracted wave-vector larger than  $2m_e E / \hbar^2$  no reflections can be seen on the LEED screen, since in this case the perpendicular component of  $\vec{k}'$  gets imaginary and the corresponding wave decays exponentially. Those exponential waves, however, have to be included in the LEED calculations, because they still could reach the next atomic layer. Looking closely at part two of Eq. (2.3.13) it is easy to get a feeling for the appearance of the beams assigned to  $\vec{G}(h, k)$  on the screen. Considering normal incidence of the electron beam on a square lattice of side length  $a$ , the condition for the first non-specular beam to occur is the following:

$$\frac{2m_e E}{\hbar^2} > |\vec{G}(1, 0)|^2 \quad (2.3.14)$$

which results with  $E = \hbar^2 \left( \frac{2\pi}{\lambda} \right)^2$  and Eq. (2.3.2) in

$$\lambda < a, \quad \lambda[\text{\AA}] \approx \sqrt{\frac{150}{E[\text{eV}]}} \quad (2.3.15)$$

In other words the wave length of the incident electron beam has to be smaller than the smallest inter-atomic distance for the occurrence of non-trivial reflexes to be possible. For a hexagonal (111) surface the situation is a little bit more difficult resulting in  $\lambda < \frac{1}{2} a$ , which yields with the next neighbor distance of  $a = 2.75 \text{ \AA}$  for Pd(111) an appearance energy of  $\sim 27 \text{ eV}$  (on an ideal  $180^\circ$  LEED screen).

### 2.3.2 Superstructures

In reality one is often confronted with a slightly more complicated situation, namely the occurrence of a superstructure, which shows a larger periodicity than the corresponding primitive unit cell of the substrate. The physical origin for the formation of a superstructure can be either an intrinsic reconstruction of the clean surface, driven for example by the lower coordination at the surface layer (cf. Pt(110)-(1 x 2)), or the adsorption of additional particles. Adsorbates nearly always lead to some kind of superstructure either by profoundly modifying the substrate itself or by simply arranging in a certain ordered pattern on the surface. The two-dimensional periodicity of such an ordered superstructure can be defined by the use of superstructure unit-cell vectors  $\vec{b}_1$  and  $\vec{b}_2$ , which can be related to the primitive substrate lattice vectors  $\vec{a}_1$  and  $\vec{a}_2$  via a matrix M:

$$\vec{b}_1 = M_{11}\vec{a}_1 + M_{12}\vec{a}_2 \quad (2.3.16)$$

$$\vec{b}_2 = M_{21}\vec{a}_1 + M_{22}\vec{a}_2 \quad (2.3.17)$$

In the majority of cases the dependence in Eq. (2.3.17) is a simple one resulting in integer values of the matrix elements  $M_{ij}$ . In some other cases the matrix elements are rational numbers, the corresponding superlattice is then called *commensurate*. The third possible type of superstructure results in irrational values of  $M_{ij}$  and is termed *incommensurate* (cf. Sec. Pd-O).

Since the superstructure unit-cell vectors are in general larger than the substrate vectors, the corresponding reciprocal lattice vectors are smaller, resulting in the appearance of additional spots in the LEED pattern. In case of a perfectly well ordered superstructure, the sharpness of the corresponding beams is similar to the one of the substrate beams. Knowing that the LEED patterns recorded by experiment are direct

images of the reciprocal lattice one can immediately deduce the correct periodicity of the observed superstructure. However, it is just the size of the superstructure unit-cell and its orientation with regard to the substrate lattice, which can be extracted directly from a given LEED pattern, since a lot of cells with different internal atomic structure can yield exactly the same pattern. As a matter of fact, most of the superstructure unit-cells are not primitive, i.e. they consist of several atoms of possibly different scattering strength  $f_j$  situated at positions  $\vec{r}_j$  within the cell, that are not necessarily located in the same horizontal plane. To account for that, the structure factor given in Eq. (2.3.11) changes to:

$$S(\vec{k}') = \sum_{m,n} \sum_j f_j e^{i(\vec{k}-\vec{k}') \cdot (m\vec{b}_1+n\vec{b}_2+\vec{r}_j)} = \sum_{m,n} e^{i(\vec{k}-\vec{k}')_{\parallel} \cdot (m\vec{b}_1+n\vec{b}_2)} \cdot \sum_j f_j e^{i(\vec{k}-\vec{k}') \cdot \vec{r}_j} \quad (2.3.18)$$

Accordingly, the atomic structure within a superstructure cell just modifies the intensities of the superstructure beams, but it does neither influence their position nor does it give rise to additional beams. It can, however, extinguish certain beams as in case of a reconstruction with p4g-symmetry. Furthermore, a modification of the intensity variation of the superstructure beams depending on the energy of the incident electron beam is also possible, as long as the according supercell is not purely two-dimensional (cf. Sec. 2.4).

## 2.4 Energy dependence of the beam intensities

### 2.4.1 Kinematic approximation

So far only the two-dimensions of the uppermost surface layer have been taken into account, but for the description of a real crystal one has to include several atomic layers, depending on the penetration depth of the probing electron beam. Considering an interlayer vector  $\vec{a}_3$  pointing from one atom of the first layer to the corresponding atom of the subsequent layer, in the kinematic single scattering approximation the structure factor of Eq. (2.3.9) changes to:

$$S(\vec{k}') = f \cdot \sum_{m,n,o} e^{i(\vec{k}-\vec{k}') \cdot (\vec{r}_{mn}+o\vec{a}_3)} = \sum_o e^{io(\vec{k}-\vec{k}') \cdot \vec{a}_3} \cdot \sum_{m,n} e^{i(\vec{k}-\vec{k}') \cdot \vec{r}_{mn}} \quad (2.4.1)$$

Consequently another condition for constructive interference of diffracted waves is introduced:

$$(k - \vec{k}') \cdot a_3 = 2\pi l, \quad l \in \mathbb{Z} \quad (2.4.2)$$

Since the parallel component of the momentum transfer is restricted to a certain value predefined by the according beam order  $(h, k)$ , its perpendicular component for a given electron energy is determined by the energy-conservation law. As a result, the intensities of the diffracted beams are energy dependent and reach maxima at certain energy values for which condition (2.4.2) is fulfilled. Those energies at which constructive interference of the contributions from multiple surface layers occurs are called *Bragg-energies*. Bragg-energies carry a lot of information about the interlayer distances and the stacking of the investigated crystal, since they do not depend on  $a_{3\perp}$  only, but also on  $a_{3\parallel}$  (called *registry shift*).

In order to get a good approximation of the interlayer distances directly out of the Bragg-energies of a certain beam one has to take the influence of the crystal potential into account. As an electron beam enters a crystal it gains additional energy equal to an average binding-energy throughout the crystal, which is loosely related to the crystals work-function. For the LEED analysis this acceleration is considered to be caused by a constant inner potential  $V_0$  (cf. Sec. 2.5.1), which is responsible for a shift of the intensity maxima in the measured  $I$ - $V$  spectra to lower energies with regard to the calculated Bragg-energies. Consequently, the effective electron energy in the crystal changes to

$$\bar{E} = E + V_0 \quad (2.4.3)$$

An example of the theoretically calculated Bragg-energies with and without the consideration of the inner potential  $V_0$  is given in Fig. 2.2.2.

### 2.4.2 Mean free path

The real shape of a measured  $I$ - $V$  curve, however, is furthermore profoundly influenced by another property inherent to a beam of low energy electrons, namely its inelastic mean free path or in other words the damping of the electron beam as it propagates through a crystal. This damping is a result of inelastic scattering processes, caused mainly by electronic excitations and the creation of plasmons or charge density waves. To account for these effects the amplitude of the electron beam has to be forced to decrease gradually as it propagates from layer to layer. This is realized in the theoretical description by the introduction of an imaginary part of the inner potential  $V_{0i}$ , which

automatically leads to a complex wave-vector, due to the well known energy-momentum relationship

$$\bar{E} = E + V_{0r} + iV_{0i} = \frac{\hbar^2 k^2}{2m_e} = \frac{\hbar^2}{2m_e} (k_r + ik_i)^2 \quad (2.4.4)$$

This complex wave-vector has therefore to fulfill the following relations:

$$k_r^2 - k_i^2 = \frac{2m_e}{\hbar^2} (E + V_{0r}), \quad k_r k_i = \frac{2m_e}{\hbar^2} V_{0i} \quad (2.4.5)$$

Since  $V_{0i}$  is small compared to  $E + V_{0r}$  one can neglect  $k_i^2$  with respect to  $k_r^2$ , which leads to

$$k_r \cong \sqrt{\frac{2m_e}{\hbar^2} (E + V_{0r})}, \quad k_i \cong \frac{V_{0i}}{\sqrt{\frac{2m_e}{\hbar^2} (E + V_{0r})}} \quad (2.4.6)$$

and, thus, to an exponential decay of the incident wave within the crystal:

$$e^{ikz} = e^{ik_r z} e^{-k_i z} = e^{ik_r z} e^{-\frac{z}{\lambda_e}}, \quad \lambda_e \cong \frac{\sqrt{\frac{2m_e}{\hbar^2} (E + V_{0r})}}{V_{0i}} \quad (2.4.7)$$

Moreover, Eq. (2.4.7) proves that the concept of a finite mean-free-path length  $\lambda_e$  of the electrons in the crystal and the introduction of an imaginary part of the inner potential are in fact equivalent. The importance of damping, however, becomes obvious as soon as one realizes that without it LEED would lose its greatest advantage, namely its surface sensitivity, which is a direct consequence of the restricted mean-free-path length caused by the inelastic scattering. Since only a few atomic layers are being probed by the electron beam (e.g.  $\lambda_e = 8.1 \text{ \AA}$  for  $E = 100 \text{ eV}$ ,  $V_0 = 7 + 5i \text{ eV}$ ), the first sum on the right hand side of Eq. (2.4.1) converges:

$$\sum_{\sigma=0}^{\infty} e^{i\sigma(\vec{k}-\vec{k}')\cdot\vec{a}_3} = \frac{1}{1 - e^{i(\vec{k}-\vec{k}')\cdot\vec{a}_3}} \quad (2.4.8)$$

Consequently, the energy dependence of the intensity of a certain beam is governed by Eq. (2.4.8) in the kinematic limit, which results in finite maxima at the Bragg-energies and a continuous - non-zero - intensity distribution between the maxima. The shapes of the maxima resemble Lorentzian curves as depicted in Fig. 2.4.1. The reason for this continuous energy-intensity relationship of every beam is based on the broken

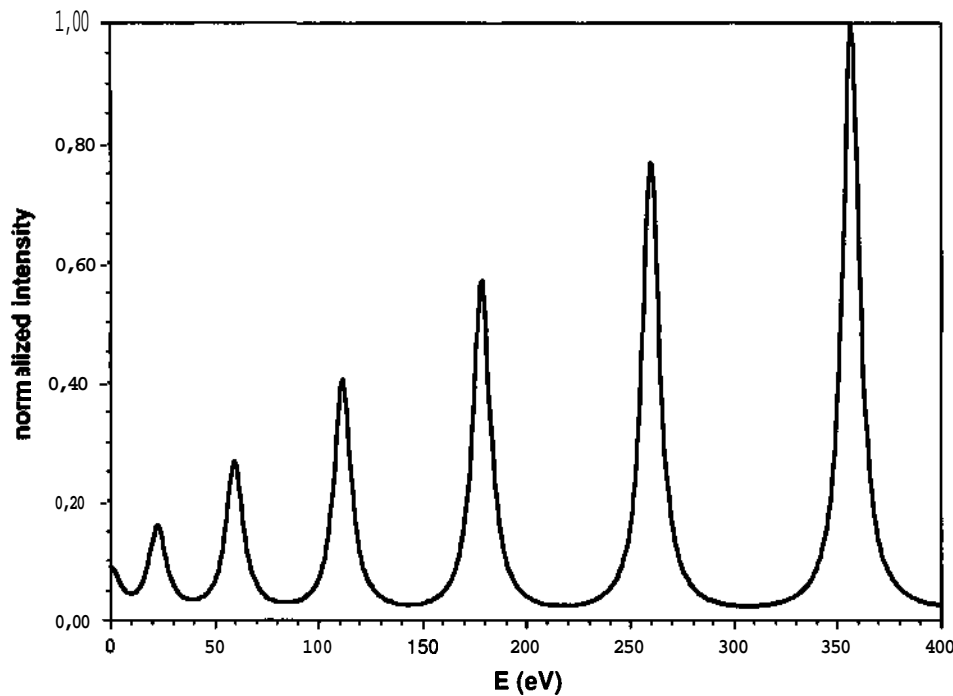


Figure 2.4.1: Intensity variation of the specular reflex (0,0) in the kinematic approximation in case of normal incidence on a Pd(111) crystal with an interlayer distance of  $2.25\text{\AA}$ . Due to damping of the electron beams - realized by the imaginary part of the inner potential  $V_{0i} = 5\text{ eV}$  - the intensity maxima are finite and non-zero in-between.

translational symmetry of the crystal in the direction perpendicular to the surface, caused by the finite penetration depth of the impinging electron beam.

### 2.4.3 Multiple scattering — a qualitative description

Additional features in the  $I$ - $V$  spectra are introduced due to multiple elastic scattering of the electron beam. The scattering angle, however, is strongly dependent on the angle of incidence with regard to the current scattering center. Although backward-scattering is the essential mechanism for LEED, the most likely elastic scattering events involve scattering in forward direction, causing just a shift of the according phases, or in directions with rather small deflection angles. Consequently, an impinging electron beam creates a lot of new beams of comparable intensity, which continue to propagate to the next atomic layer. Every single beam can now cause Bragg-reflections to occur, even if the primary electron energy is not close to a Bragg-energy. As a result of that, a lot of new maxima can usually be observed in a realistic  $I$ - $V$  curve, that are not directly related to the original electron beam impinging on the surface (cf. Fig. 2.2.2).

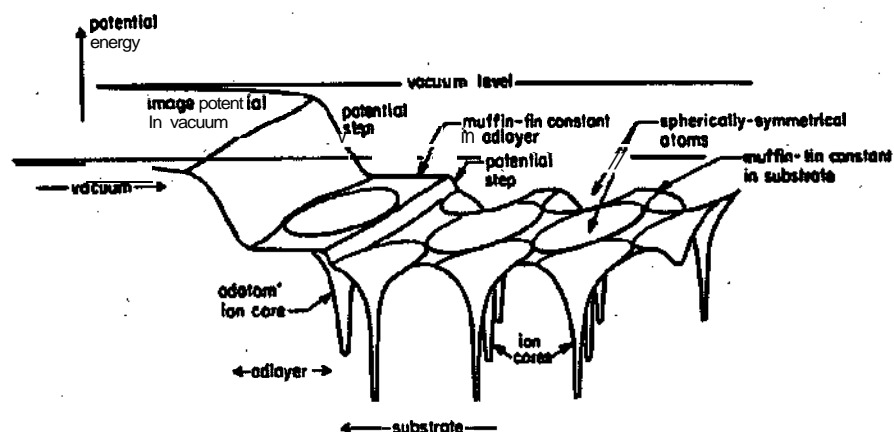


Figure 2.5.1: Sketch of a muffin-tin potential describing a surface with an adsorbate layer [21].

### 2.5.1 Muffin-tin potential

Since neither the wave functions  $\psi_i$  nor the electronic charge distribution  $p$  are known, Eq. (2.5.1) can not be used for computation in its current form. Consequently, some approximations have to be made in order to solve that problem. One approximation used in nearly all LEED calculations assumes spherical symmetry of the potential around each atom within the largest possible sphere that does not overlap with any of the other spheres centered at neighboring atoms. In the interstitial regions between the spheres, the potential is assumed constant (cf. inner potential  $V_0$ ). The above described approximation is called *muffin-tin* approximation and sketched in Fig. 2.5.1. These assumptions worked very well for most of the LEED investigations, since the radii of those muffin-tin spheres are in general large enough for the core potential to diminish sufficiently and the wave length of the LEED electrons is small compared to the real potential variations in the interstitial areas. For very open structures, however, this approximation might comprise a problem (cf. Sec. Vacuum spheres).

As a result of the muffin-tin approximation the problem boils down to the solution of the Schrödinger equation for an electron scattered from a single atom, which is modeled as described above. Because of the spherical symmetry of the atomic potential, the wave function of the electron can be separated into a radial part and an angular dependent part - in other words it can be developed in *partial waves*.

$$\varphi(\vec{r}) = \sum_{l,m} a_{lm} \phi_l(r) Y_{lm}(\Omega) \quad (2.5.2)$$

The resulting differential equation for the radial part  $\phi_l(r)$  is given by

$$-\frac{\hbar^2}{2m_e} \frac{1}{r^2} \frac{d}{dr} \left( r^2 \frac{d\phi_l}{dr} \right) + \frac{\hbar^2 l(l+1)}{2m_e r^2} \phi_l + V_C(r) \phi_l + \int V_l^{ex}(r,r') \phi_l(r') r'^2 dr' = E \phi_l \quad (2.5.3)$$

with the Coulomb potential

$$V_C(r) = -\frac{Ze^2}{r} + e^2 \sum_j \int \frac{|\psi_j(r')|^2}{|\vec{r} - \vec{r}'|} d^3r' \quad (2.5.4)$$

and a rather complex exchange potential  $V_l^{ex}$ , whose exact description can be found e.g. in Ref. [13]. Outside of the muffin-tin spheres, however, both potentials are zero:

$$V_C(r), V_l^{ex}(r,r') = 0, \quad \forall r > R_{muf} \quad (2.5.5)$$

where  $R_{muf}$  is the muffin-tin radius. Eq. (2.5.3) now has to be solved for every atom within and outside of the muffin-tin sphere, with the boundary condition of showing a continuous and continuously differentiable transition at  $r = R_{muf}$ .

### 2.5.2 Atomic scattering

Since the Coulomb potential  $V_C(r)$  and the exchange potential  $V_l^{ex}$  are by definition zero outside of the muffin-tin sphere, due to the above described approximation, the radial Schrödinger equation in the interstitial region is reduced to

$$-\frac{\hbar^2}{2m_e} \frac{1}{r^2} \frac{d}{dr} \left( r^2 \frac{d\phi_l}{dr} \right) + \frac{\hbar^2 l(l+1)}{2m_e r^2} \phi_l = E \phi_l, \quad r > R_{muf} \quad (2.5.6)$$

with the general solutions

$$\phi_l = \alpha_l h_l^{(1)}(kr) + \beta_l h_l^{(2)}(kr), \quad k = \frac{\sqrt{2m_e E}}{\hbar} \quad (2.5.7)$$

Here,  $h_l^{(1)}$  and  $h_l^{(2)}$  are the spherical Hankel functions of the first and the second kind and  $\alpha_l, \beta_l$  are complex constants. The asymptotic form of this solution, however, is given as

$$\phi_l = \alpha_l i^{-(l+1)} \frac{e^{+ikr}}{kr} + \beta_l i^{l+1} \frac{e^{-ikr}}{kr} \quad (2.5.8)$$

Consequently, in the region outside of the muffin-tin sphere, the radial wave-function of the electron consists of an incoming wave of the amplitude  $\beta_l$  and an outgoing wave of the amplitude  $\alpha_l$ . Due to the fact that only elastically scattered electrons are considered by LEED, both waves have to be of equal magnitude, in order to satisfy the current conservation law. Therefore, the only possible effect of the spherical scattering potential is a phase shift  $\delta_l$  of the outgoing wave, which is indicated in Eq. (2.5.9).

$$0, = \beta_l \left[ e^{i2\delta_l} h_l^{(1)} + f_l \right], \quad (2.5.9)$$

Notice, however, that just the phase is changed, but the angular momentum is conserved due to the spherical nature of the scattering potential. Consequently, the phase shifts contain all the information needed for a description of the scattering process in the muffin-tin approximation and are in general readily available for every element in a tabulated form.

In order to obtain the phase shifts directly, one has to solve Eq. (2.5.3) within the muffin-tin sphere and to match this solution smoothly to the solution outside. This is usually done by equating the corresponding logarithmic derivatives at the muffin-tin radius  $R_{muf}$ . Let  $\Phi_l(r)$  be the radial solution inside, the following condition has to be fulfilled:

$$\frac{\Phi_l'(R_{muf})}{\Phi_l(R_{muf})} = \frac{e^{i2\delta_l} h_l^{(1)'}(kR_{muf}) + h_l^{(2)'}(kR_{muf})}{e^{i2\delta_l} h_l^{(1)}(kR_{muf}) + h_l^{(2)}(kR_{muf})} \quad (2.5.10)$$

Resulting in

$$e^{i2\delta_l} = \frac{L_l h_l^{(2)}(kR_{muf}) - h_l^{(2)'}(kR_{muf})}{h_l^{(1)'}(kR_{muf}) - L_l h_l^{(1)}(kR_{muf})}, \quad L_l = \frac{\Phi_l'(R_{muf})}{\Phi_l(R_{muf})} \quad (2.5.11)$$

Eq. (2.5.11) shows that the phase shifts  $\delta_l$  depend not only on the scattering center but also on the energy of the incident electron. Therefore, an above mentioned table usually contains the phase shifts of a certain element for every angular momentum up to  $l = 16$  and for every energy (in 1 eV steps) between 10 and 500 eV.

### 2.5.3 t-matrix

Eq. (2.5.9) can be split up into an undisturbed part  $\phi_l^0$  and a scattered part  $\phi_l^s$ , since  $\phi_l^s$  is simply the difference between the wave function in the presence of a scattering center and the corresponding result for  $\delta_l = 0$ , thus leading to:

$$\phi_l^0 = \beta_l (h_l^{(1)} + h_l^{(2)}) = \beta_l 2j_l \quad (2.5.12)$$

and

$$\phi_l^s = \beta_l (h_l^{(1)} - h_l^{(2)}) = \beta_l 2i \sin \delta_l e^{i\delta_l} h_l^{(1)} \quad (2.5.13)$$

where  $j_l$  are the spherical Bessel functions. The complete wave function therefore amounts to

$$\varphi(\vec{r}) = \sum_{l,m} a_{lm} \phi_l(r) Y_{lm}(\Omega) = \sum_{l,m} a_{lm} (\phi_l^0(r) + \phi_l^s(r)) Y_{lm}(\Omega) \quad (2.5.14)$$

For a description of the situation encountered in a LEED experiment, however, one has to consider plane waves. By expanding an undisturbed incoming plane wave into spherical waves

$$e^{i\vec{k}\cdot\vec{r}} = \sum_{l,m} 4\pi i^l j_l(kr) Y_{lm}^*(\Omega(\vec{k})) Y_{lm}(\Omega(\vec{r})) \quad (2.5.15)$$

it is possible to compare it with the previous results and, consequently, to determine the expansion coefficients  $a_{lm}\beta_l$ .

$$a_{lm}\beta_l = 2\pi i^l Y_{lm}^* \quad (2.5.16)$$

Putting (2.5.16) into the general expression for the scattered wave of Eqs. (2.5.13) and (2.5.14) and using the following relation for the Legendre polynomials  $P_l(\cos \theta)$ , with  $\theta$  being the scattering angle in this case

$$P_l(\cos \theta) = \frac{4\pi}{2l+1} \sum_{m=-l}^l Y_{lm}^*(\Omega(\vec{k})) Y_{lm}(\Omega(\vec{r})) \quad (2.5.17)$$

results in

$$\varphi_s(\vec{r}) = \sum_l i^{l+1} (2l+1) \sin \delta_l e^{i\delta_l} P_l(\cos \theta) h_l^{(1)}(kr) \quad (2.5.18)$$

which represents in its asymptotic form for  $r \rightarrow \infty$  a spherical wave modulated by a scattering factor  $f(E, \vartheta)$

$$\varphi_s(\vec{r}) \stackrel{r \rightarrow \infty}{\sim} f(E, \theta) \frac{e^{ikr}}{r}, \quad f(E, \theta) = -\frac{1}{\kappa} \sum_l (2l+1) t_l(E) P_l(\cos \theta) \quad (2.5.19)$$

with

$$t_l(E) = \sin \delta_l e^{i\delta_l} \quad (2.5.20)$$

This set of functions  $t_l$  is called *atomic t-matrix* [13], which only depends on the phase shifts  $\delta_l$  of the individual atom and completely contains all the necessary scattering properties. Consequently, having a tabulated set of phase shifts is sufficient to calculate the according atomic t-matrices and therefore the scattered wave.

Taking a closer look at the mathematical properties of the scattering factor  $f(E, \theta)$  reveals the fact that forward scattering (i.e. scattering in directions that deviate only minor from  $\vartheta = 0^\circ$ ) is indeed the most probable event: The scattering factor shows a pronounced maximum at  $\vartheta = 0^\circ$ , which grows with increasing energy, while the according full width at half maximum is reduced. Consequently, the amount of backward scattered electrons ( $\vartheta > 90^\circ$ ), which is of significant importance for LEED, is quite small compared to the forward scattered one, namely in the order of about 10%. However, every scattering event involves a phase shift independent of the scattering angle and therefore a non-trivial  $f(E, \theta)$ . The highest quantum number  $l_{max}$  of the angular momentum that has to be considered in the calculation of the t-matrix depends exclusively on the energy of the incident electron and the atomic radius  $r$ . Since with decreasing wave length (i.e. increasing energy) the diffraction pattern caused by a single atom gets more and more finely structured, it is obvious that states with higher  $l$  have to be included. Moreover, states with high angular momentum quantum numbers also get excited whenever an electron is scattered in the outer region of an atom, therefore larger atoms require a greater value of  $l_{max}$ . An estimation of the highest quantum number  $l_{max}$  needed for the calculation is given by

$$l_{max} \sim kr \quad (2.5.21)$$

which yields for an electron energy of 400 eV and an atomic radius of 1 Å an  $l_{max}$  value of 10. Although most phase shift tables contain phase shifts up to  $l = 16$ , usually an  $l_{max}$  value of 10 is sufficient for a modern LEED calculation, since the inclusion of higher values just results in an enormous increase of the computing time, without any observable influence on the  $I$ - $V$  spectra.

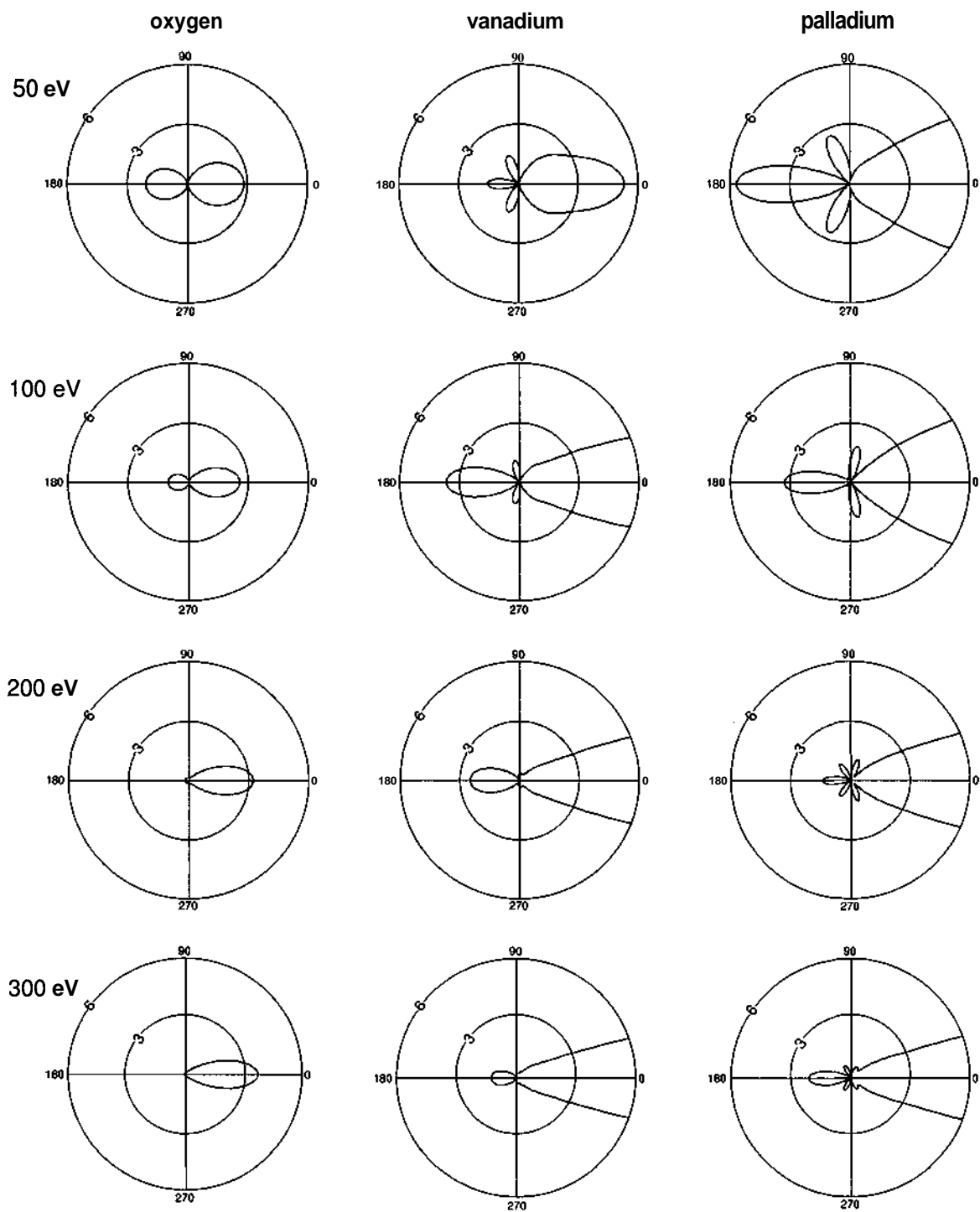


Figure 2.5.2: Differential cross sections for electron diffraction from oxygen, vanadium and palladium atoms at different electron energies.

The differential cross section for scattering into a certain angle can be directly deduced from Eq. (2.5.19) and results simply in

$$\frac{\partial\sigma(E, \theta)}{\partial\Omega} = |f(E, \theta)|^2 \quad (2.5.22)$$

Fig. 2.5.2 shows polar plots of the differential cross sections of palladium, vanadium and oxygen at different electron energies, where it is obvious that with increasing energies the amount of forward scattering gets more and more pronounced - especially for oxygen, which is known to be a weak scatterer.

The total cross section  $\sigma_{total}$  is therefore obtained by an integration of Eq. (2.5.22), which yields the following result:

$$\sigma_{total} = \frac{4\pi}{k^2} \sum_l (2l + 1) \sin^2 \delta_l \quad (2.5.23)$$

The elastic mean free path is now given as the reciprocal value of the product of the total cross section  $\sigma_{total}$  and the density of the scattering atoms. For palladium the elastic mean free path at 100 eV is roughly 2.3 Å (cf.  $\sigma_{total} = 6.3 \text{ \AA}^2$ ), which shows that the probability for a multiple scattering event is very high. Since the inelastic mean free path length is - although in the same order of magnitude - considerably larger than the corresponding elastic mean free path length (cf. Sec. 2.4.2), it is also very likely that multiple elastic scattering events occur before the first inelastic one. Long scattering pathways, involving numerous, purely elastic scattering events, however, are very improbable. Consequently, a correct calculation of the beam intensities is only possible if multiple scattering effects are considered by LEED-theory.

#### 2.5.4 Temperature effects

Before dealing with the full dynamical approach (i.e. multiple scattering) another influence on the beam intensities has to be considered. Since thermal vibrations of surface atoms have numerous effects on electron diffraction, they should also be included in the kinematic description of the scattering process. All temperature effects are naturally caused by the positional disorder of the vibrating surface atoms. A broadening of the diffraction spots with increasing temperature can be observed due to momentum exchange of impinging electrons with phonons, additionally the spot intensities themselves are decreased due to destructive interference effects between electron waves scattered by slightly displaced atoms. This decrease in every beam-intensity can be

described by a Debye-Waller factor. The lost intensity, however, contributes to an increased background intensity due to thermal diffuse scattering.

Since thermal vibrational periods are some orders of magnitude longer than the electron scattering times, the crystal can be considered as frozen in an arbitrary slightly disordered state. Consequently, the reflected waves, which would normally fulfill the Bragg conditions are in general a little bit out of phase. Just in case of forward scattering the thermal displacement of the atoms has no effect on the phases of the scattered electron waves. These effects are usually accounted for by the introduction of a Debye-Waller factor  $e^{-2M}$  multiplied to the beam intensities, resulting in  $I = I_0 e^{-2M}$ . This Debye-Waller factor is well known and given by [21]

$$e^{-2M} = e^{-|\vec{s}|^2 \langle (\Delta\vec{r})^2 \rangle} \quad (2.5.24)$$

where  $\vec{s}$  is the three-dimensional momentum transfer and  $\langle (\Delta\vec{r})^2 \rangle$  is the mean square deviation of the crystal atoms. In case of isotropic vibrations the Debye model allows the calculation of the mean amplitude  $A_{vib}$  of the thermal vibrations according to the following formula [21]

$$A_{vib}[\text{\AA}] = \sqrt{\langle (\Delta\vec{r})^2 \rangle} = \frac{1}{\Theta_D} \sqrt{\frac{432.6 \cdot T_{le}[\text{K}]}{m_{rel}[\text{amu}]}} \quad (2.5.25)$$

where  $\Theta_D$  is the Debye temperature of the considered element,  $T_{sample}$  the sample temperature and  $m_{rel}$  the relative atomic mass.

Within the multiple scattering formalism, however, temperature effects have to be included in the description of every scattering event, which is realized by replacing the phase shifts  $\delta_i$  with temperature dependent phase shifts  $\delta_i(T)$  as described in Sec. 2.6.2.

## 2.6 Dynamical LEED theory

As pointed out several times, for an accurate description of the scattering process in LEED the kinematic approach turns out to be insufficient, due to its inability to explain the additional maxima and minima observed in measured  $I$ - $V$  spectra (cf. Fig. 2.2.2). Since these additional features are caused by multiple scattering of the impinging electron beam, every LEED theory has to include these events in its very core. In the following Dirac notation is used, since it enables a rather easy and straightforward description of the multiple scattering process. Within this formalism the Schrödinger equation of the LEED problem is given by

$$(H_0 + V_s) |\Phi(\vec{k}_{\parallel})\rangle = E |\Phi(\vec{k}_{\parallel})\rangle \quad (2.6.1)$$

where  $H_0$  denotes the Hamilton operator of a free electron and  $V_s$  is the effective single-particle potential for the diffraction state  $|\Phi(\vec{k}_{\parallel})\rangle$ . According to the muffin-tin approximation  $V_s$  within the crystal is defined as

$$V_s = V_{0r} + iV_{0i} + \sum_j v_j (|\vec{R}_j\rangle) \quad (2.6.2)$$

Here,  $V_j$  is the effective potential of a single atom located at the position  $R_j$  within the muffin-tin approximation as discussed in Sec. 2.5.1 and  $V_{0r}$ ,  $V_{0i}$  are the real and the imaginary part of the inner potential. Defining the crystal potential  $V := \sum_j v_j$  and  $\tilde{E} := E - V_{0r} - iV_{0i}$  results in

$$(H_0 + V) |\Phi(\vec{k}_{\parallel})\rangle = \tilde{E} |\Phi(\vec{k}_{\parallel})\rangle \quad (2.6.3)$$

This equation now has to be solved within the crystal, which is usually done by means of a scattering path formalism, allowing electrons to be scattered several times back and forth between various surface atoms before leaving the crystal again. Since the complete derivation within the formalism of Green's functions can be found in literature (cf. Refs. [13, 21]), only the basics are presented in the next section.

### 2.6.1 Multiple scattering - a quantitative description

The basic concept for the solution of the multiple scattering problem is the inversion of the Schrödinger equation (2.6.3) to its integral form by the use of Green's functions. Let  $|\phi_0(\vec{k}_{\parallel})\rangle$  be the state of the incident electron wave in the regions of constant potential inside the crystal, then the Green's operator  $G_0 = (\tilde{E} - H_0)^{-1}$  of the homogeneous Schrödinger equation transforms the incident state into a simple plane wave

$$G_0 |\phi_0(\vec{k}_{\parallel})\rangle = |\vec{k}_0^+\rangle \quad (2.6.4)$$

Similarly, the Green's operator  $G$  of the complete Schrödinger equation (2.6.3) transforms by definition the initial state into the diffracted state

$$G |\phi_0(\vec{k}_{\parallel})\rangle = |\Phi(\vec{k}_{\parallel})\rangle \quad (2.6.5)$$

Rearranging Eq. (2.6.3) to

$$V |\Phi(\vec{k}_{\parallel})\rangle = (\tilde{E} - H_0) |\Phi(\vec{k}_{\parallel})\rangle \quad (2.6.6)$$

and letting the homogeneous Green's operator  $G_0$  act on Eq. (2.6.6) yields for the diffracted state (after adding a homogeneous solution  $|\vec{k}_0^+\rangle$ )

$$|\Phi(\vec{k}_{\parallel})\rangle = G_0 |\phi_0(\vec{k}_{\parallel})\rangle + G_0 V |\Phi(\vec{k}_{\parallel})\rangle \quad (2.6.7)$$

Equivalently, the definition of the operator  $T$  via  $V |\Phi(\vec{k}_{\parallel})\rangle = T |\vec{k}_0^+\rangle$  results in the Lippman-Schwinger equation [22] for the diffracted state

$$|\Phi(\vec{k}_{\parallel})\rangle = |\vec{k}_0^+\rangle + G_0 V |\Phi(\vec{k}_{\parallel})\rangle = (1 + G_0 T) |\vec{k}_0^+\rangle \quad (2.6.8)$$

Consequently,  $G$  and  $T$  fulfill the following equations, respectively

$$G = G_0 + G_0 V G, \quad T = V + V G_0 T \quad (2.6.9)$$

and can be expressed as Born's series

$$G = G_0 + G_0 V G_0 + G_0 V G_0 V G_0 + \dots, \quad T = V + V G_0 V + V G_0 V G_0 V + \dots \quad (2.6.10)$$

For scattering by just one atom at the position  $\vec{R}_i$ ,  $V$  is reduced to  $V_i$ , which results with the definition of the atomic t-matrix

$$t_i = V_i + v_i G_0 v_i \dots \quad (2.6.11)$$

in

$$G_{atom} = G_0 + G_0 t_i G_0 \quad \text{and} \quad T_{atom} = t_i \quad (2.6.12)$$

This atomic t-matrix includes all multiple scattering events within a certain atom and is equivalent to the representation in Sec. 2.5.3. Using definition (2.6.11) in Eq. (2.6.10) results in a series of individual scattering events at different crystal atoms  $i$ , which are connected by the Green's operator of the homogeneous Schrödinger equation  $G_0$

$$T = \sum_i t_i + \sum_i \sum_{j, j \neq i} t_j G_0 t_i + \sum_i \sum_{j, j \neq i} \sum_{k, k \neq i, j} t_k G_0 t_j G_0 t_i \dots \quad (2.6.13)$$

Finally, the amplitude  $A_{\vec{g}}^-$  of a diffracted electron beam  $|\vec{k}_{\vec{g}}^- \rangle$  is given by

$$A_{\vec{g}}^- = \langle \vec{k}_{\vec{g}}^- | \Phi(\vec{k}_{\parallel}) \rangle = \langle \vec{k}_o^- | 1 + G_0 T | \vec{k}_o^+ \rangle \quad (2.6.14)$$

with

$$\langle \vec{r} | \vec{k}_{\vec{g}}^- \rangle = e^{i\vec{k}_{\vec{g}}^- \cdot \vec{r}}, \quad \vec{k}_{\vec{g}\parallel}^- = \vec{k}_{\parallel} + \vec{g} \quad \text{and} \quad \text{fcj}_{\pm} = -\sqrt{2E - |\vec{k}_{\parallel} + \vec{g}|^2} \cdot \frac{\vec{k}_{\perp}}{|\kappa_{\perp}|} \quad (2.6.15)$$

Since Eqs. (2.6.13) and (2.6.14) contain all that is needed to solve the LEED problem, the only thing left is a practical approach to gain the final beam intensities. As a first step the atomic t-matrices have to be calculated as indicated in Sec. 2.5.3, which describe the scattering processes for a single atom. After that layer diffraction matrices  $M_{\vec{g}'\vec{g}}^{\pm\pm}$  are computed, which are obtained from the operator  $T_{layer}$ , containing only t-matrices of the according atomic layer, via

$$M_{\vec{g}'\vec{g}}^{\pm\pm} = \langle \vec{k}_{\vec{g}'}^{\pm} | 1 + G_0 T_{layer} | \vec{k}_{\vec{g}}^{\pm} \rangle \quad (2.6.16)$$

where  $|\vec{k}_{\vec{g}}^{\pm} \rangle$  represents an incoming and  $|\vec{k}_{\vec{g}'}^{\pm} \rangle$  an outgoing plane wave. Restrictions on the outgoing plane waves are imposed by the condition that the lateral momentum has to be conserved ( $\pm$  a reciprocal lattice vector  $\vec{g}$ ). Also the energy conservation law limits the number of possible outgoing wave vectors, although a slight violation of this law just leads to an imaginary  $k_{\vec{g}'\perp}^{\pm}$ , which might allow the wave to propagate until the next layer. Nevertheless, the number of possible outgoing waves  $|\vec{k}_{\vec{g}'}^{\pm} \rangle$  is finite. The calculation of all possible  $M_{\vec{g}'\vec{g}}^{\pm\pm}$  is quite fast for layers with only one atom per unit cell (Bravais layers), but for composite layers (i.e. layers with  $N_a > 1$  atoms per unit cell) the computing time scales with  $N_a^3$ .

Having all necessary layer diffraction matrices  $M_{\vec{g}'\vec{g}}^{\pm\pm}$  calculated, a total reflection matrix  $R_{a0}^{-+}$  of the surface has to be computed ( $R_{g0}^{-+} = A_g^-$ ). This can either be done perturbationally as in *renormalized forward scattering* [13] or self-consistently through matrix inversions using the *layer stacking* formalism [13, 21]. In this work the layer stacking method was used for all performed calculations. The idea behind this method is quite simple: To describe the diffraction from a stack of two layers, the corresponding layer diffraction matrices are combined. To achieve that, multiple scattering between the two layers has to be considered, which leads to a converging geometrical series of contributions to the reflection and transmission matrices of the stack. Consequently, the total diffraction matrix of the stack can then be computed numerically. The whole crystal can therefore be built up by adding one atomic layer after the other. This layer

stacking sequence has to be continued until - due to damping of the electron beam inside the crystal - the transmitted intensity into the crystal is zero. The intensity  $I_g$  of a diffracted beam  $|\vec{k}_g\rangle$  is then given by

$$I_g = |R_{g0}^{-+}|^2 = |A_g^-|^2 \quad (2.6.17)$$

### 2.6.2 Temperature dependent phase shifts

The decrease in the LEED beam intensities due to thermal effects can not be directly described by the use of an overall Debye-Waller factor as discussed in Sec. 2.5.4. Although this method is applicable in X-ray diffraction, in LEED the wave field has to be time-averaged after each scattering event, since multiple scattering is very pronounced. Therefore, immediately after scattering from a vibrating atom the intensity of the electron wave has to be reduced by the Debye-Waller factor  $e^{-2M}$ . In this approximation different atoms in the lattice were considered to vibrate completely independently, which is clearly not totally correct but a sufficiently accurate description for LEED. In order to preserve the correct phase of the scattered wave, the Debye-Waller factor is included in the atomic scattering factor  $f(E, \theta)$ , which is replaced by  $f(E, \theta)e^{-M}$ . Similarly to Eq. (2.6.11) this effective atomic scattering factor can - in case of isotropic vibrational amplitudes - be written as

$$f(E, \theta)e^{-\frac{1}{2}|\vec{g}|^2\langle(\Delta\vec{r})^2\rangle} = -\frac{1}{k} \sum_l (2l+1)t_l(E, T)P_l(\cos\theta) \quad (2.6.18)$$

By inverting Eq. (2.6.18) the temperature dependent t-matrices  $t_l(E, T)$  can be determined and, consequently, temperature-dependent phase shifts  $\delta_l(T)$  are obtained due to the relation (2.5.20). Since all  $\delta_l(T)$  are now complex with a positive imaginary part  $\delta_{li}(T)$ , the wave scattered from a vibrating atom shows a reduced amplitude as sketched in the following term

$$e^{-2\delta_{li}(T)} e^{i2\delta_{lr}(T)} h_l^{(1)}(kr) \quad (2.6.19)$$

which represents the loss of coherent intensity due to thermal vibrations.

## 2.7 Comparison between theory and experiment

The procedure to solve the LEED problem theoretically was described in Sec. 2.6 and results in  $I-V$  spectra, which have to be compared with the experimental ones. The goal of every LEED analysis is to find the optimal model structure, which shows the best agreement between theory and experiment. For obvious reasons it is necessary to judge the amount of agreement in an objective and quantitative manner rather than by visual evaluation. The demands on a proper criterion, however, are quite high, since it should more or less ignore differences due to inaccurate measurements but assess the agreement of every peak-position, which is caused by a real scattering effect. To account for that, various means of quantification have been proposed, which are generally called reliability factors ( $R$ -factors).

### 2.7.1 Reliability factors

A very commonly used  $R$ -factor, especially in older publications, is the  $R_2$ -factor, which evaluates simply the square deviation between experimental and theoretical  $I-V$  spectra

$$R_2 = \frac{\int (I_{exp} - c I_{th})^2 dE}{\int I_{exp}^2 dE}, \quad c = \frac{\int I_{exp} dE}{\int I_{th} dE} \quad (2.7.1)$$

where the constant  $c$  serves to normalize the curves to each other and is in general recalculated for every single beam. The total  $R$ -factor is finally obtained by a summation of all single-beam  $R$ -factors, which are scaled by their corresponding energy range. The  $R_2$ -factor focuses on relative peak heights only and is therefore quite sensitive to the main peaks but rather insensitive to smaller maxima.

Since the existence and the position (on the energy-axis) of a rather small maximum also contains valuable information about the investigated geometrical structure, a different  $R$ -factor was proposed by Pendry [15], which attempts to treat all maxima and minima with equal weight:

$$R_{Pe} = \frac{\int (Y_{exp} - Y_{th})^2 dE}{\int (Y_{exp}^2 + Y_{th}^2) dE}, \quad Y = \frac{L}{1 + V_{0i}^2 L^2} \quad \text{and} \quad L = \frac{1}{I} \frac{dI}{dE} \quad (2.7.2)$$

Pendry's  $R$ -factor is based on the logarithmic derivative  $L$  of the  $I-V$  spectra, which is modified into the function  $Y$  to avoid singularities for  $I = 0$ . Since  $R_{Pe}$  is the most

commonly used  $R$ -factor today and exclusively used throughout this work, its typical values are discussed in the next paragraph.

Possible values of Pendry's  $R$ -factor range between 0 and 2, where 0 represents perfect agreement and 2 stands for total anticorrelation. In general, an agreement that resulted in  $R_{Pe} < 0.2$  is considered to be sufficiently good. However, one has to be aware that the best possible value depends strongly on the investigated surface structure. While for clean single crystals  $R_{Pe}$ -factors below 0.1 can be achieved rather easily, for so-called *open* surfaces, as in *missing-row* reconstructions, the best possible  $R_{Pe}$  is typically above 0.2 (cf. Ref. [23]).

### 2.7.2 Error estimation

After having found a best-fit structure for a certain surface configuration, following the procedures described in Sec. 2.9, it is of essential importance to have an idea about the possible errors involved. To estimate the possible error of a given model the variance of Pendry's  $R$ -factor can be used. This variance is derived from statistical considerations and defined as [15]

$$var(R_{Pe}) = R_{D_e}^{min} \cdot \sqrt{\frac{8V_{0i}}{\Delta E}} \quad (2.7.3)$$

where  $R_{D_e}^{min}$  represents the  $R$ -factor of the best-fit structure,  $V_{0i}$  the imaginary part of the inner potential and  $\Delta E$  the total energy range of all analyzed  $I$ - $V$  spectra. Every model that results in an  $R$ -factor below  $R_{D_e}^{min} + var(R_{Pe})$  has to be considered as a possible correct representation of the real surface structure. Consequently, the error bar of a single parameter is determined by moving it away from its best-fit value and reoptimizing all other parameters until a minimum of the  $R$ -factor is found. This procedure has to be repeated until the final  $R$ -factor lies outside of  $R_{D_e}^{min} + var(R_{Pe})$ , which then yields the error bar of the according parameter. For complex structures, which naturally contain a lot of free parameters, however, the error bar determination described above is extremely time-consuming, therefore the practical approach is to simply skip the reoptimization of the other parameters, which results of course in smaller error bars. The difference between the original error bar determination and the simplified one is found to be roughly a factor 2 [24], which is acceptable since the error bars obtained from Pendry's variance were assessed to be too large anyway [25].

## 2.8 The Tensor LEED approximation

After having developed the theoretical tools to calculate LEED  $I$ - $V$  spectra in Sec. 2.6 and introduced a quantitative method to compare measured and theoretical results in Sec. 2.7, all the necessary means are provided to perform a successful quantitative LEED analysis of an in principle arbitrarily complex structure. However, fundamental problems are encountered in the application of LEED to complex systems. Firstly, the computational effort to simulate a set of  $I$ - $V$  spectra scales as  $N^3$  ( $N$  equals the number of atoms in the surface unit cell). Secondly, the simultaneous optimization of many parameters, which automatically becomes necessary if large and complex unit cells are considered, also gets very time-consuming and results in an additional exponential increase of the computing time with the number of free parameters. Although the available program codes for full-dynamical LEED calculations became faster and faster, a reliable structural analysis by LEED was restricted to rather simple reconstructions or adsorbate structures for a long time. An additional problem was caused by the manual search of the parameter space, since due to the possible coupling of some parameters, the variation of one parameter at a time often led to an only local  $R$ -factor minimum.

To tackle the problems outlined above, the tensor LEED approximation was developed [17, 18, 26], which based on some concepts used in X-ray scattering: Since the interaction of X-ray photons with matter is weak (i.e. the atomic scattering cross-section is several orders of magnitude smaller than the physical cross-section), the effect of the investigated crystal on the incident photon wave-field can be treated as a first order perturbation, which leads to a direct relationship between the atomic positions  $R_j$  and the scattered wave-field. In LEED, however, the atomic scattering is strong (i.e. the corresponding cross-section is comparable to the physical cross-sectional area) and, consequently, the crystal surface cannot be interpreted as first order perturbation of the incident electron wave-field. The idea behind tensor LEED is therefore to apply perturbation theory to a full-dynamically calculated *reference* LEED wave-field, which is generated by diffraction from a particular reference structure. Provided that only small atomic displacements with respect to the reference structure are considered, the changes induced in the reference wave-field are also small and the modified  $I$ - $V$  spectra can indeed be calculated by first order perturbation theory. The main benefit of this approach is that the computing time required for the calculation of the LEED wave-fields of these distorted structures scales only linearly with  $N$ , thus dramatically speeding up the quantitative LEED analyses. The use of tensor LEED and of the according search-algorithms therefore enabled the treatment of very complex surface structures (including oxides) and is implemented in most of the standard LEED program packages [27, 28] available today.

### 2.8.1 Theory of tensor LEED

Since in the tensor LEED approach a trial structure is considered as a perturbation of a given reference structure, the final goal is to relate the plane wave LEED amplitudes caused by the trial surface  $\tilde{A}_s^-$  to the reference ones  $A_s^-$ . The basic idea is that any minor structural modification of one particular lattice site  $i$  can be described by a change of the local scattering property - i.e. the atomic  $t$ -matrix  $t_i$ .

$$t_i \longrightarrow \tilde{t}_i = t_i + \Delta t_i \quad (2.8.1)$$

Inserting Eq. (2.8.1) in Eq. (2.6.13) leads to the T-matrix of the modified surface  $\tilde{T}$

$$\tilde{T} = \sum_i \tilde{t}_i + \sum_i \sum_{j, j \neq i} \tilde{t}_i G_0 \tilde{t}_j + \dots \quad (2.8.2)$$

which can easily be transformed into a power series in  $\Delta t_i$ , assuming the absolute convergence of Eq. (2.8.2)

$$\tilde{T} = T + \sum_i (1 + T_i^{start} G_0) \cdot \Delta t_i \cdot (1 + G_0 T_i^{end}) + O[(\Delta t_i)^2] \quad (2.8.3)$$

with

$$T_i^{start} = T_i = \sum_{j, j \neq i} t_j G_0 t_i + \dots \quad \text{and} \quad T_i^{end} = T_i = \sum_{j, j \neq i} t_i G_0 t_j + \dots \quad (2.8.4)$$

The definition of  $T_i^{start}/T_i^{end}$  as being the sum of all scattering paths that do not start/end with a scattering event at the atom  $i$  is a direct consequence of the rule that two successive scattering events at the same atom are forbidden, since the atomic  $t$ -matrices already contain all possible multiple scattering events within a given atom. As long as the perturbations  $\Delta t_i$  are sufficiently small, the terms of higher order in  $\Delta t_i$  can be neglected in Eq. (2.8.2) and  $\tilde{T}$  becomes equal to the reference T-matrix  $T$  modified by all possible scattering paths that include exactly one scattering event at the deviation  $\Delta t_i$ .

The LEED amplitudes diffracted from the modified surface  $\tilde{A}_s^-$  are therefore given as

$$\tilde{A}_s^- = \langle k_a^- | 1 + G_0 \tilde{T} | k_0^+ \rangle = A_s^- + \sum_i \Delta A_{g,i} \quad (2.8.5)$$

with

$$\Delta A_{g,i} = \langle \vec{k}_g^- | G_0 (1 + T_i^{start} G_0) \cdot \Delta t_i \cdot (1 + G_0 T_i^{end}) | \vec{k}_0^+ \rangle \quad (2.8.6)$$

Consequently, the modified amplitudes  $\tilde{A}_g^-$  depend exclusively on the variations of the atomic  $t$ -matrices  $\Delta t_i$  and some quantities that can be directly obtained in the reference calculation. Therefore, once a full-dynamical LEED calculation for a given reference structure has been performed, the computation time for  $I$ - $V$  spectra of related structures scales only linearly with  $N$ .

The best way to calculate the so-called *delta-amplitudes* of Eq. (2.8.6) is in angular momentum representation, which yields after the insertion of the closure relation  $\sum_{lm} |lm\rangle \langle lm| = I$

$$\Delta A_{g,i} = \sum_{l'm',lm} T_{g,i}^{l'm',lm} \cdot \langle l'm' | \Delta t_i | lm \rangle \quad (2.8.7)$$

with

$$T_{g,i}^{l'm',lm} = \langle \vec{k}_g^- | G_0 (1 + T_i^{start} G_0) | l'm' \rangle \cdot \langle lm | 1 + G_0 T_i^{end} | \vec{k}_0^+ \rangle \quad (2.8.8)$$

where  $T$  is a tensor that depends only on the reference structure and is computed during the full-dynamical calculation (cf. Ref. [28]). It is this tensor  $T$ , by the way, that gave tensor LEED its name. The only thing missing so far is a quantitative description of the changes in the atomic  $t$ -matrices  $\Delta t_i$ , which is addressed in the next paragraphs.

### 2.8.1.1 Geometrical modifications

The most frequent application of tensor LEED is clearly the calculation of LEED intensities of trial structures that show a slightly different geometry compared to the reference structure, since the primary goal of LEED is the structural determination of surfaces. If an atom  $i$  is shifted by an amount  $\Delta \vec{R}_i$ , then the corresponding atomic scattering potential changes to  $V_i(|\vec{r} - (R_i + \Delta R_i)|)$ , whose scattering effect is still represented by the same atomic  $t$ -matrix  $t_i$ . The geometrical changes involved can be accounted for by the use of a quantum mechanical translation operator  $\tau(\Delta \vec{R}_i)$ , which is in principle the free-particle propagator to  $\Delta \vec{R}_i$ , leading to:

$$\Delta t_i = \tilde{t}_i - t_i = \tau(-\Delta \vec{R}_i) t_i \tau(\Delta \vec{R}_i) - t_i \quad (2.8.9)$$

The numerical details on how to calculate  $\Delta t$  in practice, however, can be found in Refs. [26, 29, 30]. The validity range of the tensor LEED approximation for geometrical

displacements was found to be  $\pm 0.4 \text{ \AA}$  [26], but can be worse in case of very strong scatterers or simultaneous, profound modifications of adjacent atomic positions.

### 2.8.1.2 Vibrational variations

As pointed out in Sec. 2.6.2, the effect of thermal vibrations is most conveniently represented by the use of temperature dependent phase-shifts or, consequently, by a temperature dependent  $t$ -matrix. Therefore a change in the vibrational amplitude of an atom  $i$  from  $A_{vib,i}$  to  $\tilde{A}_{vib,i}$  corresponds simply to the following change in the  $t$ -matrix

$$\Delta t_i = t_i(\tilde{A}_{vib,i}) - t_i(A_{vib,i}) \quad (2.8.10)$$

which can be described within the framework of tensor LEED. Consequently, the validity of thermal tensor LEED is only restricted by the accuracy of the determination of the temperature dependent  $t$ -matrices themselves - i.e. the number of angular momentum quantum numbers  $l$  used for the inversion of Eq. (2.6.18) [31].

### 2.8.1.3 Chemical changes

Also chemical variations can be treated using the tensor LEED formalism. The basis for this is provided by the *average t-matrix approximation* (ATA) [32, 33, 34], which assumes that for a given lattice site  $i$  randomly occupied by two different elements A and B an *effective*  $t$ -matrix  $t_i^{ATA}$  can be used:

$$t_i^{ATA} = c_i^A \cdot t_i^A + c_i^B \cdot t_i^B, \quad c_i^A + c_i^B = 1 \quad (2.8.11)$$

where  $c_i^A$  and  $c_i^B$  represent the according probabilities of occupation.

Assuming a change of the occupation-probability of element A in the lattice site  $i$  from  $c_i^A$  to  $\tilde{c}_i^A = c_i^A + \Delta c_i^A$  results in a corresponding modification of the  $t$ -matrix, which is given as

$$\Delta t_i = \tilde{c}_i^A \cdot t_i^A + (1 - \tilde{c}_i^A) \cdot t_i^B - t_i^{ATA} = \Delta c_i^A (t_i^A - t_i^B) \quad (2.8.12)$$

Using Eq. (2.8.12), chemical changes can be treated similar to geometrical displacements within the tensor LEED approximation [35, 36]. The validity of ATA and its

application to tensor LEED has been shown in various publications, where LEED results for the chemical composition of the first atomic layer of a surface were compared to results obtained from complementary methods (cf. e.g. [37, 38]). Even randomly distributed vacancies or adsorption positions can be described within this formalism by mixing the atomic  $t$ -matrix of the corresponding element with a trivial - non-scattering - contribution (i.e. a  $t$ -matrix that describes no scattering event).

## 2.9 Structural search

Once a full-dynamical LEED calculation for a certain reference structure has been performed and all possible changes in the amplitudes  $\Delta A_{g,i}$  are computed according to Eq. (2.8.6), all that is needed is an appropriate search algorithm that enables the determination of the global  $R$ -factor minimum in the shortest possible time. Since the number of free parameters  $pf$  often exceeds ten even for very simple structures, assuming ten grid steps for every parameter already results in more than  $10^{10}$  possible trial structures. Therefore, it's clearly not feasible to compare the  $I$ - $V$  spectra of every trial structure with the experimental ones in order to sort out the *best-fit* structure. The easiest approach to solve that problem is to employ a local search algorithm that simply follows the gradient of the  $R$ -factor starting from a given configuration until the nearest local minimum is found. The advantage of this method is its fast convergence, but the big disadvantage lies in the complexity of the  $R$ -factor hypersurface itself, since due to all the multiple scattering events and the rather large number of free parameters a lot of local minima can occur. Therefore using the previously described algorithm one often gets stuck in a local minimum instead of finding the desired global one. Consequently, a more sophisticated search algorithm is needed.

In the TensErLEED program package [28] used throughout this work, however, a totally different search strategy is employed [39]. As a starting point a random set of trial structures, belonging to the considered parameter space, is generated, followed by an independent determination of the  $R$ -factor minimum for every single starting structure. The search strategy itself differs quite distinctively from the one described above, since every new parameter-set is generated randomly, using a Gaussian probability distribution centered at the current trial structure. If the overall  $R$ -factor of the new structure is lower than the former one, the next jump is based on this new structure, otherwise the previous step is repeated. This procedure is reiterated until a certain number of trial structures - typically about 20% - have converged into the same structural minimum, which is then considered to be the true global minimum. Using this Gaussian probability distribution for the determination of each new parameter-set results in rather large parameter changes for large  $R$ -factors (i.e. a quasi global behavior of the search algorithm), whereas for a small  $R$ -factor only configurations

in the vicinity of the current one are considered (i.e. a quasi local behavior close to the  $R$ -factor minimum). In other words the search algorithm implemented in the TensErLEED program package (computing time proportional to  $p_f^{2.5}$ ) constitutes a very good compromise between a truly global simulated annealing algorithm [40], which scales with  $p_f^6$ , and a simple local one, which scales with  $p_f^2$ .

The convergence properties of the algorithm used in this work, however, depends strongly on the number and nature of the free parameters  $p_f$ . While for  $pf < 10$  convergence is very fast (some hundred iterations), for  $pf > 15$  proper convergence cannot always be achieved, especially if a lot of parameters are involved that effect the  $I-V$  spectra only very weakly. Despite that the *best-fit* structures described by the final parameter-set are in general at least very similar and can be considered to be very close to the true *best-fit* structure (within the error bars determined by LEED), which is a sufficiently good result, especially if one considers very complex structures like some of the oxides described later in this work.

### 3 Other surface analysis techniques

Since the determination of a complex structure by LEED alone is more or less impossible, some other, complementary methods have been used to gain more information about the investigated structures. The ability to take real-space images by scanning tunneling microscopy (STM) can be very helpful to identify certain structural features unique to the investigated surface. Information on the chemical surface composition can be obtained by Auger electron spectroscopy (AES). All those additional experimental results simplify in general the creation of a meaningful reference structure considerably. The most important contributions for this work, however, came from state of the art molecular dynamics calculations based on density functional theory (DFT) - all of the models proposed by this method could be confirmed by LEED as described within this work. Also surface X-ray diffraction (SXRD) experiments were performed, due to the possibility to restrict the analysis to the first atomic layer, which was very helpful for the structural determination of the incommensurate surface oxide layer on Pd(111). All the different methods mentioned above were involved in the structural determination process of the vanadium and palladium surface oxides analyzed within this work and are therefore described in the following sections.

#### 3.1 Scanning tunneling microscopy

The development of scanning tunneling microscopy (STM) in the years 1978-81 - by Gerd Binnig and Heinrich Rohrer in the IBM research laboratories in Ruschlikon - was definitely one of the major advances in surface science in the last century and was awarded with the Nobel price for physics already in the year 1986. Within the two decades since its invention STM had led to a revolution in studies of solid surfaces due to its ability to deliver atomically resolved real-space images of an investigated surface, which are often quite straightforward to understand.

The physical concept behind the operating mode of an STM is based on the rather well-know quantum mechanical tunneling effect, i.e. the tunneling of electrons between a small probe (STM-tip) and a conductive sample that occurs for a sufficiently small tip-sample distance. The idea is to approach a conducting surface with a perfect tip (in most cases: tungsten) until a certain tunneling current is obtained. Most of the STMs are then operated in constant current mode, which means that a feedback loop controls the tunneling current and keeps it constant by removing the tip slightly for higher values and by approaching the surface for lower values. Moving the tip around on the surface under this condition causes the tip to follow the topography of the surface in an approximately constant distance. Therefore, scanning the surface in  $x$

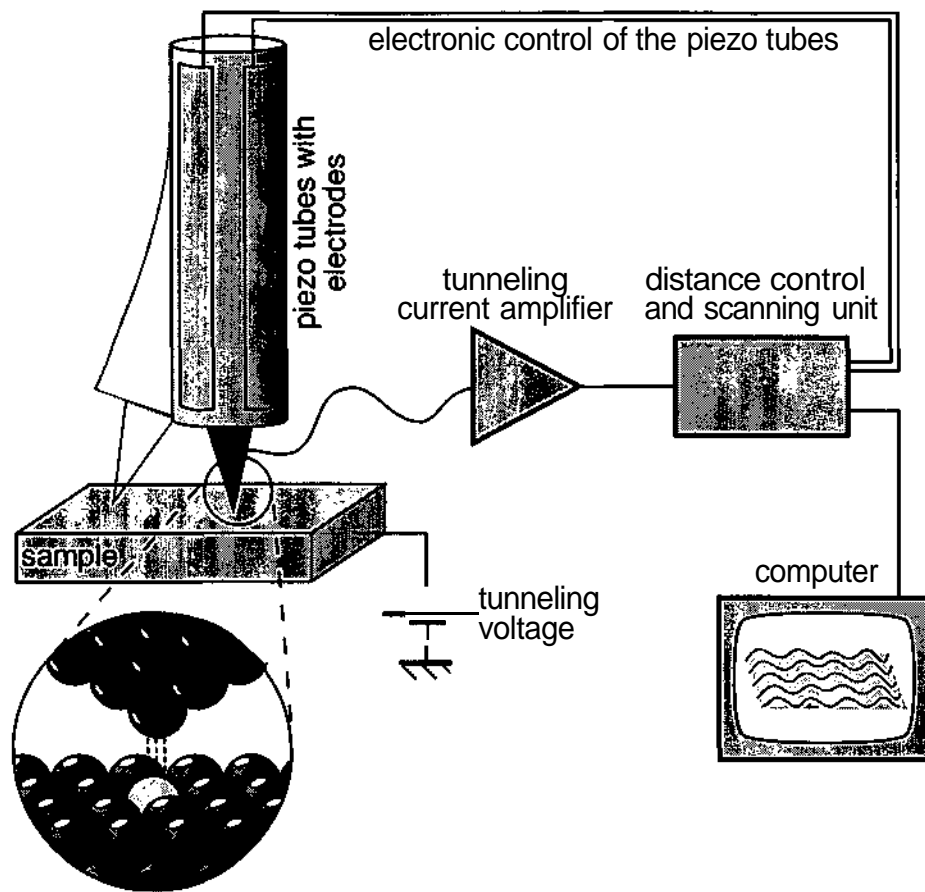


Figure 3.1.1: Schematic of the operating mode of a scanning tunneling microscope [41].

and  $y$  direction by means of piezo-tubes and simultaneously recording the according tip-sample distance, results in an image of the topography of the surface (cf. Fig. 3.1.1).

A very simple model, which describes the tunneling process, is depicted in Fig. 3.1.2. In this approximation the tunneling barrier is represented by a one-dimensional rectangular potential, which yields, according to the time-independent Schrödinger equation

$$\left(-\frac{\hbar^2}{2m_e}\nabla^2 + V(z)\right)\psi(z) = E\psi(z), \quad (3.1.1)$$

for the region inside the barrier an exponentially decreasing wave-function

$$\psi(z) \propto e^{-\kappa z}, \quad K = \sqrt{\frac{2m_e\phi}{\hbar^2}} \quad \text{and} \quad \phi = V - E \quad (3.1.2)$$

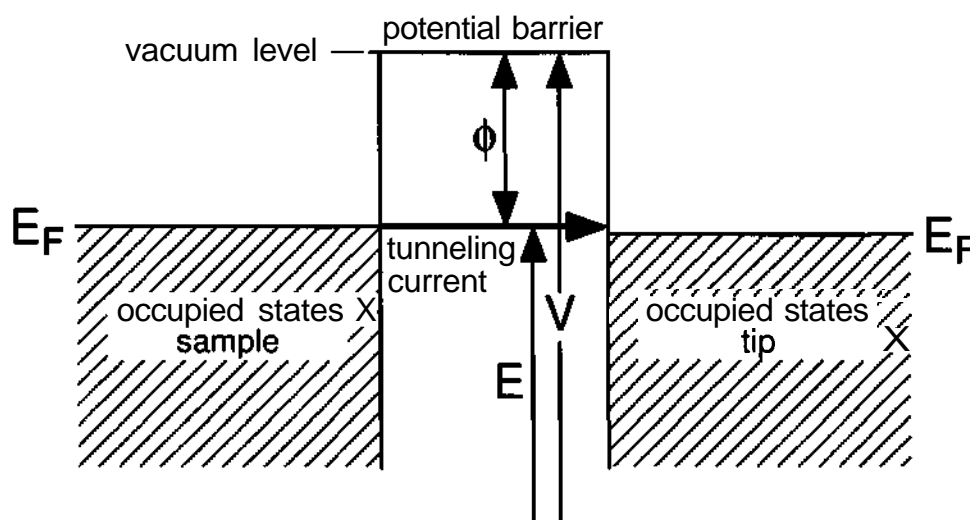


Figure 3.1.2: Schematic of the tunneling process between tip and sample, for a very small negative sample voltage. Electrons of occupied states of the surface are tunneling into unoccupied states of the tip.

The value of  $\phi$  in Eq. (3.1.2) is equal to the work function, since only electrons close to the Fermi-edge are considered. Consequently, the probability of transmission of a single electron through a potential barrier of the thickness  $d$  is approximately

$$T \propto |\psi(d)|^2 \propto e^{-2\kappa d} \quad (3.1.3)$$

In other words the tunneling current itself depends exponentially on the tip-sample distance, i.e. a change of  $1 \text{ \AA}$  in the distance results in a change of the current by a factor 5-10 (depending on the work function). An STM operating in constant current mode is therefore able to resolve the topography of a given surface with an accuracy of  $1/100 \text{ \AA}$  in the 2-direction. The lateral resolution, however, is restricted by the piezo-tubes and therefore clearly lower ( $\approx 1/10 \text{ \AA}$ ).

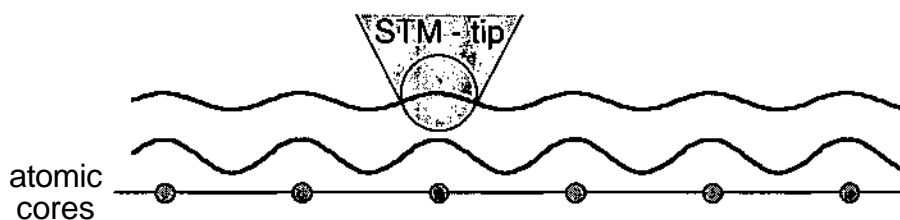


Figure 3.1.3: An STM operating in constant current mode images areas of constant density of states.

What is clear, already from this very simple approach, however, is the fact that STM maps the electronic structure of a surface (i.e. the density of states at the Fermi-edge), not the true geometric structure (cf. Fig. 3.1.3). That's why certain adsorbates, sitting on the surface, are sometimes imaged as depressions [42, 43]. Additionally, for very small tip-sample distances the electronic interaction between tip and sample has to be taken into account, since an unintentional, profound change in the surface structure can occur due to this interaction [44]. Information on a more sophisticated theoretical treatment of the STM imaging process can be found in Refs. [42, 45].

However, the advantages of STM are very obvious: Firstly, STM directly delivers real-space images of conducting surfaces. Secondly, no long range ordering is necessary to obtain information on the investigated structures. Last, but not least, even chemical contrast is possible for certain elements.

### 3.2 Auger electron spectroscopy

Another very important technique in surface science is Auger electron spectroscopy (AES), mainly due to its sensitivity to the chemical composition of the sample in the surface area. The physical reason for the surface sensitivity of AES is based on the inelastic mean free path of the Auger electrons (escape depth). Since the energy range usually analyzed in an Auger analysis lies between 10 and 1000 eV, the according escape depth of the electrons is 5-10 Å (Fig. 3.2.1), i.e. only information about the composition of the first 3-6 atomic layers can be obtained. The chemical sensitivity, however, is inherent to the Auger process itself.

For AES, an electron beam is accelerated towards the sample by applying a rather high voltage (3 kV in this work). Due to the high kinetic energy of the impinging electrons, scattering events can cause the ejection of some core level electrons from the atoms, leaving vacant core holes, that are preferentially repopulated by an Auger transition; i.e. an electron of a higher shell fills the core hole, at the same time the corresponding energy gain is transferred to another electron (most likely of the same shell), which can then leave the crystal (Fig. 3.2.2).

Consequently, the kinetic energy of an Auger electron  $E_A$  can be approximated [for the example given in Fig. 3.2.2(a)] by

$$E_A = (E_K - E_{L1}) - E_{L2} \quad (3.2.1)$$

for positive binding energies related to the vacuum level. For more accurate calculations, however, one has to consider the shift in the energy levels caused by the ionization

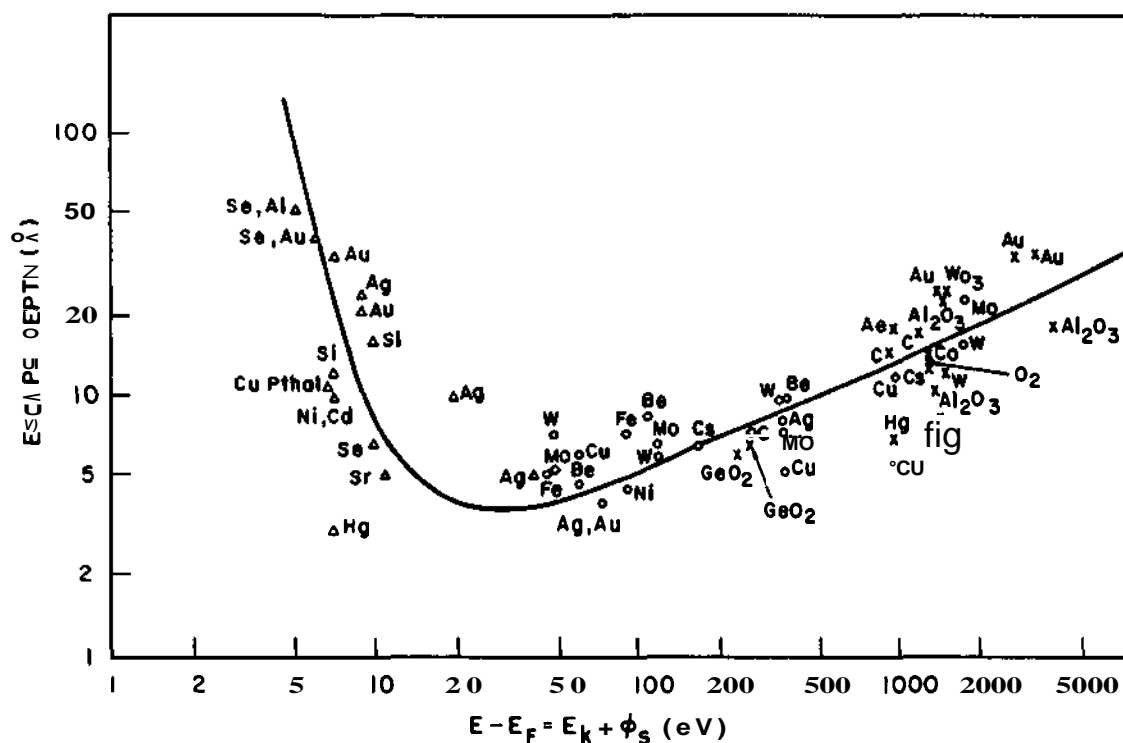


Figure 3.2.1: Inelastic mean free path of electrons in a solid in dependence of the electron energy [46].

of the atom. Nevertheless, the energy of an Auger electron  $EA$  is determined exclusively by the core levels of the corresponding atom and is therefore very characteristic for every single element. In case of an Auger process involving electrons of the valence band [cf. Fig. 3.2.2(c)], a broadening of the according Auger electron energies can be observed, which shows a characteristic shape caused by the density of states in the valence band, giving direct information on the chemical bonding.

In practice, all that is needed for AES is an electron source and an energy analyzer for the Auger electrons (a cylindrical mirror analyzer was used throughout this work). Due to the high background, caused by the inelastically scattered primary and Auger electrons, usually the derivative of an Auger spectrum is used to determine Auger-peak-to-peak-heights (APPH), i.e. the difference between maximum and minimum of a certain peak in the obtained spectrum. However, the exact APPH-values depend on many parameters unique to every set-up and can therefore not be directly compared. Most of the time relative APPHs are given, which in general relate an Auger peak of a certain element to the main peak of the substrate and are therefore a measure for the coverage or impurity. A quantitative determination of the coverage of a certain element, however, is very difficult and usually standard spectra are used as reference. Another disadvantage of AES is the fact that some elements show Auger transitions

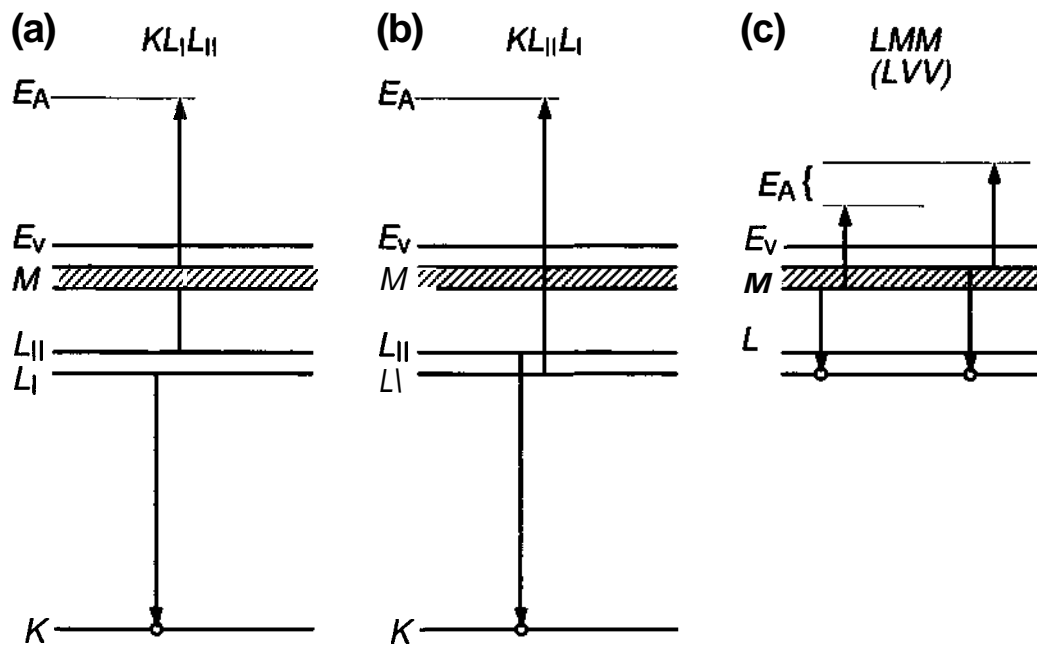


Figure 3.2.2: Auger process for an element of the third period. Energies of the Auger-electrons  $E_A$  created in a  $KL_I L_{II}$  (a) and a  $KL_{II} L_I$  (b) transition are in a first approximation the same. For transitions involving the valence band LVV (c) the energy uncertainty equals twice the valence band width [41].

of more or less the same energy and are therefore impossible to differentiate, whereas hydrogen shows no Auger transition at all and can therefore not be detected by AES.

### 3.3 Surface X-ray diffraction

X-ray diffraction has been widely used since the 1960s to study structural bulk-properties of crystalline materials. One of the biggest advantages is that X-rays interact only weakly with matter and a single scattering approach is therefore sufficient to reproduce the experimental data. Its application to surfaces, however, took a little bit longer, mainly because of the low signal rates involved. Since intense X-ray sources are needed for a proper surface analysis, the activity in the field of surface X-ray diffraction (SXRD) scaled with the number of synchrotron X-ray facilities and started to boom in the late 1980s.

One direct consequence of the applicability of a kinematic theory (single scattering) is that fractional order superstructure reflections caused by a reconstructed surface or an overlayer are only influenced by those layers at the surface with corresponding periodicity. Hence, by analyzing these reflections X-ray diffraction is only sensitive to

the surface. Consequently, the in-plane arrangement of incommensurate surface structures can be determined completely independently of the bulk structure, which is a big advantage that was used for the analysis of the palladium surface oxide described in Sec. 5.3.5. In order to reduce the thermal diffuse scattering from the bulk, in general grazing incidence of the X-ray beam to the surface is used, thereby limiting the penetration depth into the bulk and therefore the probed crystal volume, i.e. a well collimated beam as provided by synchrotron sources is needed.

In the next paragraph a short summary of the basic formulas used for theoretical calculations in SXRD is given and the differences to LEED are outlined. A more detailed and complete treatment of kinematic diffraction theory, however, can be found in Refs. [47, 48, 49].

### 3.3.1 Differences and similarities between LEED and SXRD

One of the main differences between SXRD and LEED is the fact that X-rays are scattered by electrons rather than by the atomic potential. The amplitude of the scattered field at distance  $R$  is given in the free electron approximation according to Thomson [47] as

$$E' = E_0 \cdot \frac{e^2}{R m_e c^2} \sqrt{P} \quad (3.3.1)$$

where  $E_0$  is the amplitude of the incoming wave  $\vec{E}_0 e^{i\vec{k}\cdot\vec{r}}$  and  $P$  a polarization factor. Consequently, the scattering from an atom, whose electron density is  $\rho_a(\vec{r})$ , is given in analogy to Eq. (2.3.7) as

$$E'_a = \int E' \rho_a(\vec{r}) dV = E_0 \frac{e^2}{R m_e c^2} \sqrt{P} \int \rho_a(\vec{r}) e^{i(\vec{k}-\vec{k}')\cdot\vec{r}} dV \quad (3.3.2)$$

which leads to the definition of an atomic form factor

$$f_a(\vec{k} - \vec{k}') = \int \rho_a(\vec{r}) e^{i(\vec{k}-\vec{k}')\cdot\vec{r}} dV \quad (3.3.3)$$

Applying the above results to a crystal lattice (as described in Sec. 2.3) leads to the following amplitude of the scattered wave

$$E' = E_0 \frac{e^2}{R m_e c^2} \sqrt{P} F(\vec{k} - \vec{k}') \sum_{m,n,o} e^{i(\vec{k}-\vec{k}')\cdot(m\vec{a}_1+n\vec{a}_2+o\vec{a}_3)} \quad (3.3.4)$$

where  $F(\vec{k} - \vec{k}')$  is the form factor (also often termed *structure factor* in literature), which is given as the sum of contributions from every atom in the unit cell

$$F(k - \vec{k}') = \sum_j f_j(k - \vec{k}') e^{i(\vec{k} - \vec{k}') \cdot \vec{r}_j} \quad (3.3.5)$$

Also in SXRD thermal vibrations have to be taken into account, which is realized - as it is in LEED (cf. Secs. 2.5.4 and 2.6.2) - by the inclusion of a Debye-Waller factor, but in this case directly in the structure factor, leading to the final definition of  $F(\vec{k} - \vec{k}')$

$$F(k - \vec{k}') = \sum_j f_j(k - \vec{k}') e^{-\frac{1}{2}|\vec{k} - \vec{k}'|^2 \langle (\Delta \vec{r})^2 \rangle} e^{i(\vec{k} - \vec{k}') \cdot \vec{r}_j} \quad (3.3.6)$$

At this point it is important to mention that it is the structure factor of Eq.(3.3.6), which is simulated by computational codes and compared to experiment. However, not all kinds of momentum transfer  $s = (\vec{k} - \vec{k}')$  are possible and therefore only a restricted number of structure factors has to be calculated. As in LEED only a parallel momentum transfer equal to a reciprocal lattice vector  $\vec{G}(h, k)$  is possible in the two-dimensional case and the peak intensities of the corresponding reflections are given by squaring the amplitudes of Eq. (3.3.4)

$$I_{hk}^{peak}(s_z) = I_0 \frac{e^4}{R^2 m_e^2 c^4} P |F_{hk}(s_z)|^2 N^2 M^2 \quad (3.3.7)$$

Here,  $N \cdot M$  equals the number of surface unit cells probed by the X-ray beam. Since the peak intensities are strongly affected by the quality of the crystal and the collimation of the X-ray beam, in practice integrated intensities of the reflections are used, which can be determined much more accurately. An integrated intensity is measured in a scan, which starts somewhere at background level, passes the peak and ends up again at background level (cf. Fig. 3.3.1). The background subtracted total sum of detected photons is then a measure of the integrated intensity, which can be directly related to the square of the structure factor [49]

$$I_{hk}(s_z) = I_0 \frac{e^4}{m_e^2 c^4} \frac{A \lambda^2 P}{\Omega a \sin 2\theta} |F_{hk}(s_z)|^2 \frac{\hbar}{2\pi} \Delta s_z \quad (3.3.8)$$

where  $A = aNM$  is the area of the surface participating in the diffraction experiment,  $\Delta s_z$  the resolution of the detector arrangement in the direction along the Bragg rods and  $\Omega$  the angular velocity of the crystal rotation. As a result of Eq. (3.3.8), the integrated intensities depend on the experimental setup.

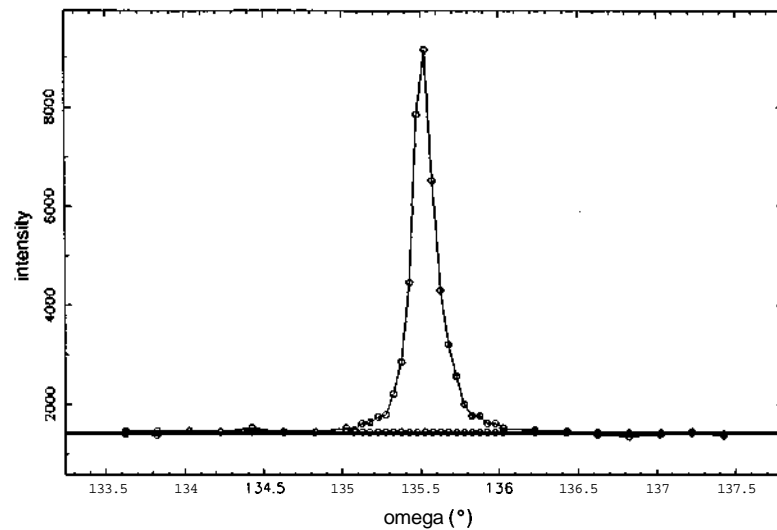


Figure 3.3.1: Omega scan of a superstructure reflex  $[(-2,-1)]$  of the second domain] of the surface oxide on Pd(111). The black line indicates the background level, which has to be subtracted before integration.

For a high quality dataset as many reflections as possible have to be measured and symmetry equivalent reflections have to be averaged. The set of integrated intensities can then be transformed into a corresponding set of structure factors using Eq. (3.3.8). The quality of a proposed structural model, however, is in most cases determined via

$$\chi^2 = \frac{1}{N - p_f} \sum_{h,k} \left( \frac{|F_{hk}^{calc}|^2 - |F_{hk}^{exp}|^2}{\sigma_{hk}} \right)^2 \quad (3.3.9)$$

where  $N$  is the number of structure factors,  $p_f$  the number of free parameters in the model and  $\sigma_{hk}$  the uncertainties of  $|F_{hk}^{exp}|^2$ . The refinement of the atomic positions in the model is then performed by minimizing  $\chi^2$ , where a value of  $\chi^2 \sim 1$  is considered as a very good agreement of the proposed model.

### 3.3.2 Crystal truncation rods

While structure factors calculated the way describe above can just be directly applied to fractional order reflections, where no bulk contribution has to be taken into account, all the information on the stacking and on the bulk structure is contained in the integer order reflections. These are also called crystal truncation rods (CTR), because the continuous variation of the intensity of these reflections in dependence on the momentum transfer perpendicular to the surface originates from the truncation of the surface. In order to simulate such CTRs one has to calculate the total structure factor

of an integer order reflection, which is given by the sum of contributions from the surface and the bulk:

$$F_{sum} = F_{surf} + F_{bulk} \quad (3.3.10)$$

with

$$F_{surf} = \sum_j^{surf \text{ unit cell}} f_j(\vec{s}) e^{-\frac{1}{2}|\vec{s}|^2 \langle (\Delta\vec{r})^2 \rangle} e^{i\vec{s} \cdot \vec{r}_j} \quad (3.3.11)$$

The calculation of the bulk structure factor is a little bit more complicated since it consists of phase-shifted contributions from every atomic layer, which are attenuated with increasing penetration depth, due to absorption (cf. the LEED analogon in Sec. 2.4.2). Therefore the final bulk value amounts to:

$$F_{bulk} = \frac{1}{1 - e^{-i2\pi l} e^{-a}} \sum_j^{bulk \text{ unit cell}} f_j(\vec{s}) e^{-\frac{1}{2}|\vec{s}|^2 \langle (\Delta\vec{r})^2 \rangle} e^{i\vec{s} \cdot \vec{r}_j} \quad (3.3.12)$$

where  $a$  is the attenuation factor and  $l$  is the part of the momentum transfer in the direction of  $a_3$ . Consequently, the intensity is very high for integer values of  $l$ , but due to the termination of the crystal even for non-integer values there is finite intensity. Finally, the comparison of calculated and measured CTRs can be used to extract information about the inter-layer distances and the stacking. It should be mentioned, however, that, in contrast to LEED, SXRD is very sensitive to the in-plane coordinates, but rather large error bars are involved in the determination of out-of-plane distances.

## 4 Experimental

### 4.1 Setups used for this work

The LEED and STM experiments were carried out in Vienna in two different ultra high vacuum (UHV) chambers with base pressures in the low  $10^{-11}$  mbar range. The hydrogen pressure in particular was below  $10^{-11}$  mbar, which turned out to be quite important for the stability of the prepared surface oxides. The setup used for STM measurements consists of two separate chambers: A preparation chamber, showing a slightly worse base pressure ( $< 10^{-10}$  mbar) and a main chamber, where the measurements were performed. The preparation chamber contains an ion gun used for sputtering, several gas inlets and evaporators for metal deposition. The main chamber itself contains a customized Omicron micro-STM (operated at room temperature) as well as the facilities to do X-ray photoelectron spectroscopy (XPS), low energy ion scattering (LEIS), qualitative LEED and AES. For a detailed description of the UHV system containing the STM see e.g. Ref. [50]. The setup used for quantitative LEED is also additionally equipped with the instrumentation for AES and ISS, as well as an ion gun, several gas inlets and one evaporator. The AES systems of both chambers consist of an electron gun and a cylindrical mirror analyzer to measure the energy distribution of the emitted electrons. Moreover, information on the chemical composition of the residual gas can be obtained by quadrupole mass spectrometers, which are also present in both setups.

The STM measurements were done using an electrochemically etched tungsten tip, which was cleaned in the preparation chamber by  $\text{Ar}^+$  bombardment. All images presented in this study were taken in constant current mode of the above described STM with the sample at negative voltage (unless otherwise mentioned). For a detailed description of the LEED experiment see Sec. 2.2.

The SXRD experiments were carried out in Grenoble at beam line BM32 of the European Synchrotron Radiation Facility (ESRF). The overall setup at this beam line consists of several UHV chambers interconnected via an UHV transport system, with the X-ray chamber being installed in a shielded hutch. The UHV chamber for SXRD, in particular, is mounted on a  $z$ -axis diffractometer and allows for an in-situ reflection high energy electron diffraction (RHEED) and AES analyzes simultaneously with X-ray irradiation. The base pressure of this chamber, however, was considerably worse compared to the other setups, i.e. in the low  $10^{-10}$  mbar range. The diffractometer was constructed to enable the highest possible precision concerning the sample orientation and the relative movement of the detector. A more complete description of this setup, however, can be found in Ref. [51]. The actual SXRD measurements, however, were

carried out at a photon energy of 18 keV and grazing incidence of the incoming X-ray beam ( $1.5^\circ$ ).

## 4.2 Sample cleaning

To prepare a clean Pd(111) surface, the crystal was sputtered by 1-2 keV  $\text{Ar}^+$  ions. After half an hour of Ar bombardment the sample was heated up to  $600^\circ\text{C}$ , kept at this temperature for 5 min and allowed to cool down to room temperature afterwards. The duration of the whole sputtering cycle was about 1.5 h and was followed by an annealing step at  $800^\circ\text{C}$ . Although at this time the surface was already free from contaminations as sulfur or oxygen according to AES, an additional oxygen treatment was conducted due to the possible existence of residual carbon, which can not be detected on Pd by AES because of the overlap of the main carbon peak at 272 eV with a secondary Pd peak. Accordingly, the crystal was exposed to molecular oxygen ( $2 \times 10^{-7}$  mbar) at  $600^\circ\text{C}$  for 5 min, cooled down to  $100^\circ\text{C}$  in oxygen atmosphere, followed by a flash to  $800^\circ\text{C}$  to get rid of residual impurities. The LEED pattern of a Pd(111) surface cleaned following the procedures described above showed a very bright and sharp ( $1 \times 1$ ) pattern and no visible contaminations, in agreement with the AES results. The oxygen treatment, however, was performed as an initial sample cleaning step only and found to be unnecessary for later oxide preparations. The only exception to this rule was applied for measurements conducted at the ESRF, where this oxygen treatment was always performed due to the slightly poorer quality of the vacuum compared to the other setups.

## 5 The oxidation of Pd(111)

### 5.1 Introduction

Palladium is quite well-known for being a very promising catalyst for applications involving oxidation reactions, since compared with current Pt/Rh catalysts, Pd is more economical and can operate at higher temperatures [52]. But unusual phenomena, that tend to occur in Pd-catalyzed reactions, have delayed the implementation of Pd-based catalysts (e.g. oscillations in the CO oxidation rate at high O<sub>2</sub> to CO ratios). Various models were proposed trying to explain such oscillations, most of them involving a periodic filling and depletion of subsurface oxygen [6, 7], since Pd was believed to be one of the model systems demonstrating the existence of this kind of oxygen species [53, 54, 55]. For the Pd(110) system, however, this model was proved wrong by Bondzie *et al.* [9], showing the oscillations to be caused by the formation and deformation of palladium oxide, questioning the existence of subsurface oxygen. In this respect it might very well be the case, that most of the effects, previously attributed to subsurface oxygen are indeed signs of the formation of a surface oxide. Consequently, a thorough structural analysis of the ordered surface structures that form on Pd(111) due to exposure to oxygen above room temperature was performed, which should give some additional insights into this topic. However, it has already been shown previously that the exposure of clean Pd surfaces to O<sub>2</sub> at room temperature leads to the dissociation of the O<sub>2</sub> molecules and the formation of a chemisorbed oxygen layer. On Pd(111) the adsorbed oxygen atoms form a p(2 x 2) overlayer with a saturation coverage of 0.25 ML (monolayer = adsorbed atoms per substrate atom) [56, 57]. It should be mentioned here that already for this rather simple overlayer the opinions on the oxygen adsorption site are diverging. While Steltenpohl *et al.* [56] claim the hcp 3-fold hollow site to be the favorable one, Seitsonen *et al.* [57] find oxygen adsorption in the fcc sites. This indicates the rather poor characterization of the interaction of palladium with oxygen. Higher oxygen coverages have been obtained at elevated temperatures and higher oxygen pressures [58] or by using stronger oxidants (i.e. NO or NO<sub>2</sub>) [52, 53]. Two different ordered structures have been found in this high coverage regime: A metastable structure [52], which was not investigated during this work, and a very complex one, which showed some indications of the formation of a surface oxide. The atomic structure of these phases, however, could not be determined. It was therefore part of this work to analyze the atomic structure of this complex phase, which was eventually indeed identified as being a surface oxide [59].

Generally speaking, the formation of oxides on metal surfaces has increasingly received attention within the last years, mainly due to the realization that oxides can play an important role in catalysis, even in cases where the catalytic properties were previously

attributed to the metal surface [60]. It has been found that the formation of an oxide on a metal changes not only the surface properties in a profound way, but also serves as a source/sink of oxygen in oxidation/reduction reactions. Despite the fact that under realistic catalytic conditions one is almost always confronted with some kind of oxide, the analysis of oxides was neglected for a long time in surface science due to several reasons. Firstly, the oxides of the more noble metals form only at rather high oxygen partial pressures, which causes an experimental problem since surfaces are traditionally studied in ultrahigh vacuum. Secondly, many oxide structures and surface oxides, in particular, exhibit an atomic arrangement which is difficult to resolve with traditional experimental techniques [61, 62]. The main reason for these difficulties lies in large unit cells or sometimes even incommensurate structures, which exhibit strong buckling of the surface layer and consequently a large number of independent structural parameters. Additionally, oxygen is quite a weak scatterer, which complicates an analysis using traditional diffraction techniques (i.e. LEED and SXRD) even further. Consequently, for the structural determination of the surface oxide a complimentary method was needed that could restrict the number of possible trial structures. Fortunately, due to a collaboration with G. Kresse from the *Centre for Computational Materials Science* in Vienna, theoretical results, obtained by finite temperature molecular dynamics calculations based on density functional theory (DFT), were available and provided the needed final input.

In the following a quantitative LEED analysis of the  $p(2 \times 2)$ -O superstructure on Pd(111) is presented, providing strong evidence in favor of the fcc 3-fold hollow adsorption site. Furthermore, a detailed description of the structure determination process of the PdO-surface oxide is given, including STM and LEED measurements as well as SXRD and DFT analyses. Most of the STM images presented in the following were taken either by C. Konvicka or E. Lundgren already several years ago and the DFT calculations were performed by G. Kresse. As a result of this analysis it is clear that the previous generally accepted assumption, stating that oxygen forms exclusively either overlayers or bulk-like oxides on metal surfaces, is incorrect, because it is shown that the oxidation of a metal surface can also lead to a two-dimensional oxide which is neither related to the metal structure nor to any bulk oxide.

## 5.2 The $(2 \times 2)$ -O phase

### 5.2.1 Preparation

After having cleaned a Pd(111) crystal following the procedures described in Sec. 4.2, dosing molecular oxygen at room-temperature always leads to the formation of a  $p(2 \times 2)$ -O superstructure. Already after exposure to 10 L (Langmuir, where 1 L =

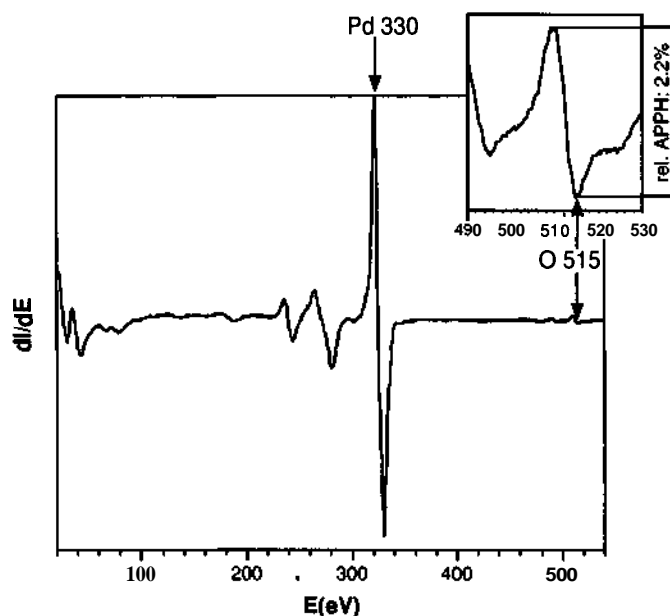


Figure 5.2.1: Auger spectrum of a Pd(111) surface after the adsorption of 10 L of molecular oxygen at  $3 \times 10^{-8}$  mbar  $O_2$ -partial pressure and room temperature. The relative APPH between the O-peak at 515 eV and the main Pd-peak at 330 eV was found to be 2.2%, which corresponds to the saturation coverage of 0.25 ML.

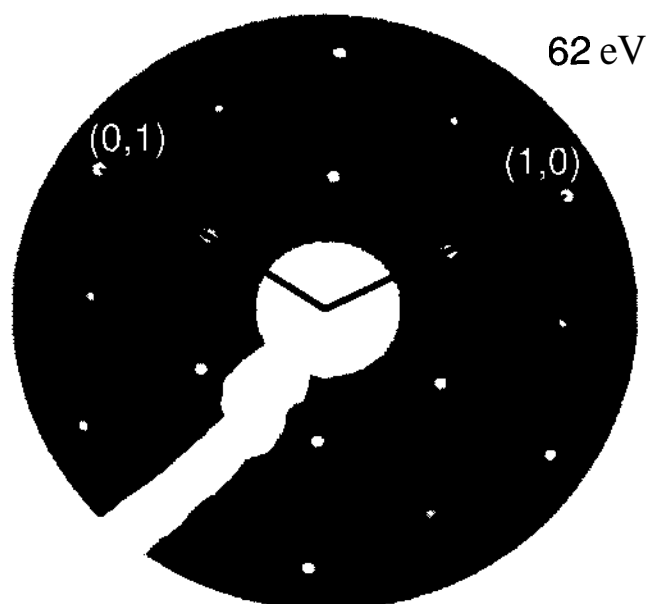


Figure 5.2.2: LEED pattern of the  $p(2 \times 2)$ -0 superstructure on Pd(111) at 62 eV electron energy.

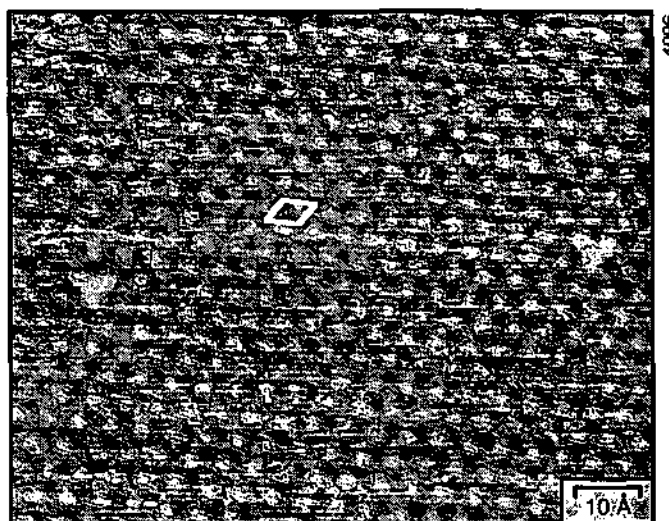


Figure 5.2.3: STM image of the  $p(2 \times 2)$ -O superstructure on Pd(111) ( $100 \times 80 \text{ \AA}^2$ ,  $-26 \text{ mV}$ ,  $0.46 \text{ nA}$ ). The corresponding unit cell is highlighted in the image.

$10^{-6}$  Torr s) at an oxygen partial pressure of  $3 \times 10^{-8}$  mbar the saturation coverage of 0.25 ML is reached. Accordingly, the relative Auger peak-to-peak height (APPH) corresponding to this coverage, which was measured to be 2.2 % (of the main Pd peak at 330 eV, taking the O peak at 515 eV as reference), stayed constant during any additional exposure (Fig. 5.2.1). The LEED pattern of such an oxygen saturated Pd(111) surface always shows very sharply pronounced  $(2 \times 2)$  superstructure spots as indicated in Fig. 5.2.2 and no change in the spot intensities was observed during several hours. Consequently, this  $(2 \times 2)$ -O superstructure was sufficiently stable for an accurate, quantitative LEED analysis. After 16 hours, however, no superstructure was visible in the LEED images anymore, which showed a simple  $(1 \times 1)$  pattern.

A room-temperature STM image of a Pd(111) surface with similar oxygen coverage (2% APPH) is presented in Fig. 5.2.3, also showing a clearly visible  $(2 \times 2)$  superstructure. The fuzziness of this image is caused by the high mobility of the chemisorbed oxygen atoms, but it is not totally clear whether oxygen is mapped as protrusion or depression. Since oxygen is most of the time imaged as depression (see e.g. Ref. [63]), the unit cell highlighted in Fig. 5.2.3 connects adjacent dark spots.

### 5.2.2 Surface structure

Although it is well known that the exposure of Pd(111) crystals to  $\text{O}_2$  at room temperature leads to the formation of a  $(2 \times 2)$  LEED pattern, most likely caused by oxygen adsorption in 3-fold hollow sites [56, 57, 64], there is no general agreement concerning

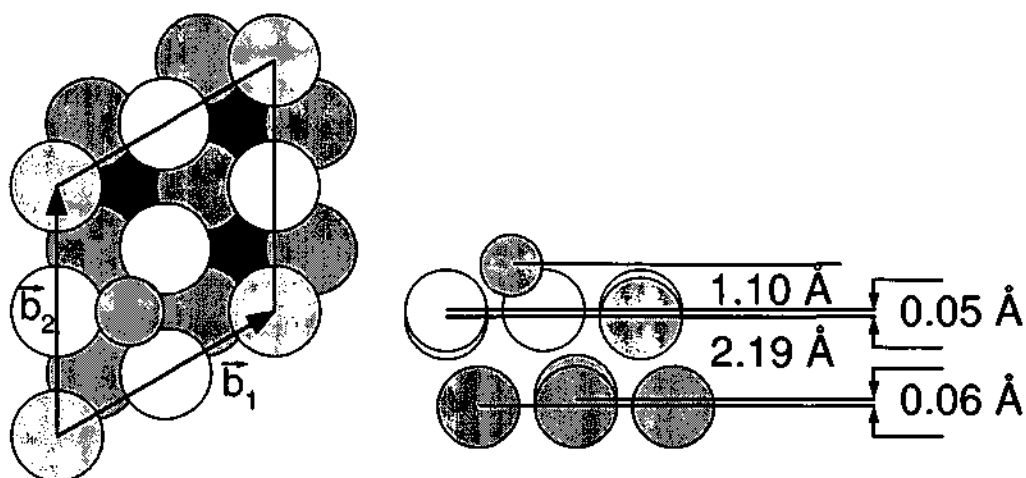


Figure 5.2.4: Best-fit structure for the Pd(111)-(2x2)-O surface as determined by LEED.

the exact adsorption site; i.e. whether it is an hcp- or fcc-like site. While a study using low-energy ion scattering (LEIS) favors adsorption in hcp sites [56], a more recent analysis, involving quantitative LEED and DFT calculations, found the fcc sites to be occupied by oxygen. The later result, however, seems to be more probable, since oxygen atoms are known to tend to adsorb in those sites, where metal atoms of the next layer would sit [65]. Hence, in order to resolve all doubt concerning the true adsorption site of oxygen on Pd(111) and to determine the structural details of this system, another quantitative LEED analysis was performed.

For this analysis of the p(2 x 2)-O superstructure, LEED patterns starting from 30 eV up to 360 eV were recorded, enabling the extraction of 5 integer and 7 fractional order, symmetry-inequivalent beam-sets. The cumulative energy range obtained by these 12 beam-sets amounted to 2720 eV. Due to reasons mentioned above, just two models were investigated, namely the ones with oxygen atoms being located either in hcp or fcc 3-fold hollow sites. For optimization, the first 3 Pd interlayer distances as well as the height of the oxygen atom above the surface were varied. Additionally, buckling of the first three substrate layers was considered. Finally, the vibrational amplitudes of the oxygen atom and the first two Pd layers were optimized within the tensor-LEED framework. The imaginary part of the inner potential  $V_{0i}$  and the vibrational amplitudes of the bulk, however, had to be analyzed full dynamically after the geometrical best-fit structure was found. Last but not least, the oxygen coverage was checked using the average  $t$ -matrix approximation (cf. Sec. 2.8.1.3).

The result of this quantitative LEED analysis is clearly in favor of oxygen adsorption in 3-fold hollow fcc sites, yielding  $R_{Pe} = 0.19$ , since the hcp-model shows quite a bad agreement with the experimental data ( $R_{Pe} = 0.52$ ). The best-fit structure obtained

	LEED	LEED [57]	DFT[57]
$d_{OPd}$ (Å)	$1.10 \pm 0.03$	$1.17 \pm 0.03$	1.16
$b_1$ (Å)	$0.05 \pm 0.03$	$0.07 \pm 0.03$	0.07
$\Delta d_{12}$ (%)	$+1.0 \pm 1.1$	+0.7	+3.4
$b_2$ (Å)	$0.06 \pm 0.03$	$0.08 \pm 0.05$	0.00
$\Delta d_{23}$ (%)	$+0.1 \pm 1.2$	-	-
MA	$0.01 \pm 0.03$	-	-
$\Delta d_{34}$ (%)	$-0.3 \pm 1.6$	-	-
$d_{bulk}$ (Å)	2.246	2.25	-

Table 5.2.1: Comparison of the structural parameters obtained in this work for an oxygen saturated Pd(111) surface with the corresponding values given in literature, where  $d_{xy}$  stands for the averaged interlayer distance between Pd layer  $x$  and  $y$  and  $b_z$  represents the buckling of the according layer  $z$ .

by the analysis is depicted in Fig. 5.2.4 and compared to LEED and DFT results of Seitsonen *et al.* [57] in Table 5.2.1. The error bars given in Table 5.2.1 were derived from Pendry's variance ( $R_{Pe}(var) = 0.022$ ), namely by varying a certain parameter away from the best fit structure until the difference between the according  $R$ -factor and the best fit value got larger than this variance. Since all other parameters were fixed to the values of the best fit structure, the obtained errors were slightly too small. Consequently, the larger error was assumed for every parameter, according to Fig. 5.2.6. It is obvious, that the agreement between the two LEED results is nearly perfect, whereas the DFT values show some minor differences. The general trend, however, is the same: Palladium atoms that are in direct contact with oxygen atoms relax outward, leading to a slight averaged expansion of the first Pd interlayer spacing with respect to the bulk structure. This effect can be easily understood if one considers the weakening of the bonds of the corresponding Pd atoms induced by the presence of the strongly electronegative oxygen. The bond length between oxygen and palladium was found to be  $1.93 \text{ \AA}$ , which is also quite similar to the value obtained by Seitsonen *et al.* [57] ( $1.97 \text{ \AA}$ ). Unfortunately it is not possible to compare the two LEED results in more detail due to the restricted information given in Ref. [57].

The optimization of the vibrational amplitudes resulted in  $0.18 \text{ \AA}$  for the oxygen atoms,  $0.17 \text{ \AA}$  for the Pd atoms bond to the oxygen and  $0.16 \text{ \AA}$  for the lower Pd atom in the first layer. For the second Pd layer the deviation from the bulk vibrational amplitude ( $0.127 \text{ \AA}$ ) was found to be already negligible. The best-fit values of the inner potential were  $V_{0r} = 5.5 \text{ eV}$  and  $V_{0i} = 4.5 \text{ eV}$ , respectively. Finally, the variation of the oxygen coverage yielded an occupancy of the 3-fold hollow fcc sites with oxygen of 100%,

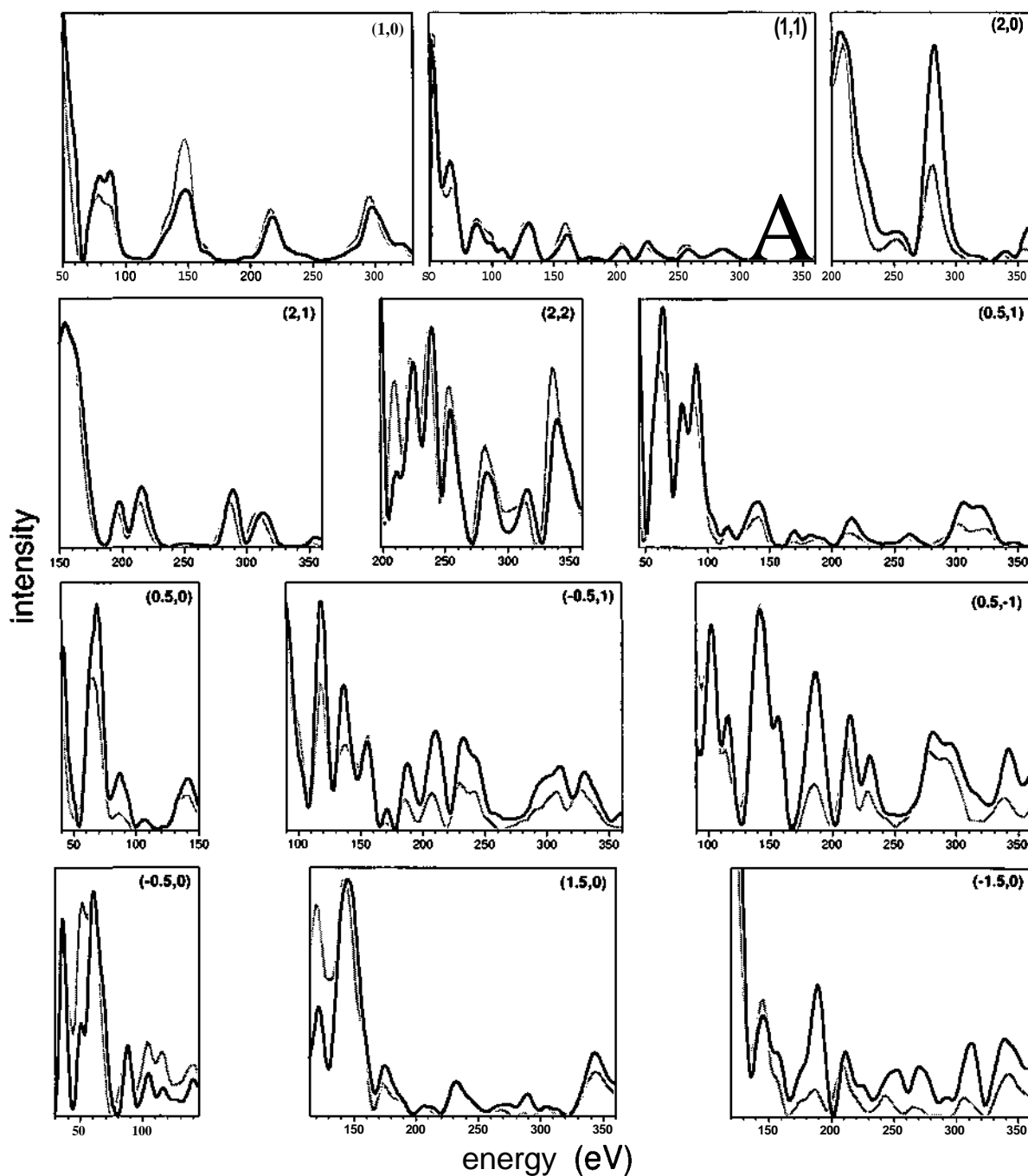


Figure 5.2.5: Comparison between experimental (black) and calculated (gray) LEED I-V spectra of the best-fit model found for the  $p(2 \times 2)$ -O overlayer on Pd(111). The total energy range amounted to 2720 eV and yielded a Pendry R-factor of 0.19.

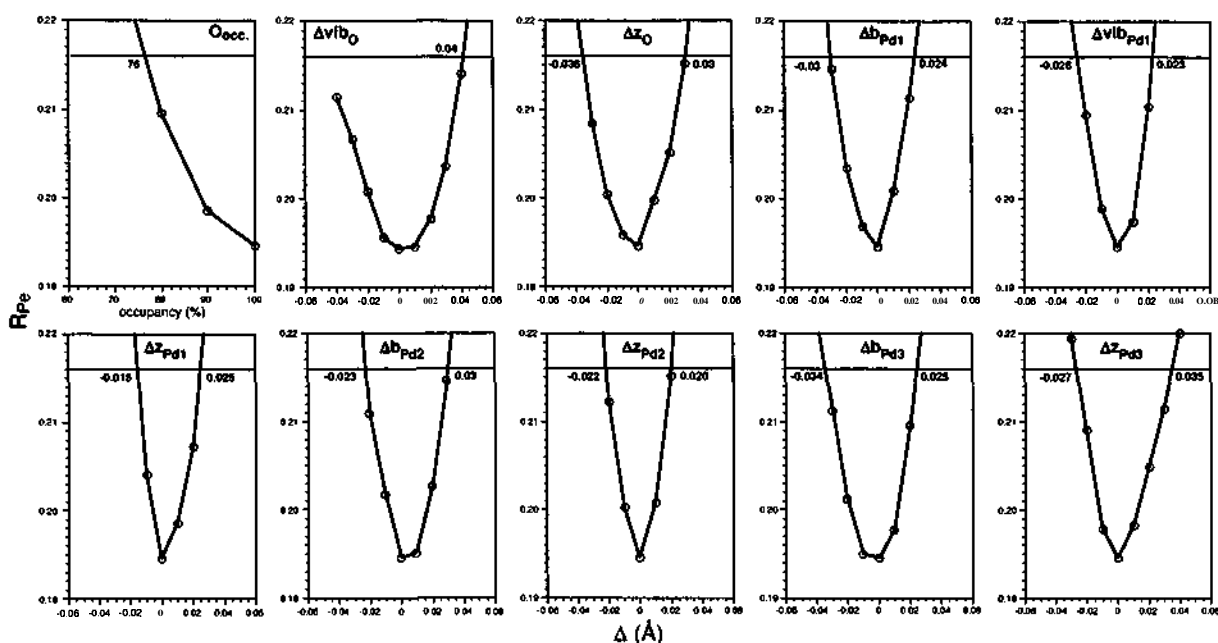


Figure 5.2.6: Error determination for all optimized parameters of the LEED analysis of the  $p(2 \times 2)$ -O overlayer on Pd(111). All deviations from the best fit structure that correspond to an  $R$ -factor below  $R_{Pe}(\min) + R_{Pe}(\text{var})$  (cf. black lines) are in principle compatible with the presented LEED result.

indicating either that no oxygen desorbs at all during the measurement or that at least the balance between oxygen desorption and adsorption from the residual gas phase was even. Consequently, the measured APPHs indeed correspond to an O-coverage of 0.25 ML. The good agreement of all calculated  $I$ - $V$  spectra with the experimental ones can be seen in Fig. 5.2.5.

The results obtained for this particular reconstruction can be summarized as follows: At room temperature oxygen adsorption on Pd(111) leads to the formation of a  $p(2 \times 2)$ -O superstructure, which is caused by chemisorbed oxygen sitting in 3-fold hollow *fcc* sites. The oxygen saturation coverage at room temperature is exactly 0.25 ML (as long as only molecular oxygen is dosed). The later result was important for the calibration of the oxygen Auger signal, which was necessary to enable a determination of the oxygen coverage of the surface oxide. Equipped with the findings described above, the far more complicated structure of the surface oxide was treated.

## 5.3 A surface oxide

### 5.3.1 Preparation

The cleaning procedures prior to the actual surface oxide preparation were a little bit more sophisticated than in the previous case. The crystals were cleaned by the usual sputtering-annealing cycles, but additionally exposed to oxygen, while keeping the samples at 600 °C in an oxygen pressure of  $2 \times 10^{-8}$  mbar, followed by flashes to 1100 °C. The surface oxide was then formed by exposing a Pd(111) surface to 5000 L of molecular oxygen at a temperature of 320 °C and an oxygen pressure of at least  $5 \times 10^{-6}$  mbar. This high oxygen partial pressure was achieved by either positioning the sample directly in front of an O<sub>2</sub> outlet (*oxygen shower*), which led to local pressures at the sample about 1000 times the background pressure, or by simply flooding the chamber with oxygen until the desired pressure was reached. The former preparation, which allowed for considerably higher pressures than the latter one, however, was only possible in the preparation chamber of the STM. Fig. 5.3.1 shows the formation of this new structure as a function of the exposure time, indicating  $\approx 3600$  L to be the critical dose needed to reach saturation coverage. In order to preserve the obtained structure while cooling down to room temperature, the vacuum quality had to be quite high, especially with regard to the H<sub>2</sub> and CO partial pressures ( $< 5 \times 10^{-11}$  mbar), since in setups, where this condition was not fulfilled, a complete reduction of the surface oxide, similar to the one reported in Ref. [58], was observed. Therefore, in the setup used for SXRD measurements, the sample had to be cooled down in oxygen atmosphere to  $\approx 180$  °C in order to keep the surface oxide stable.

A Pd(111) crystal prepared following the procedures described above shows a very sharp, but at the same time very complex LEED pattern, indicating a very well ordered superstructure (cf. Fig 5.3.2). Also STM images of this surface reveal a very interesting and beautiful structure, resembling a Persian-carpet-like pattern (Fig 5.3.3). In the work of Zheng and Altman [52], however, nitrogen dioxide (NO<sub>2</sub>) was used as oxidant instead of O<sub>2</sub>, but, despite the differences in preparation, a comparison of the LEED patterns and STM images obtained in their study with the ones found in the present work shows that both preparations yield an identically ordered structure. Analyzing an Auger spectrum of this structure, one finds a relative oxygen APPH of  $\sim 6.5\%$ , indicating a rather high oxygen coverage of about 0.74 ML.

### 5.3.2 Qualitative LEED

Taking a closer look at the LEED pattern of this complex structure one can identify the coexistence of three domains of a square superstructure on the hexagonal Pd(111)

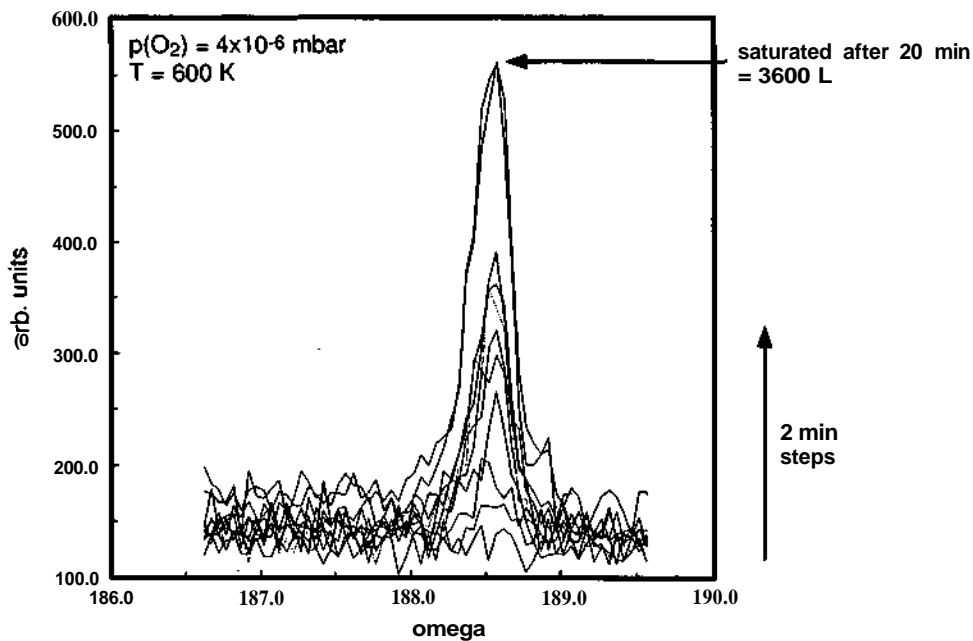


Figure 5.3.1: Development of a superstructure reflection of the surface oxide in dependence of the exposure time.

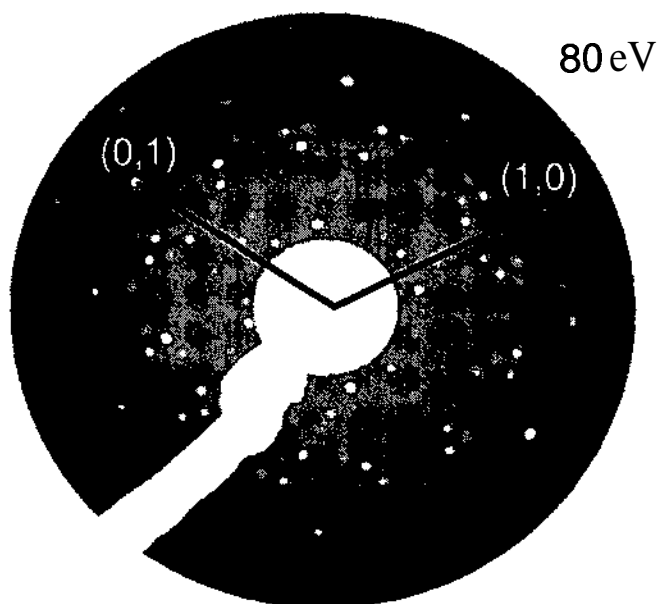


Figure 5.3.2: LEED pattern of a surface oxide on Pd(111) recorded at an electron energy of 80 eV.

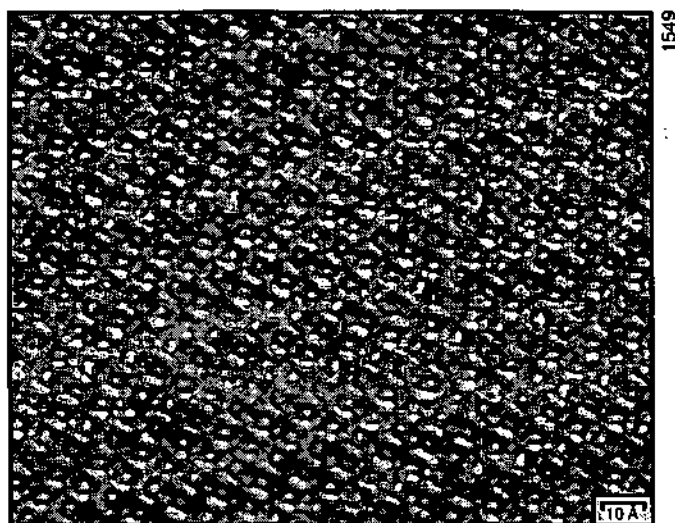


Figure 5.3.3: STM image of the surface oxide ( $150 \times 100 \text{ \AA}^2$ ,  $0.5 \text{ mV}$ ,  $0.46 \text{ nA}$ ).

substrate (cf. Fig 5.3.4). An outstanding feature of these domains is the fact that one of the two diagonals of such a square reciprocal superstructure unit cell is perfectly aligned with a reciprocal lattice vector of the substrate, i.e. one diagonal of a superstructure unit cell in reciprocal space matches exactly one half of  $\vec{G}(1,0)$ . Knowing the next neighbor distance of Pd(111) to be  $2.75 \text{ \AA}$ , it is therefore quite easy to calculate the corresponding side length of such a superstructure unit cell in real space. The only thing that is important here is that one must not forget to take the different angles between the lattice vectors of the hexagonal substrate and the lattice vectors of the square superstructure into account. Using Eq. (2.3.2) results in the following relations for the absolute values of substrate and superstructure lattice vectors:

$$a^* = \frac{2\pi}{a \cdot \cos 30^\circ} = \frac{4\pi}{a \cdot \sqrt{3}}, \quad b^* = \frac{2\pi}{b} \quad (5.3.1)$$

which results with  $\sqrt{2} \cdot b^* = \frac{1}{2} \cdot a^*$  in

$$b = \sqrt{6} \cdot a \sim 6.74 \text{ \AA} \quad (5.3.2)$$

For simplicity the superstructure will therefore be called  $(\sqrt{6} \times \sqrt{6})$  structure in the following, despite of the fact that it is a square structure on a hexagonal substrate lattice. Another result obtained by this qualitative LEED analysis is the fact that one diagonal of the superstructure has to be aligned commensurate with regard to the substrate, while the other diagonal is incommensurate. The additional spots visible in Fig. 5.3.4, however, are exclusively caused by multiple scattering events between the

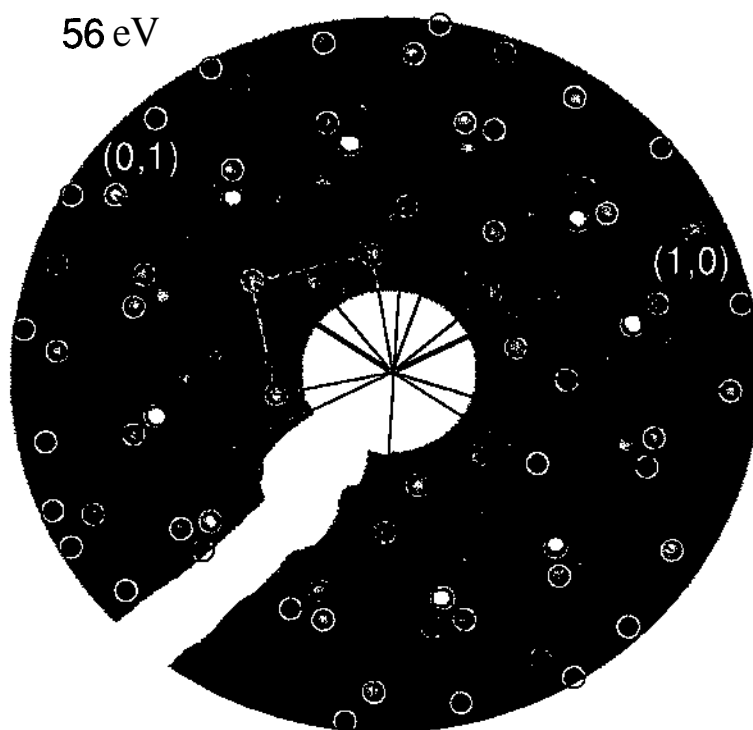


Figure 5.3.4: Three domains of a square superstructure indicated in the LEED pattern of the surface oxide.

hexagonal substrate and the square superstructure and not by some additional ordered phase.

### 5.3.3 STM

Fig. 5.3.5 shows a high resolution STM image of the surface oxide, where indeed the  $(\sqrt{6} \times \sqrt{6})$  unit cell can be identified. This image is particularly nice, since it exhibits in the lower left corner a rather small area where the underlying substrate is visible. By utilizing the presence of this Pd(111)-(1 x 1) area as a ruler, it is possible to determine that one diagonal of the square is equal to the  $[2\bar{1}\bar{1}]$  substrate vector and hence commensurate, while the other diagonal - parallel to the  $[0\bar{1}1]$  direction - is incommensurate, in agreement with the qualitative LEED result and Ref. [52]. It is this incommensurability, which is responsible for the waviness of the corrugation in the direction normal to  $[2\bar{1}\bar{1}]$ , since it causes a different registry for every superstructure unit cell along this direction. Consequently, the exact supercell looks somewhat larger (cf. red supercell indicated in Fig. 5.3.5, which was used for DFT calculations later on), although the in-plane periodicity is strictly  $(\sqrt{6} \times \sqrt{6})$ .

As indicated in Sec. 5.3.1, the surface oxide was found to be not very stable, since

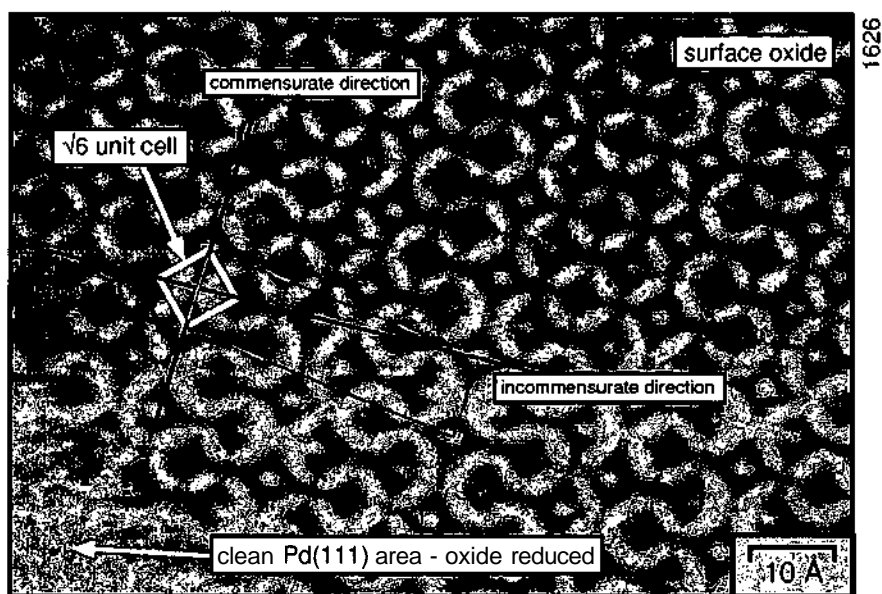


Figure 5.3.5: High resolution STM image of the surface oxide ( $100 \times 80 \text{ \AA}^2$ ,  $-0.5 \text{ mV}$ ,  $3.5 \text{ nA}$ ). In the lower left corner the oxide is partly reduced revealing the  $(1 \times 1)$  periodicity of the underlying substrate, enabling the determination of the commensurate and incommensurate directions of the superstructure.

it could be easily reduced by either annealing the sample at elevated temperatures ( $> 350^\circ\text{C}$ ) or by dosing CO at room temperature followed by a flash to  $150^\circ\text{C}$ . The reduction process was found to start at the step-edges, revealing reduced areas, where large holes of monoatomic depth could be identified (Fig. 5.3.6). By increasing the CO dose or the annealing time the surface oxide could be completely removed resulting in a full surface coverage of this reduced surface structure (Fig. 5.3.7), which could be identified as consisting of unreconstructed Pd(111) areas partly covered by a  $(2 \times 2)$  oxygen overlayer - the surface fraction of this residual, chemisorbed overlayer depends strongly on the applied annealing temperatures. This rather simple reduction experiment gave already a lot of clues about the surface oxide itself and the physical processes involved.

The gradual decrease of the area covered by the surface oxide starting at the step edges and continuing at the borders to the  $(2 \times 2)$  structure could be explained by the desorption model proposed by B. Klötzer *et al.* [66]. Within this model direct desorption from the surface oxide is assumed to be much slower than from the chemisorbed  $(2 \times 2)$  overlayer. Therefore, desorption preferentially takes place from the  $(2 \times 2)$  phase with the surface oxide acting as a feedstock for oxygen. This view is also supported by various STM images taken during the desorption process, showing a coexistence of the  $p(2 \times 2)\text{-O}$  phase and the surface oxide as well as an increase of the former surface

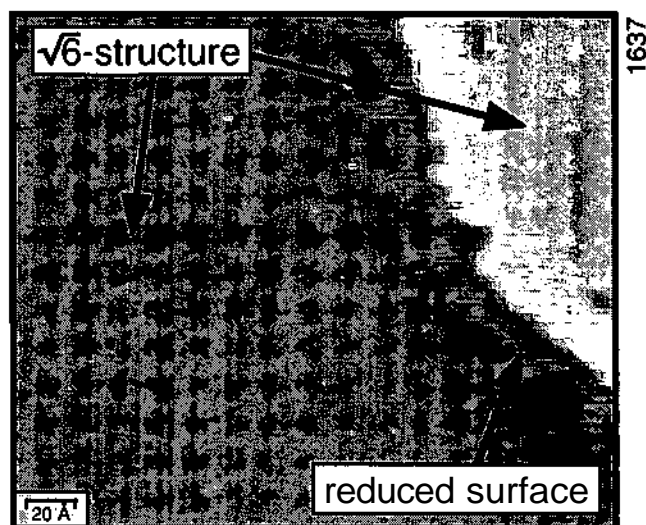


Figure 5.3.6: STM image ( $250 \times 215 \text{ \AA}^2$ ,  $-1 \text{ V}$ ,  $0.46 \text{ nA}$ ) of the partly reduced surface oxide (5 L CO followed by a flash to  $150^\circ\text{C}$ ). The reduction starts at the step edge and results in Pd(111) areas covered by the low coverage (1 x 2) oxygen overlayer, wherein large hexagonal holes can be identified.

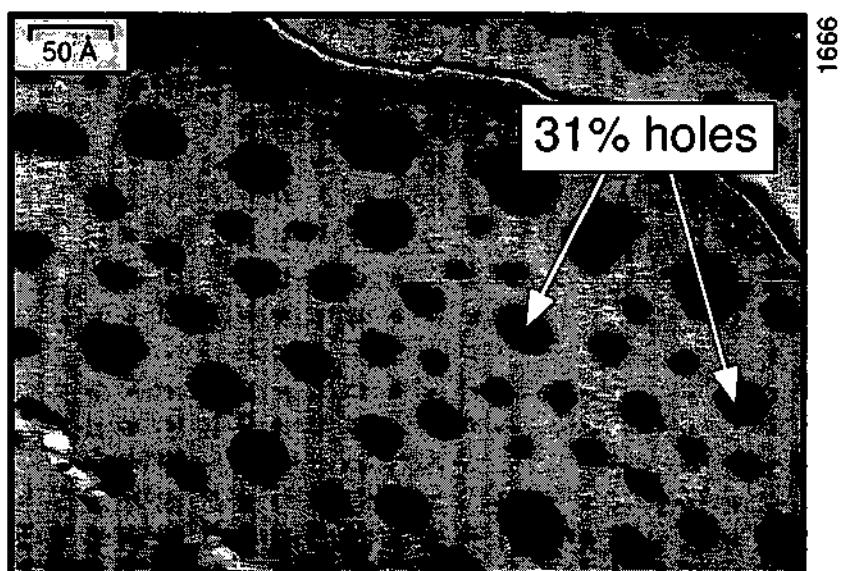


Figure 5.3.7: STM image ( $500 \times 355 \text{ \AA}^2$ ,  $-1 \text{ V}$ ,  $0.66 \text{ nA}$ ) of the completely reduced surface (25 L CO followed by a flash to  $150^\circ\text{C}$ ) showing a lot of large hexagonal holes of monoatomic depth. The surface fraction covered by those holes was determined to be 31%.

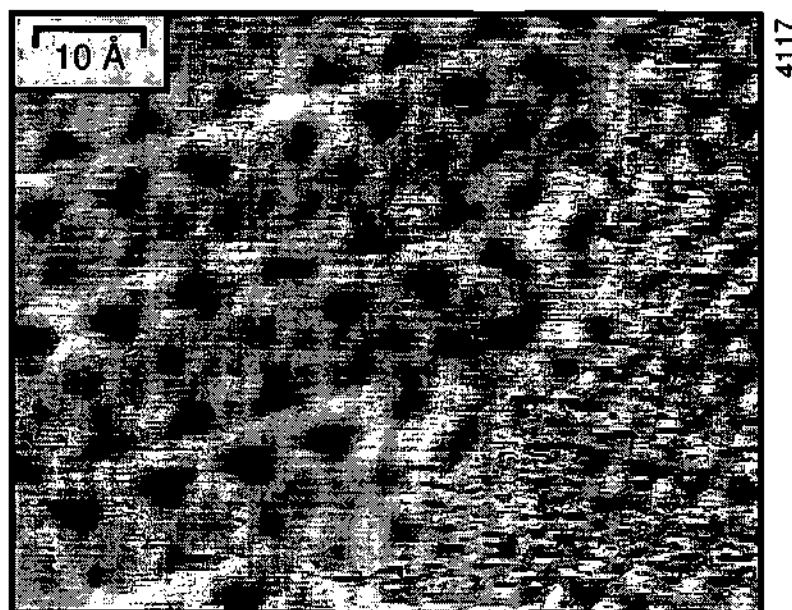


Figure 5.3.8: STM image ( $70 \times 56 \text{ \AA}^2$ ,  $-1 \text{ V}$ ,  $0.66 \text{ nA}$ ) showing the phase boundary between the surface oxide and the chemisorbed  $p(2 \times 2)\text{-O}$  phase on a single terrace - taken after the exposure of clean Pd(111) to  $750 \text{ L O}_2$  at  $300^\circ\text{C}$ .

fraction at the expense of the latter one (Fig. 5.3.8).

Consequently, the defective surface areas, which display those holes of monoatomic depth, must have been formed by Pd atoms of the decomposed surface oxide, which therefore has to show a reduced Pd density. Keeping that in mind, it is clear why the formation of this surface oxide is an activated process, i.e. why it requires an elevated substrate temperature during exposure to oxygen: An extensive mass transport of Pd atoms over mesoscopic distances is necessary, which is only possible if the substrate temperature is high enough. The oxygen atoms have to be able to replace Pd atoms in the surface layer, which then start to diffuse around until they eventually form islands and peninsulas together with oxygen. Evaluating the surface fraction of those holes found on a completely reduced surface therefore allows for an estimation of the number of Pd atoms in the  $(\sqrt{6} \times \sqrt{6})$  unit cell of the surface oxide. Since about 31% of the reduced surface is covered with holes as indicated in Fig. 5.3.7, the Pd density in the surface oxide has to be only about 69% of the one of a regular Pd(111) monolayer ( $1.526 \times 10^{19} \text{ atoms/m}^2$ ), which results, by multiplying with the area of a  $(\sqrt{6} \times \sqrt{6})$  cell, in:

$$N_{Pd} = 0.69 \cdot 1.526 \times 10^{19} \cdot (\sqrt{6} \cdot 2.75 \times 10^{-10})^2 = 4.8 \quad (5.3.3)$$

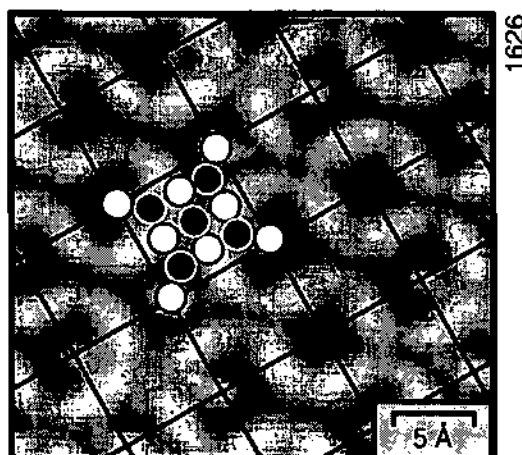


Figure 5.3.9: Magnification of an STM image of the surface oxide ( $30 \times 28 \text{ \AA}^2$ ,  $-0.5 \text{ mV}$ ,  $3.5 \text{ nA}$ ), showing several  $(\sqrt{6} \times \sqrt{6})$  cells. A possible model for the in-plane configuration of the structure is drawn in the center of the image, exhibiting the experimentally suggested composition of 5 Pd and 5 O atoms (white spheres: palladium, black spheres: oxygen)

In other words, approximately 5 Pd atoms have to be located within one  $(\sqrt{6} \times \sqrt{6})$  superstructure unit cell. To estimate the oxygen content of such a  $\sqrt{6}$ -cell, the relative oxygen APPHs of the surface oxide and the  $p(2 \times 2)$ -O phase have to be compared. As indicated in Sec. 5.3.1 the analysis of the Auger spectra resulted in an oxygen coverage of about 0.7 ML and therefore  $\sim 5$  oxygen atoms per  $\sqrt{6}$ -cell. Including the highest and the lowest possible values compatible with some of the experimental results, led to 4-6 oxygen atoms per superstructure unit cell. Especially lower oxygen densities have to be considered, since the calibration strongly depends on the preparation of a perfect  $p(2 \times 2)$ -O phase covering the whole surface, which might not have been the case - an insight gained after analyzing the results described in the next paragraphs. Anyway, the number of possible model structures is already considerably reduced due to the experimental findings. Taking a closer look at a high-resolution STM image of the surface oxide, one can therefore try to build up a model structure compatible with the previous results. Since one  $\sqrt{6}$ -cell contains 5 Pd atoms, it is very tempting and straightforward to relate them to the bright spots observed in the STM images as depicted in Fig. 5.3.9. Even that can't be verified by experiment easily and the exact identification of the location of the oxygen atoms is considerably harder - if not impossible. However, one structure model is indicated in Fig. 5.3.9 that shows the  $\text{Pd}_5\text{O}_5$  stoichiometry favored so far. Nevertheless, the next step in this analysis had to be a DFT calculation in order to gain information on the stability of the possible trial models and maybe already the right structural result.

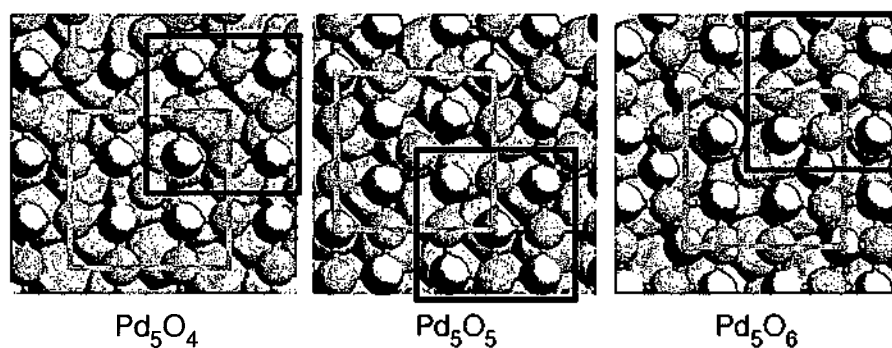


Figure 5.3.10: Simulated annealing results for three different stoichiometries.  $\text{Pd}_5\text{O}_4$  model yields the highest adsorption energy of 1.0 eV per oxygen atom, while the adsorption energy for each additional oxygen atom is smaller than 0.3 eV, implying that the  $\text{Pd}_5\text{O}_5$  and  $\text{Pd}_5\text{O}_6$  structures are unstable towards oxygen removal under realistic conditions. Grey squares represent the calculated supercells, black squares the corresponding experimental ones.

#### 5.3.4 Structural model - DFT

The DFT calculations presented in the following were performed using the Vienna *Ab initio* Simulation Package (VASP) [67, 68]. The interaction between the electrons and ions was described by the projector augmented wave method (PAW) in the implementation of Kresse and Joubert [69]. All DFT results were obtained by utilizing the generalized gradient approximations of Perdew and Wang (PW91) [70].

In order to gain information on the correct model and its precise atomic structure, the configuration space was probed by first-principles simulated annealing based on molecular dynamic calculations. In a first step, three ( $\sqrt{6} \times \sqrt{6}$ ) cells with different stoichiometry ( $\text{Pd}_5\text{O}_4$ ,  $\text{Pd}_5\text{O}_5$  and  $\text{Pd}_5\text{O}_6$  - see Fig. 5.3.10) were simulated on a two layer thick frozen Pd(111) substrate. Since such a superstructure cell is commensurate in the direction of only one diagonal, the substrate was compressed in the  $[0\bar{1}1]$  direction by a factor 8/6.92 to reach commensurability. Those model structures were then melted at 3000 K, cooled down to 1000 K in 20 ps and finally quenched into the nearest local energy minimum. Out of the three simulated compositions, only the  $\text{Pd}_5\text{O}_4$  structure showed a larger oxygen adsorption energy (1.0 eV) than bulk PdO (0.98 eV). For the models with higher oxygen coverages the adsorption energies found for the additional oxygen atoms were very small ( $< 300$  meV), which strongly suggested the  $\text{Pd}_5\text{O}_4$  model to be the correct one.

For the final calculation a large supercell, consisting of seven  $\sqrt{6}$ -cells (i.e. 48 Pd atoms per layer), was used as shown in Fig. 5.3.11. For this supercell, the mismatch between adsorbate and substrate is only 1% in the direction of the second diagonal. This can

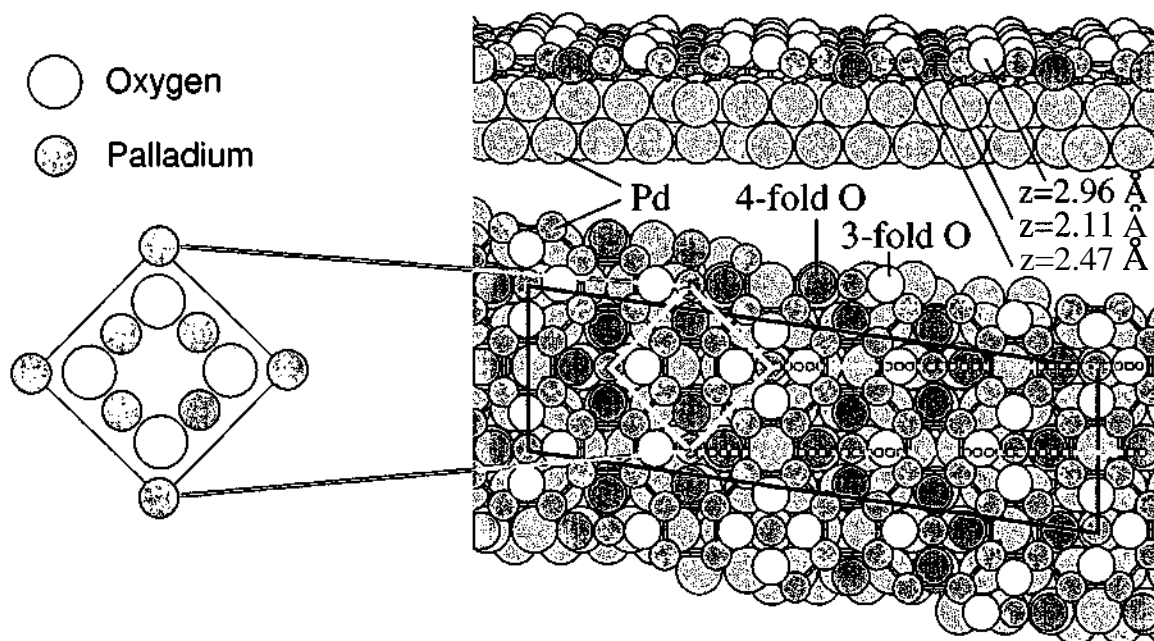


Figure 5.3.11: Final atomic structure of the surface oxide as determined by DFT using large supercells consisting of  $7\sqrt{6}$ -cell on a 3 layer thick Pd(111) slab. The surface oxide was compressed by 1% to reach commensurability. The right hand side shows a magnification of the averaged  $(\sqrt{6} \times \sqrt{6})$  unit cell, which was found to consist of 5 palladium and 4 oxygen atoms, forming two squares within the cell, rotated by  $45^\circ$  with respect to each other.

be seen clearly in Fig. 5.3.11, since 3.5 times the diagonal of a  $\sqrt{6}$ -cell was forced to match 12 Pd-Pd distances in the substrate layer ( $3.5 \cdot \sqrt{2} \cdot \sqrt{6} : 12$ ). Looking at the optimal final positions (Fig. 5.3.11), one quickly realizes that the averaged in-plane structure found by DFT is indeed very similar to the structural model proposed in Fig. 5.3.9, the only obvious difference being the missing oxygen atom in the middle of the  $\sqrt{6}$ -cell compared to the former model. Since DFT strongly suggests a  $\text{Pd}_5\text{O}_4$  stoichiometry, it is up to additional experimental methods to confirm this finding. What also can be seen in Fig. 5.3.11, however, is the existence of two different types of Pd atoms in the surface: One Pd atom per unit cell has four oxygen neighbors, whereas the other four Pd atoms are only adjacent to two oxygen atoms. Another difference found between those two types of Pd atoms is that the fourfold coordinated ones are located directly above the densely packed Pd atom rows, while the others are positioned somewhere in between, close to bridge or hollow sites. Moreover, half of the oxygen atoms are bonded only to in-plane Pd neighbors (3-fold O) and the other half is additionally coordinated to subsurface Pd atoms directly below (4-fold O). This different coordination is found to result in a considerably strong buckling of the oxygen atoms ( $\approx 0.85 \text{ \AA}$ ). This structure, however, has neither the stoichiometry nor structural similarity to any plane of the bulk oxide PdO. The oxygen adsorption energy of the final structure was calculated to be 1.24 eV, which lies between the O-adsorption energy of the  $p(2 \times 2)$ -O overlayer (1.36 eV) and bulk PdO (0.98 eV). Consequently, the  $\text{Pd}_5\text{O}_4$  structure found by DFT is thermodynamically stable at intermediate oxygen pressures and can indeed represent the correct atomic structure of the surface oxide discussed above.

### 5.3.5 SXR D analysis

For the SXR D analysis of this structure a rather large data set was evaluated, consisting of 630 in-plane reflections and 7 rod scans. Data reduction and structural analysis were performed using the ANA-ROD package written by Vlieg [71, 72]. The (HKL) intensities were measured by scanning the sample azimuth (i.e. the polar angle for the specular rod). The data were integrated after background subtraction, and the structure factors were then calculated by applying the Lorentz correction and the correction factors for beam polarization and the illuminated area of the sample [48]. During the analysis of the recorded data, a slight distortion of the ( $\sqrt{6} \times \sqrt{6}$ )-cell was detected, since the angle between (H,0) and (0,H) reflections was found to be not exactly  $90^\circ$ . It was possible to deduce from the deviations of the sample azimuths that the according angle in reciprocal space has to be  $90.4^\circ \pm 0.1^\circ$ , which results in  $89.6^\circ$  for the real space angle. Consequently, the superstructure lattice vectors are slightly shorter than the ones for a perfect square ( $6.72 \pm 0.01 \text{ \AA} : 6.74 \text{ \AA}$ ), in other words the surface oxide layer has to be compressed by about 1% in the incommensurate

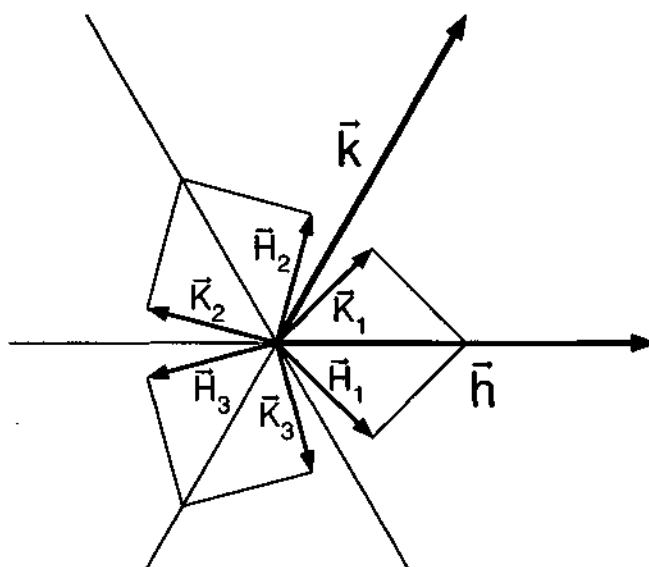


Figure 5.3.12: Relationship between superstructure unit cells and substrate unit cell in reciprocal space.

direction with regard to a perfect square  $\sqrt{6}$  structure. This finding, however, fits very well to the DFT results presented above and indicates that the large cell treated in the theoretical analysis may indeed represent the surface oxide encountered in reality. Since this deviation becomes critical for high values of H and K only, the in-plane data set (measured at  $l = 0.5$ , in order to obtain the best possible signal to background ratio) was restricted to 14 nonequivalent superstructure reflections ( $H, K \leq 4$ ). Those variables H and K mentioned before refer to the reciprocal superstructure lattice vectors  $\vec{H}$  and  $\vec{K}$ , which are related to the reciprocal substrate lattice vectors  $\vec{h}$ ,  $\vec{k}$  as follows (for the first domain):

$$H \cdot \vec{H}_1 + K \cdot \vec{K}_1 = (0.3943H + 0.1057K) \cdot \vec{h} + (-0.2887H + 0.2887K) \cdot \vec{k} \quad (5.3.4)$$

- relations for the other two domains are very similar (cf. Fig. 5.3.12).

The form factors in the final data set were obtained by averaging over all three domains and then used as experimental input for the analysis. Due to the incommensurability of the surface oxide, the SXRD analysis was restricted to the oxide layer at first, neglecting scattering from the substrate. Consequently, as a starting structure a planar layer composed of  $\sqrt{6}$ -cells, similar to the averaged one depicted in the right hand side of Fig. 5.3.11, was designed. Assuming this model, which allows only for two free parameters (in-plane coordinates compatible with  $p4mm$  symmetry), an analysis based on the above mentioned data set yields an excellent agreement between measured

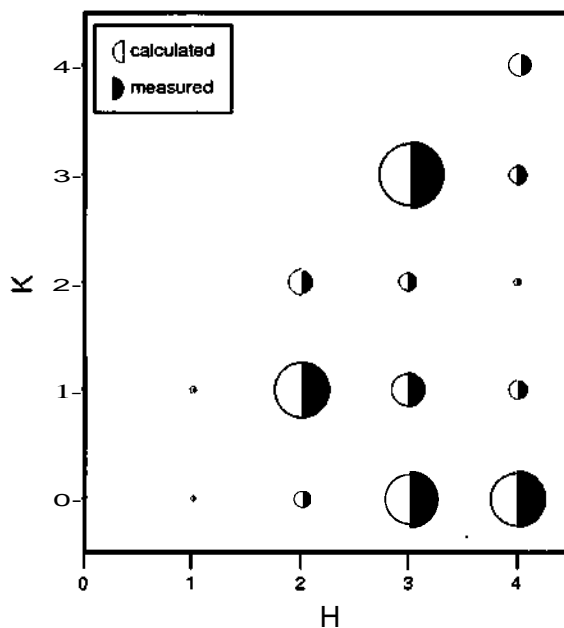


Figure 5.3.13: Comparison between calculated and measured structure factors of 14 nonequivalent superstructure reflections of the surface oxide.

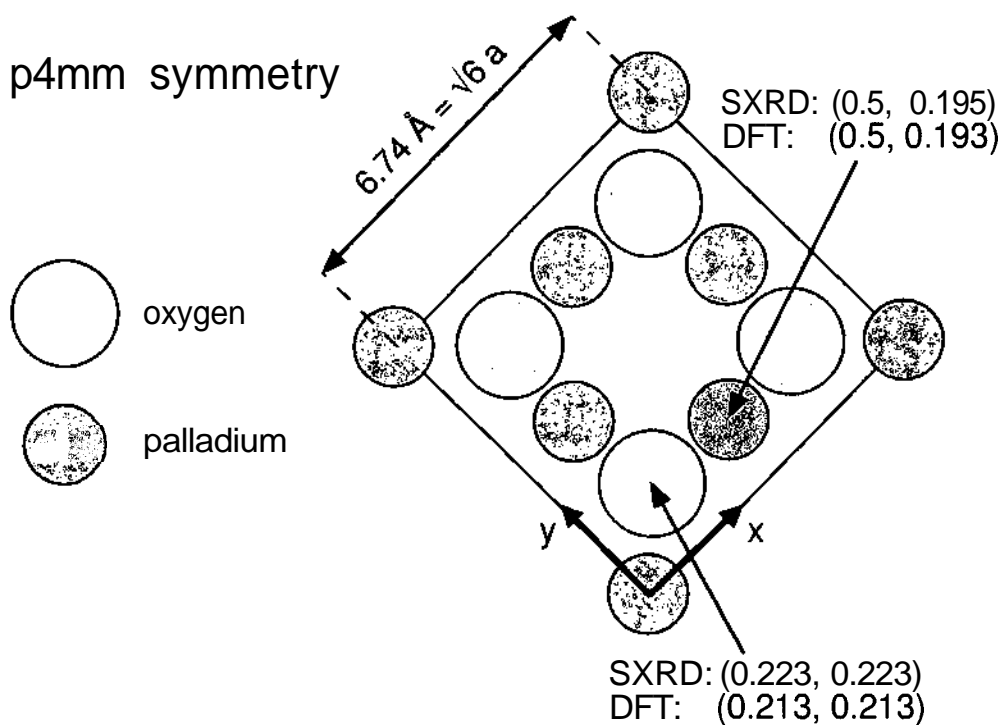


Figure 5.3.14: Comparison between SXRD and DFT results for the in plane structure of the surface oxide.

and calculated structure factors ( $\chi^2 = 0.48$  - cf. Fig. 5.3.13). The resulting in-plane coordinates match the *ab initio* values, which were averaged over seven  $\sqrt{6}$ -cells in order to be directly comparable to the SXRD results, within 0.02 Å for Pd and 0.1 Å for O (see Fig. 5.3.14). However, due to the high quality of the data, the SXRD analysis is also quite sensitive to the oxygen atoms. Adding an O atom in the center of the cell - as suggested by the combined STM and AES results (cf. Fig. 5.3.9) - yields a considerably worse agreement reflected in  $\chi^2 = 4.1$ . Consequently, this Pd<sub>5</sub>O<sub>5</sub> model is not compatible with the SXRD measurements and therefore ruled out as a possible surface structure.

In order to obtain some information on the out-of-plane structure of this surface oxide, two superstructure rods of the first domain were analyzed. Due to the fact that SXRD is not very sensitive to oxygen and in particular not to its vertical displacements, the DFT results were used to create a starting model. The difference of this new 3-dimensional superstructure unit cell compared to the previous one was that it consisted of 8 oxygen atoms - one half 0.4 Å below and the other half 0.4 Å above the Pd atoms. The occupancy of this oxygen positions was assumed to be 50%. This approach was necessary to account for the random distribution of the 3-fold and 4-fold bound oxygen (and the related difference in height) caused by the incommensurability of the surface oxide. For the fit, the in-plane parameters were fixed and only the out-of-plane parameters were varied. In the end only the buckling of the Pd atoms contributed to the final result, since oxygen atoms preferred to stay at their starting positions. Also the buckling of the Pd atoms was restricted, since the four Pd atoms close to the center of the cell were assumed to be of the same average height. As a result, the Pd atoms at the corners of the  $\sqrt{6}$ -cell, which are supposed to be located directly above the densely packed  $[0\bar{1}1]$  rows of the substrate (cf. Sec. 5.3.4), were found to be slightly higher (0.15 Å) than the other Pd atoms. The agreement between calculated and measured superstructure rods was found to be quite good ( $\chi^2 = 0.13$ ) and can be seen in Fig. 5.3.15.

Finally, Pd rods were analyzed to get an idea about the registry shift/stacking between the surface oxide and the Pd substrate and the interlayer distance. However, in order to be able to extract this information, the surface oxide had to be compressed by 14% to reach commensurability. To minimize the effect of this distortion, the occupancy of all atoms in the supercell was set to 86% (43% for each oxygen atoms). In the following, the Pd atoms located in the corners of a  $\sqrt{6}$ -cell were placed in different adsorption sites of the substrate (fcc and hcp 3-fold hollow, top) and the resulting model was then compared to the experimental results. The best agreement between calculated and measured rods was achieved for the top model, confirming the stacking proposed by DFT. Also the according interlayer distance between surface oxide and substrate agreed very well with the theoretical result (SXRD: 2.41 Å; DFT: 2.47 Å).

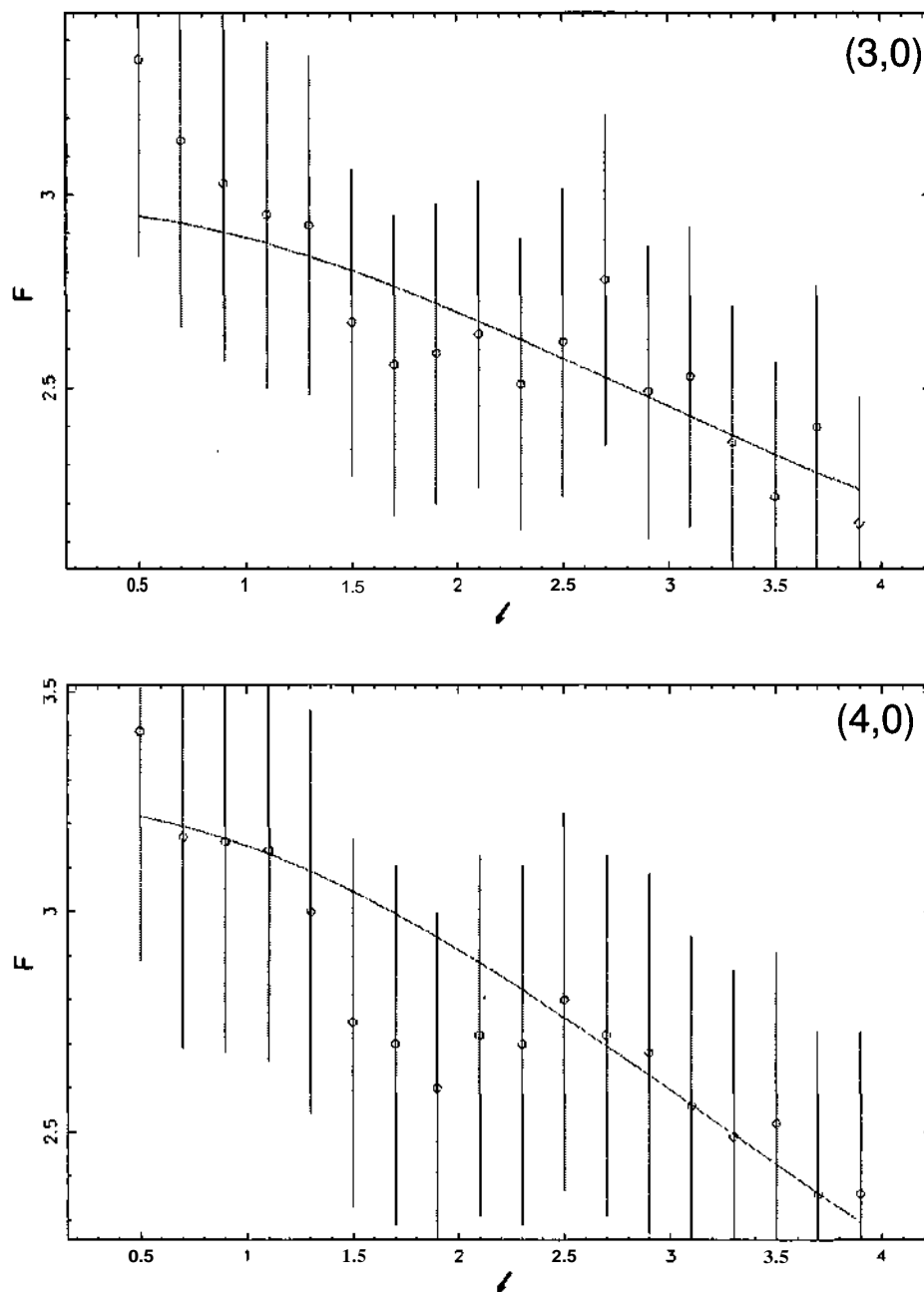


Figure 5.3.15: Agreement between calculated (line) and measured (circles) structure factors  $F$  for two superstructure rods of the first domain. The vertical lines represent the error bars associated with the measured values. The  $l$ -values on the x-axis refer to the out-of-planer reciprocal substrate lattice vector  $\vec{l}$ .

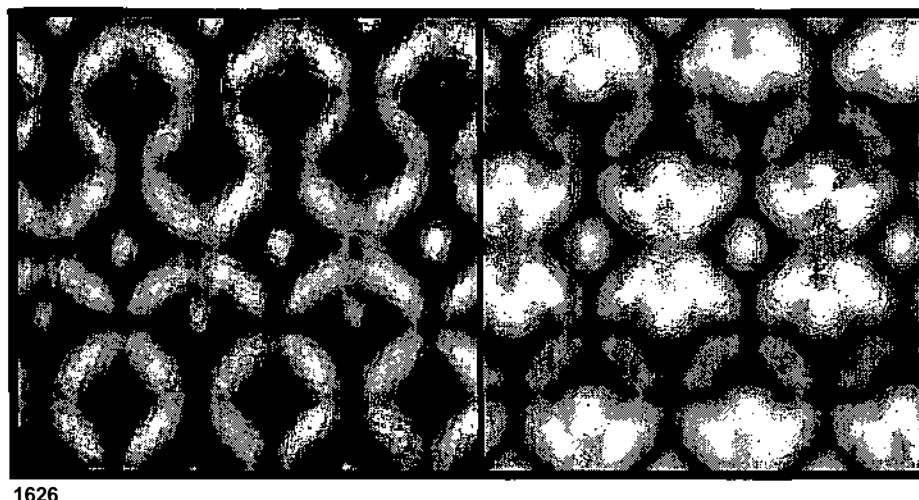


Figure 5.3.16: Comparison between a measured (left) and a calculated (right) STM image of the surface oxide.

### 5.3.6 Conclusions

Due to the excellent agreement of various different experimental and theoretical methods it is possible to state that the structure of the surface oxide on Pd(111) has been resolved. This surface oxide was found to consist of an almost coplanar Pd<sub>5</sub>O<sub>4</sub> overlayer, forming a truly two-dimensional, incommensurate oxide, which shows no resemblance to any bulk oxide that can form at a metal surface. Consequently, it represents an intermediate phase between an oxygen overlayer (discussed in Sec. 5.2) and a bulk oxide and should therefore have interesting consequences for heterogeneous catalysis. At ambient pressure, however, it is very likely that this surface oxide transforms into a bulk oxide with PdO stoichiometry - this assumption is currently under investigation.

All things considered, the analysis of the surface oxide on Pd(111) was not an easy task, mainly due to its incommensurability, which made a quantitative LEED analysis more or less impossible. The very large superstructure unit cells needed (cf. Sec. 5.3.4) and the pronounced buckling involved are problems that are not possible to tackle with LEED at the moment. Nevertheless, the ability of SXRD to completely separate the overlayer from the substrate was of great help to confirm the model proposed by DFT. In the end it was this elaborate DFT analysis (done by G. Kresse), which completely solved the atomic structure. The agreement of the results of these calculations with experiment is truly impressive and can be seen best in a direct comparison between a measured and a calculated STM image (see Fig. 5.3.16). For the sake of completeness it has to be mentioned that additionally a study of high resolution core level shifts (HRCLS) was performed, which also agrees very well with the result presented above (cf. Ref. [59]). Summing up, it can be said that a lot of complementary experimental

techniques as well as an extensive DFT analysis gave a very consistent picture of the structure of this two-dimensional surface oxide, which can therefore be considered to be solved.

## 6 Vanadium surface oxides on Pd(111)

### 6.1 Introduction

Vanadium oxides play an important role in numerous technological applications: They are used e.g. as cathode materials in lithium ion batteries [73] as well as chemical sensors for ethanol and various other organic compounds [74]. The main field of application of vanadium oxides, however, is definitely catalysis (cf. e.g. the production of sulfur acid by using  $V_2O_5$  as catalyst). The reason for that is mainly based on vanadium's ability to appear in a wide range of oxidation states. Stable phases include rocksalt VO ( $V^{2+}$ ), monoclinic  $V_2O_3$  ( $V^{3+}$ ), rutile  $VO_2$  ( $V^{4+}$ ) and orthorhombic  $V_2O_5$  ( $V^{5+}$ ). Therefore, vanadium oxides can serve as catalysts in oxidation as well as reduction reactions. A very interesting effect has been observed for ultrathin vanadium oxides grown on certain appropriate substrates, namely a profound increase in the catalytic activity compared to bulk vanadium oxides. The first time that such an effect has been reported was for monolayer-thick vanadia supported on titania ( $TiO_2$ ) [10, 11]. The origin of this phenomenon, however, is still quite unclear, except for the fact that it has to be a support mediated effect. One reason for this lack of understanding lies in the missing knowledge about the structural details of those oxides. Since vanadia layers tend to form many different surface structures simultaneously, due to the large amount of stable phases caused by the various possible V oxidation states, a conventional structure analysis using diffraction techniques like LEED or SXRD is quite difficult.

Vanadium oxide on Pd(111) is in particular very interesting since it is a model system for the design of a so-called *inverse* strong metal support interface (SMSI) catalyst, which consists of metal-oxide islands on a transition metal [3]. In this system, however, one is also always confronted with mixed phases, which can be analyzed best using local probe techniques such as STM [75], but the atomic structure of these phases could not be determined by experiment. One general finding is that, whenever vanadium oxide is grown on a support, the established phase depends strongly on the deposition conditions [76]. On the other hand - as shown in this work - a careful preparation under appropriate conditions enables the growth of well ordered vanadium surface oxides on Pd(111) covering the entire surface, which makes a quantitative LEED analysis of these structures possible.

Although the growth of thin vanadium oxide films on Pd(111) has been intensely investigated mainly by STM and DFT [75, 77, 78, 79], the structures, which form in the oxygen rich regime with vanadium coverages below 0.3 ML, have not been analyzed in detail so far. In this work, results on this low vanadium coverage regime are presented, showing the formation of a novel, non periodic vanadium-oxide at 0.1 ML, which al-

readily incorporates building blocks of a well ordered  $p(4 \times 4)$  phase. The latter structure is of particular interest due to its extraordinary atomic composition and arrangement, and starts to form at 0.2 ML coverage. An STM study of the transformation from the unordered, non-periodic oxide structure to the above mentioned  $p(4 \times 4)$  structure, which finally covers the whole surface at 0.31 ML, is presented. The  $p(4 \times 4)$  phase is identical to the one reported in Refs. [75] and [80], which was found to be very unstable due to its easy reduction by hydrogen. Therefore one paragraph dealing with the structural changes caused by this reduction process is included, containing a detailed description of the steps necessary for a complete transformation of the  $p(4 \times 4)$  to a  $p(2 \times 2)$  phase. However, the main focus of this part of the work lies on the structural analysis of the highly ordered  $p(2 \times 2)$  and  $p(4 \times 4)$  phases including a detailed DFT and quantitative LEED analysis. Models for both structures have been suggested before, but, in particular, the  $p(4 \times 4)$  phase is so unusual that further experimental support for the uncommon tetrahedral coordination of vanadium atoms was required. This unambiguous support is given in this section by means of a careful quantitative LEED analysis.

## 6.2 Sample preparation & evaporation conditions

Prior to any vanadium deposition the Pd(111) sample had to be as clean as possible, which was achieved as described in Sec. 4.2. The vanadium-oxide was then prepared following the procedures described in Ref. [75], namely by evaporating V from a water-cooled electron beam evaporator, followed by a deposition on the heated Pd(111) crystal (250 °C) in oxygen atmosphere ( $p_{O_2} = 2 \times 10^{-7}$  mbar). The deposition rates were kept rather low ( $\approx 0.25$  ML/min) in order to be able to precisely control the vanadium coverage and to get films, which are as uniform as possible. The amount of deposited V was calibrated with a quartz microbalance and was varied between 0.1 and 0.3 ML. After deposition the sample was cooled down in oxygen atmosphere to prevent unintentional reduction of the prepared oxide layer. In the following, the V coverage will be given and not the surface coverage of the vanadium oxide, i.e. the monolayer values of this chapter are not equal to the actual covered surface area.

In some cases Pd was deposited on a Pd(111) surface, which was already covered with a vanadium oxide, in order to get some additional information on the atomic structure of the oxide. This preparation was performed at room temperature from a second water-cooled electron beam evaporator, also at very low deposition rates of about 0.16 ML/min.

Additionally, in all cases, a retarding voltage (slightly higher than the acceleration voltage of the electrons) was applied to the end of the evaporator in order to prevent

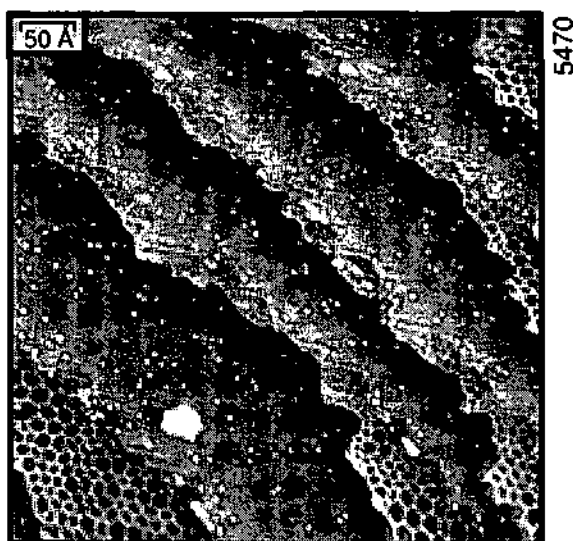


Figure 6.3.1: Room temperature STM image ( $500 \times 500 \text{ \AA}^2$ ,  $-1.03 \text{ V}$ ,  $0.46 \text{ nA}$ ) of  $0.1 \text{ ML}$  vanadium oxide grown on Pd(111), showing a hexagonal, non-periodic surface oxide, which starts to grow from the steps.

unintentional sputtering of the crystal by vanadium or palladium ions, since such accelerated ions have previously been found to profoundly influence the growth of thin films [81].

### 6.3 Low coverage regime - STM results

Fig. 6.3.1 shows an STM image of a Pd(111) crystal after deposition of  $0.1 \text{ ML}$  vanadium as described above. Already at this low coverage an unordered hexagonal oxide starts to grow from the steps, trying to cover as much of the surface as possible. The Auger peak to peak height corresponding to this coverage was measured to be  $1.5 \%$  of the main Pd peak at  $330 \text{ eV}$ , taking the V peak at  $477 \text{ eV}$  as reference. In case of large terraces ( $> 500 \text{ \AA}^2$ ) also the formation of islands was observed. The maximal diameter of these hexagons is very large and was determined to be  $\sim 22.1 \text{ \AA}$ . For comparison, the next neighbor distance on a Pd(111) surface is  $2.75 \text{ \AA}$ , which means that the biggest hexagons are comparable in size to a  $(8 \times 8)$  supercell. It can clearly be seen in Fig. 6.3.1, however, that the size of such a hexagonal structure varies considerably, depending on the vanadium coverage.

At a certain amount of deposited vanadium ( $\approx 0.15 \text{ ML}$ ) nearly the entire surface is found to be covered by this non-periodic phase. From this coverage on, a partial transformation from the original non periodic phase to a quasi-ordered phase starts to occur, which consists of a characteristic, nearly periodic arrangement of large hexagons

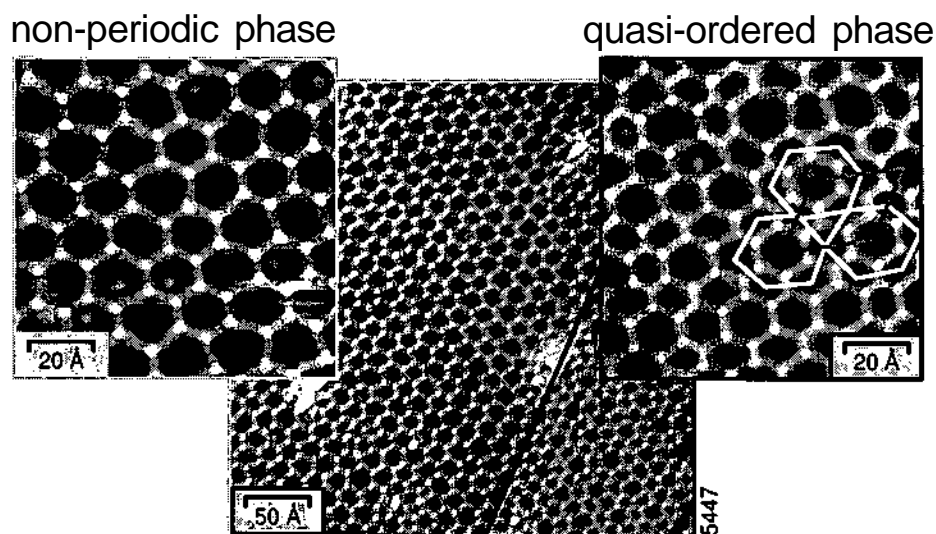


Figure 6.3.2: High resolution STM image ( $250 \times 240 \text{ \AA}^2$ ,  $-1.05 \text{ V}$ ,  $0.46 \text{ nA}$ ,  $0.2 \text{ ML}$ ) of coexisting quasi ordered and non-periodic vanadium surface oxides grown on Pd(111). Smaller images to the left and the right of the main STM image are just magnifications, showing the two phases and the "periodicity" of the quasi ordered one in more detail.

being surrounded by 6 small ones (Fig. 6.3.2). The corresponding supercell size would be roughly a  $(10 \times 10)$ . However, the size of these hexagons varies too much for superstructure spots to be observable by LEED. The apparent hexagon-height with respect to the clean Pd(111) surface was measured to be  $1.3 \text{ \AA}$  and the corrugation amplitude between maxima and minima was  $0.9 \text{ \AA}$ .

Further increase of the vanadium coverage results in a decrease of the average honeycomb size, eventually leading to the formation of an ordered  $p(4 \times 4)$  structure starting at  $\sim 0.2 \text{ ML}$ , as shown in Fig. 6.3.3(a). In this STM image one can identify all three different vanadium oxide phases at once, i.e. the non-periodic, the quasi-ordered and a rather small area covered with the above mentioned, ordered  $p(4 \times 4)$  structure. This ordering can already be observed by LEED, showing a weak  $(4 \times 4)$  diffraction pattern. Increasing the vanadium oxide coverage above  $0.2 \text{ ML}$  causes the surface area covered by the  $p(4 \times 4)$  structure to grow at the expense of the low coverage phases. At the optimal coverage of  $0.31 \text{ ML}$  this perfectly ordered phase covers the entire surface [Fig. 6.3.3(b)], resulting in a very sharp LEED pattern. The corresponding Auger peak to peak height was found to be  $\approx 4.5\%$ . Increasing the coverage above this ideal value results in the formation of other structures as observed in Ref. [78]. Compared to the low coverage phases, the  $(4 \times 4)$  structure seems higher by  $0.7 \text{ \AA}$ , which amounts to an apparent height of  $2.0 \text{ \AA}$ . Also the observed corrugation of  $1.1 \text{ \AA}$  is similar to the one mentioned in Ref. [75]. Taking a closer look at this very beautiful  $p(4 \times 4)$  surface oxide (Fig. 6.3.4), one can identify perfect hexagons built up by three very bright

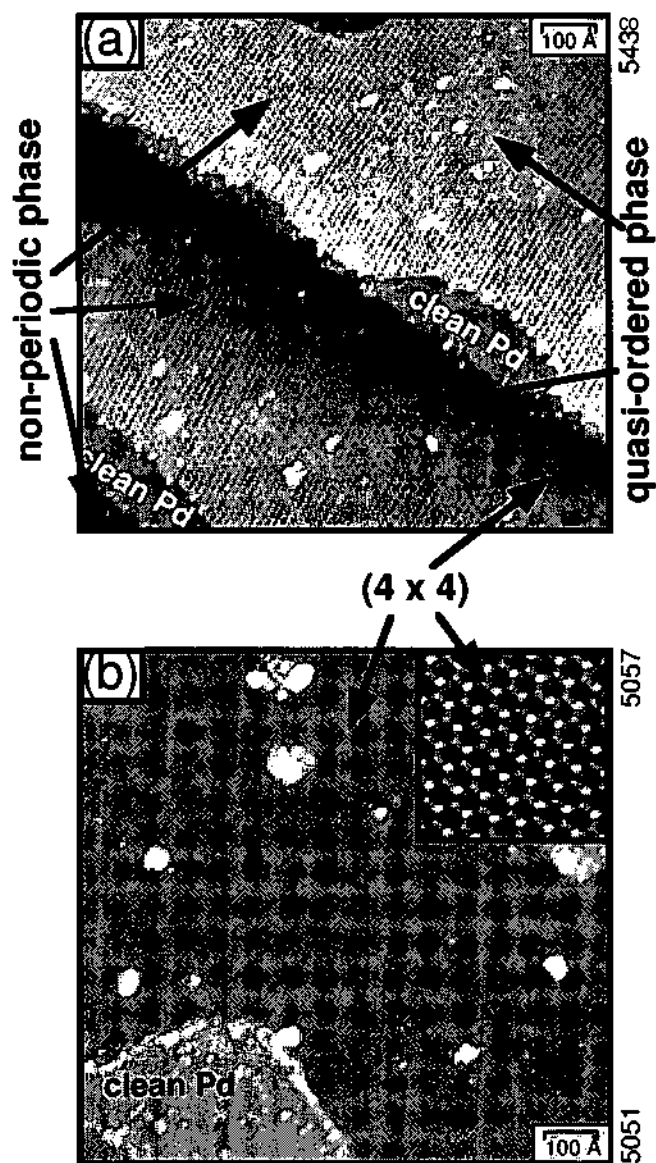


Figure 6.3.3: Room temperature STM images of vanadium surface oxides grown on Pd(111) at different vanadium coverages. (a) Large scale image obtained after deposition of 0.2 ML vanadium, showing a coexistence of three different oxide phases ( $1000 \times 1000 \text{ \AA}^2$ ,  $-1.09 \text{ V}$ ,  $0.46 \text{ nA}$ ). (d) Large scale image of the  $p(4 \times 4)$  phase, covering almost the entire surface ( $1000 \times 1000 \text{ \AA}^2$ ,  $-0.10 \text{ V}$ ,  $0.46 \text{ nA}$ ,  $0.3 \text{ ML}$ ); the inset in the upper right corner shows an atomically resolved magnification of a  $(4 \times 4)$  area ( $71 \times 69 \text{ \AA}^2$ ,  $-0.05 \text{ V}$ ,  $0.46 \text{ nA}$ ).

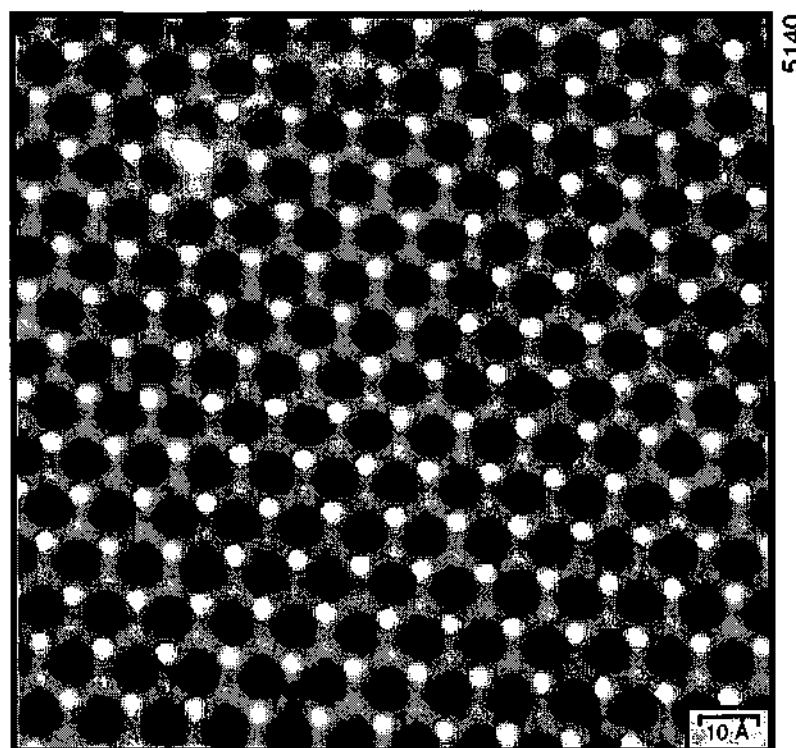


Figure 6.3.4: High resolution STM image ( $129 \times 126 \text{ \AA}^2$ ,  $-1.02 \text{ V}$ ,  $0.46 \text{ nA}$ ,  $0.3 \text{ ML}$ ) of the perfectly ordered  $p(4 \times 4)$  vanadium surface oxide grown on Pd(111).

spots and three slightly darker ones, which are interconnected by lightgray lines. Assuming regular corrugation (i.e. metal atoms appear bright, oxygen appears dark) it is very tempting to attribute the observed spots to vanadium atoms, but everything else remains quite unclear. It was therefore necessary to use other methods to get more information about the structural details of this very interesting surface oxide.

The  $p(4 \times 4)$  structure, however, is easily reduced in the presence of hydrogen [79]. Upon hydrogen exposure the  $(4 \times 4)$  structure begins to dissolve, starting at the phase boundaries to the low coverage phases. Fig. 6.3.5 shows STM images of the decomposition of the above described phases in a hydrogen background pressure of  $4 \times 10^{-9} \text{ mbar}$ . Already after dosing  $0.24 \text{ L}$  (hydrogen doses given in this work are corrected for the sensitivity of the ion gauge) of molecular hydrogen, part of the low coverage phases starts to disintegrate [Fig. 6.3.5(b)], whereas the  $(4 \times 4)$  structure remains predominantly stable until an overall hydrogen dose of  $\sim 1 \text{ L}$ , which is reached at the end of Fig. 6.3.5(c). After the exposure to  $2.1 \text{ L}$  all former phases are completely decomposed, resulting in a network of fractal branches with a local  $(2 \times 2)$  symmetry [Fig. 6.3.5(f)]. Heating the crystal up to  $300 \text{ }^\circ\text{C}$  (5 min) smoothens the surface, resulting in large  $(2 \times 2)$  regions, separated by clean Pd(111) areas. Fig. 6.3.6 shows an STM image of the obtained surface structure, revealing some interesting features, i.e. the occurrence

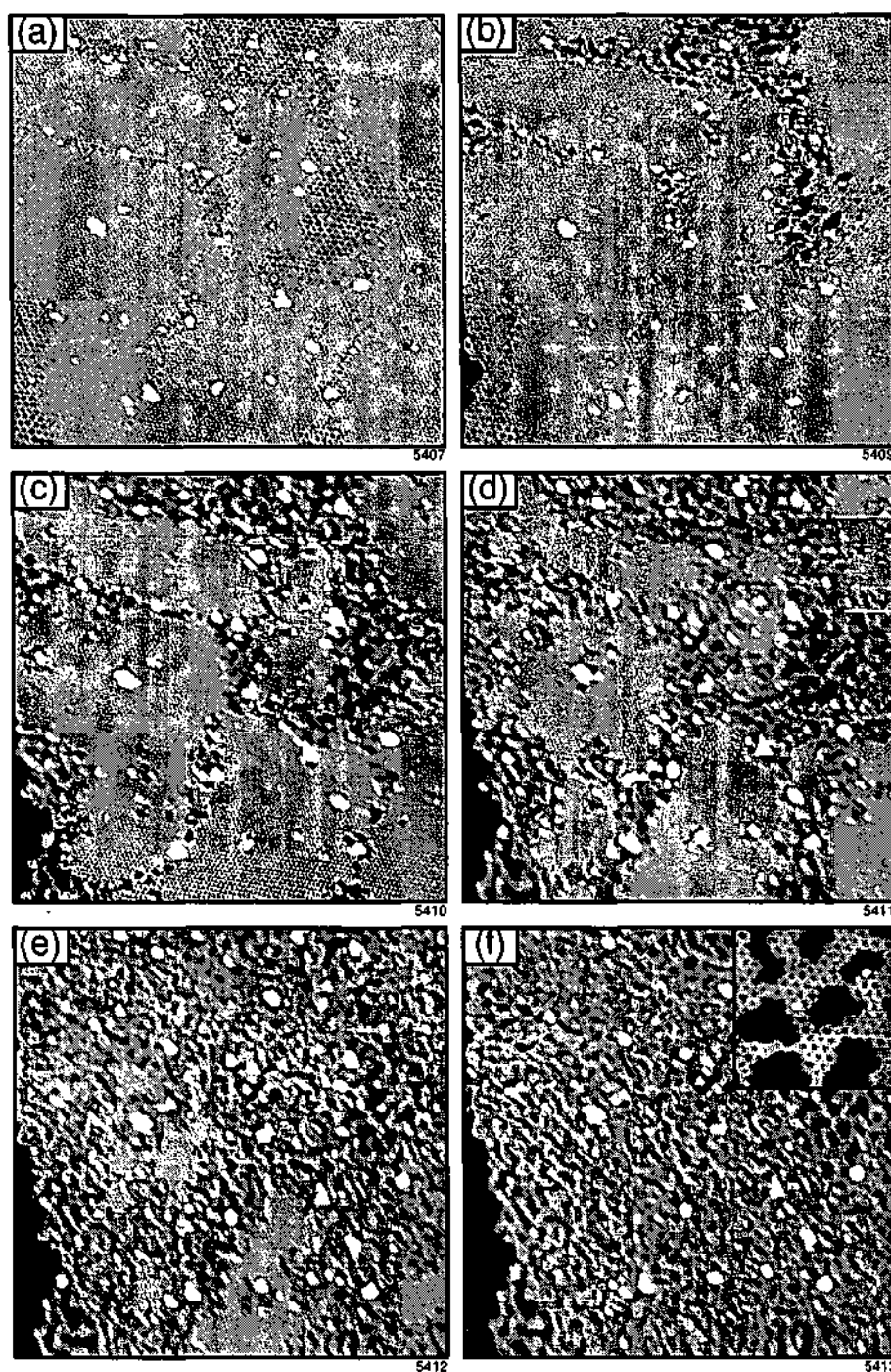


Figure 6.3.5: STM images of the same area of a Pd(111) crystal covered with 0.3 ML vanadium oxide ( $1000 \times 1000 \text{ \AA}^2$ ,  $-1.1 \text{ V}$ ,  $0.46 \text{ nA}$ ). (a) Surface structure before exposure to hydrogen showing large well ordered ( $4 \times 4$ ) areas separated by rather small regions composed of the low-coverage phases. (b)-(f) Images taken at a hydrogen background pressure of  $4 \times 10^{-9} \text{ mbar}$ , the time difference between two successive images was 2.2 min, which is equivalent to a hydrogen dose of 0.53 L. During the reduction process all former phases are completely decomposed resulting in a network of fractal branches with local ( $2 \times 2$ ) symmetry [cf. inset of (f) ( $81 \times 82 \text{ \AA}^2$ ,  $-1.07 \text{ V}$ ,  $0.46 \text{ nA}$ )]

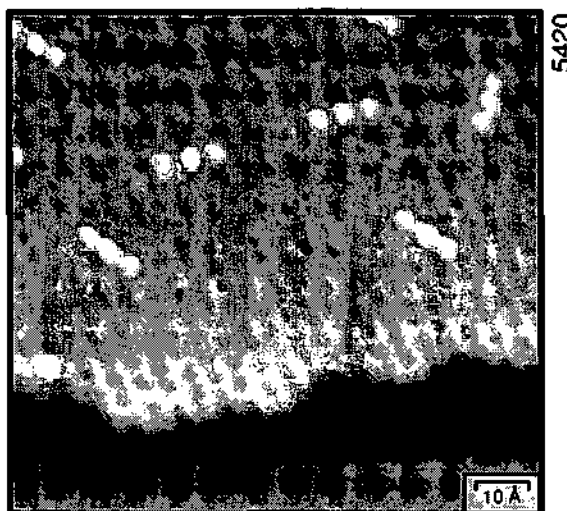


Figure 6.3.6: STM image ( $102 \times 97 \text{ \AA}^2$ ,  $-1.27 \text{ V}$ ,  $0.46 \text{ nA}$ ,  $0.3 \text{ ML}$ ) of a  $p(2 \times 2)$  vanadium surface oxide coexisting with clean Pd(111) areas, obtained after reduction of the  $p(4 \times 4)$  phase with hydrogen, followed by an annealing step (5 min at  $300 \text{ }^\circ\text{C}$ ).

of “nanostructures” consisting of three bright spots, which are arranged in a straight line. It is quite likely that this structure consists of building blocks of the  $(2 \times 2)$  as well as the  $(4 \times 4)$  phase, therefore a model, trying to explain the observed features, is given after the structural details of the ordered phases have been discussed. It is important, however, to stress the fact that the above described post-evaporation treatment always results exclusively in those  $(2 \times 2)$  areas, removing all other phases, up to a vanadium coverage of  $0.5 \text{ ML}$ . These  $(2 \times 2)$  domains are structurally equal to the  $(2 \times 2)$  phase described in Ref. [78], indicating this structure to be the most stable one at a vanadium coverage below  $0.5 \text{ ML}$ .

In the following, a structural analysis of the two ordered phases is presented, including quantitative LEED as well as DFT results. At first the  $(2 \times 2)$  structure is treated, due to its rather simple structure and its easy experimental preparation (caused by its high stability). After that some of the obtained results are used for an analysis of the highly complex  $p(4 \times 4)$  structure.

## 6.4 $(2 \times 2)$ - $\text{V}_2\text{O}_3$

### 6.4.1 Preparation

After sputtering and annealing of the crystal,  $0.3 \text{ ML}$  of vanadium were deposited in an oxygen background as described previously. To obtain a pure  $(2 \times 2)$  reconstruction the

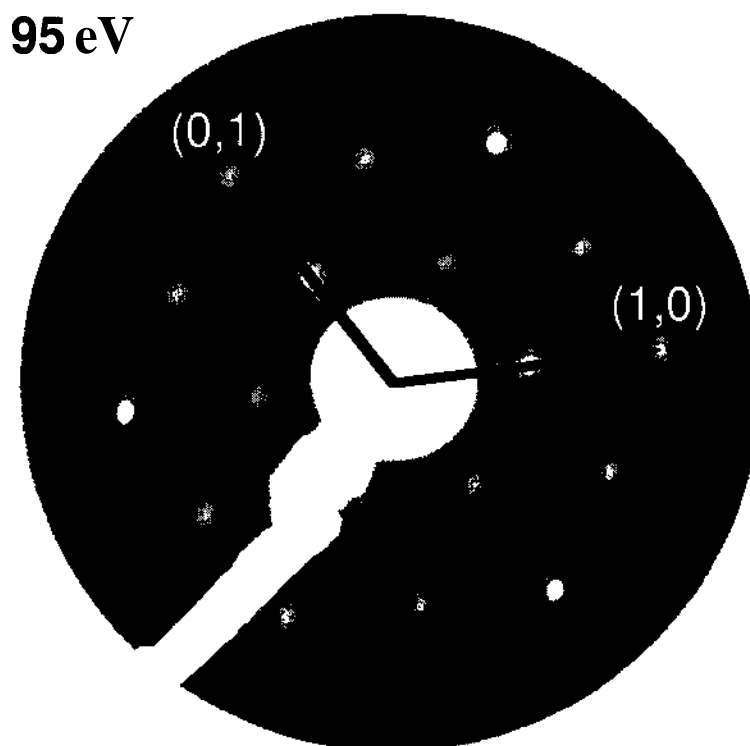


Figure 6.4.1: LEED pattern of the  $p(2 \times 2)$  vanadium oxide phase grown on a Pd(111) substrate, taken at an incident electron energy of 95 eV.

sample had to undergo a hydrogen treatment at 250 °G and  $7 \times 10^{-8}$  mbar hydrogen partial pressure for 5 min, resulting in very sharp  $(2 \times 2)$  superstructure spots, as shown in Fig.6.4.1. Since this preparation results in a vanadium-oxide surface coverage of  $\sim 60\%$ , one is always confronted with a coexistence of the well ordered  $p(2 \times 2)$  phase together with clean Pd(111) areas. This is an important fact, which has to be taken into account in the quantitative LEED calculations, in order to achieve the best possible agreement with the measured  $I-V$  spectra.

## 6.4.2 Quantitative LEED analysis

For the LEED  $I-V$  analysis LEED patterns starting from 30 eV up to 350 eV were recorded, taken images at 1 eV intervals. This enabled the extraction of 12 symmetry-inequivalent beam-sets (5 integer and 7 fractional order beams) and resulted in a cumulative energy range of 2120 eV. The structural models treated in the quantitative LEED analysis of this surface oxide are similar to the DFT trial models proposed in Ref. [75] and are shown in Fig. 6.4.2. For optimization the first 4 Pd interlayer distances and the vanadium and oxygen vertical coordinates were varied within the Tensor-LEED framework. In addition to the consideration of buckling of the surface

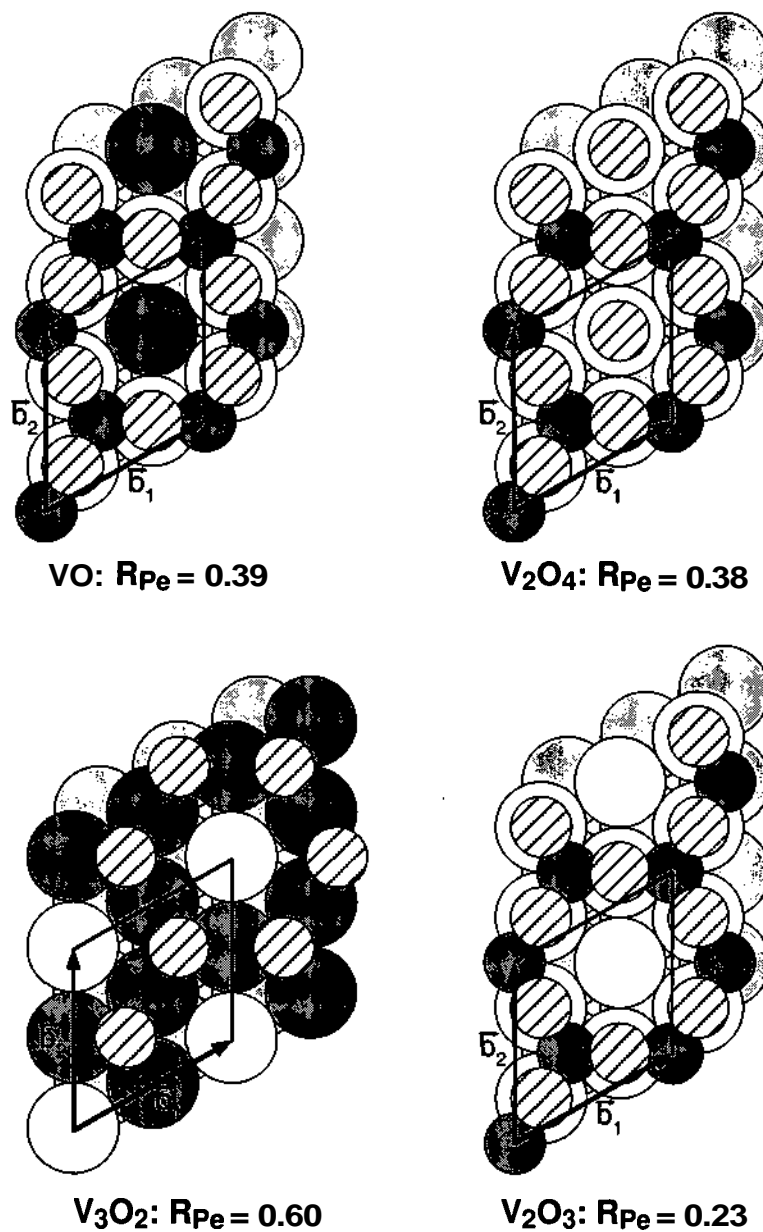


Figure 6.4.2: Structural models for the  $p(2 \times 2)$  superstructure considered in the quantitative LEED analysis. Striped spheres represent oxygen atoms, whereas darkgray spheres are vanadium atoms - the rest are palladium atoms of the first and the second substrate layer.

Parameters	LEED	LEED	VASP
	(pure V <sub>2</sub> O <sub>3</sub> )	(domain mixing)	
vib <sub>O</sub> (Å)	0.32	0.27 ± 0.08	-
d <sub>OV</sub> (Å)	0.66	0.68 ± 0.08	0.71
vib <sub>V</sub> (Å)	0.20	0.18 ± 0.04	-
d <sub>VPd1</sub> (Å)	2.10	2.10 ± 0.03	2.11
b <sub>Pd1</sub> (Å)	0.08	0.10 ± 0.04	-0.04
vib <sub>Pd<sub>center</sub></sub> (Å)	0.15	0.14 ± 0.05	-
vib <sub>Pd1</sub> (Å)	0.13	0.13 ± 0.05	-
Δd <sub>12</sub> (%)	+0.62	+0.66 ± 1.2	+1.96
Δd <sub>23</sub> (%)	+1.07	+0.00 ± 1.87	+0.18
Δd <sub>34</sub> (%)	-1.16	-0.89 ± 1.91	+0
d <sub>bulk</sub>	2.246	2.246	2.246
R <sub>Pe</sub>	0.23	0.16	-

Table 6.4.1: Comparison between the LEED and ab-initio results for the (2 x 2) surface V<sub>2</sub>O<sub>3</sub> structural parameters. Here, d<sub>xy</sub> denotes the averaged vertical distance between atoms/layer x and atoms/layer y; b<sub>x</sub> represents the buckling of the according layer x.

oxide and the first Pd layer, pairing was allowed to occur in those layers, since V atoms located in fcc 3-fold hollow sites have not necessarily to be of the same height as the ones in hcp sites and might consequently cause a different surrounding for the O and the underlying Pd atoms. This type of reconstruction, however, was not found to occur in this system. The imaginary part of the inner potential was optimized fully dynamically, the real part was kept energy independent. Furthermore, the vibrational amplitudes of the atoms of the surface oxide and the first Pd layer were varied and also the vibrational amplitudes of the Pd bulk were allowed to vary slightly for the determination of the best-fit structure. The result of this structural LEED analysis is a confirmation of the model originally proposed by DFT[78], favoring a surface oxide with V<sub>2</sub>O<sub>3</sub> stoichiometry (cf. Fig. 6.4.2). Even very similar models as the VO or the V<sub>2</sub>O<sub>4</sub> model, which differ from the V<sub>2</sub>O<sub>3</sub> structure only in one atomic position (i.e. one different set of phase shifts or one additional oxygen atom per unit cell), can be clearly ruled out.

Considering the (2 x 2) structure only, a Pendry *R*-factor of 0.23 is already achieved for the V<sub>2</sub>O<sub>3</sub> model, with  $R_{Pe}(\text{int}) = 0.27$  and  $R_{Pe}(\text{frac}) = 0.20$ , respectively (cf. Fig. 6.4.3). This rather high value of the *R*-factor for the integer order beams is caused by the disregard of the clean Pd(III) areas. Taking the clean Pd(III) regions into

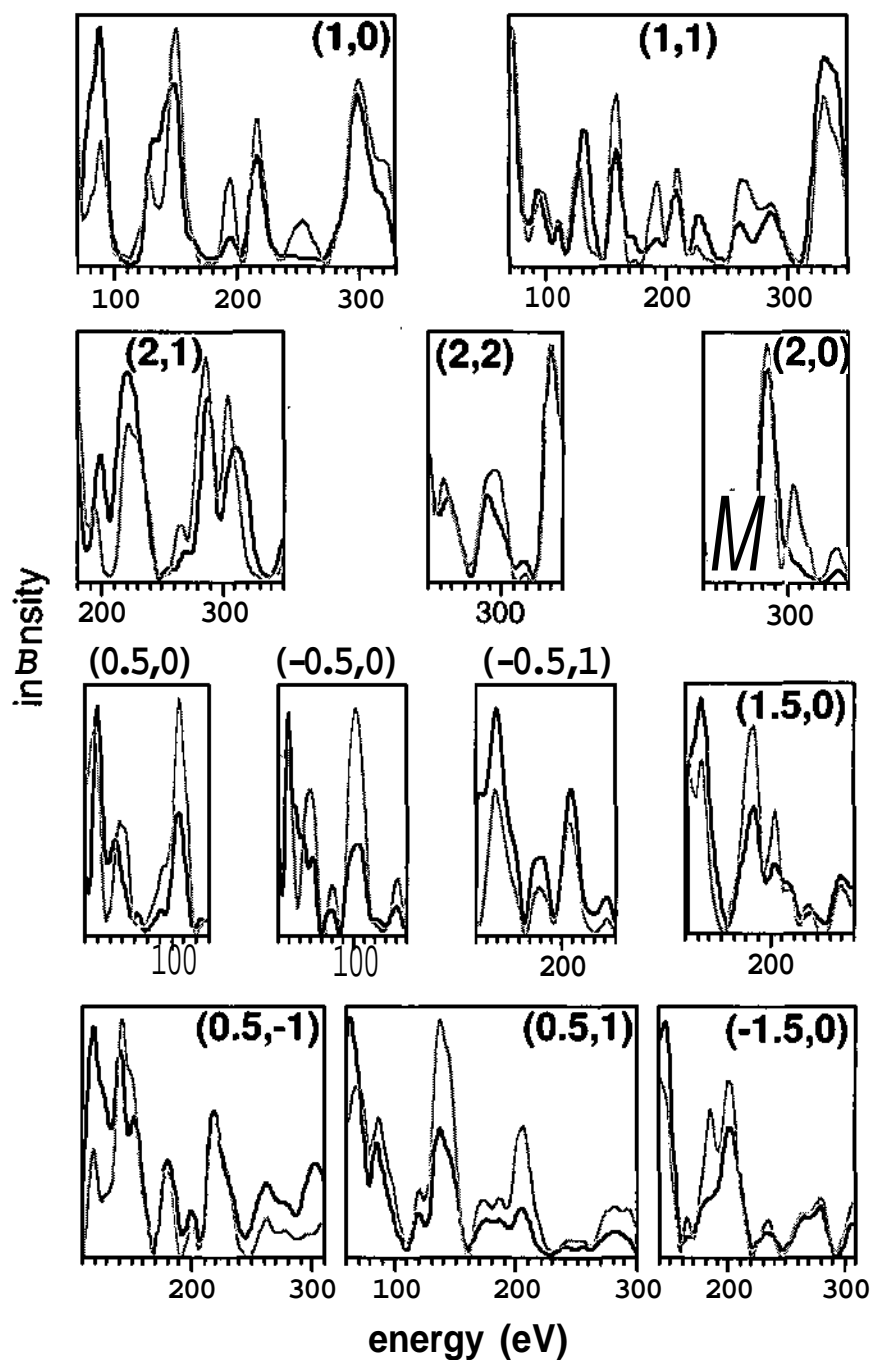


Figure 6.4.3: Comparison between experimental (black) and calculated (gray) LEED I-V spectra of the  $V_2O_3$  surface oxide on Pd(111), obtained without domain mixing. The total energy range amounted to 2120 eV and yielded a Pendry R-factor of 0.23.

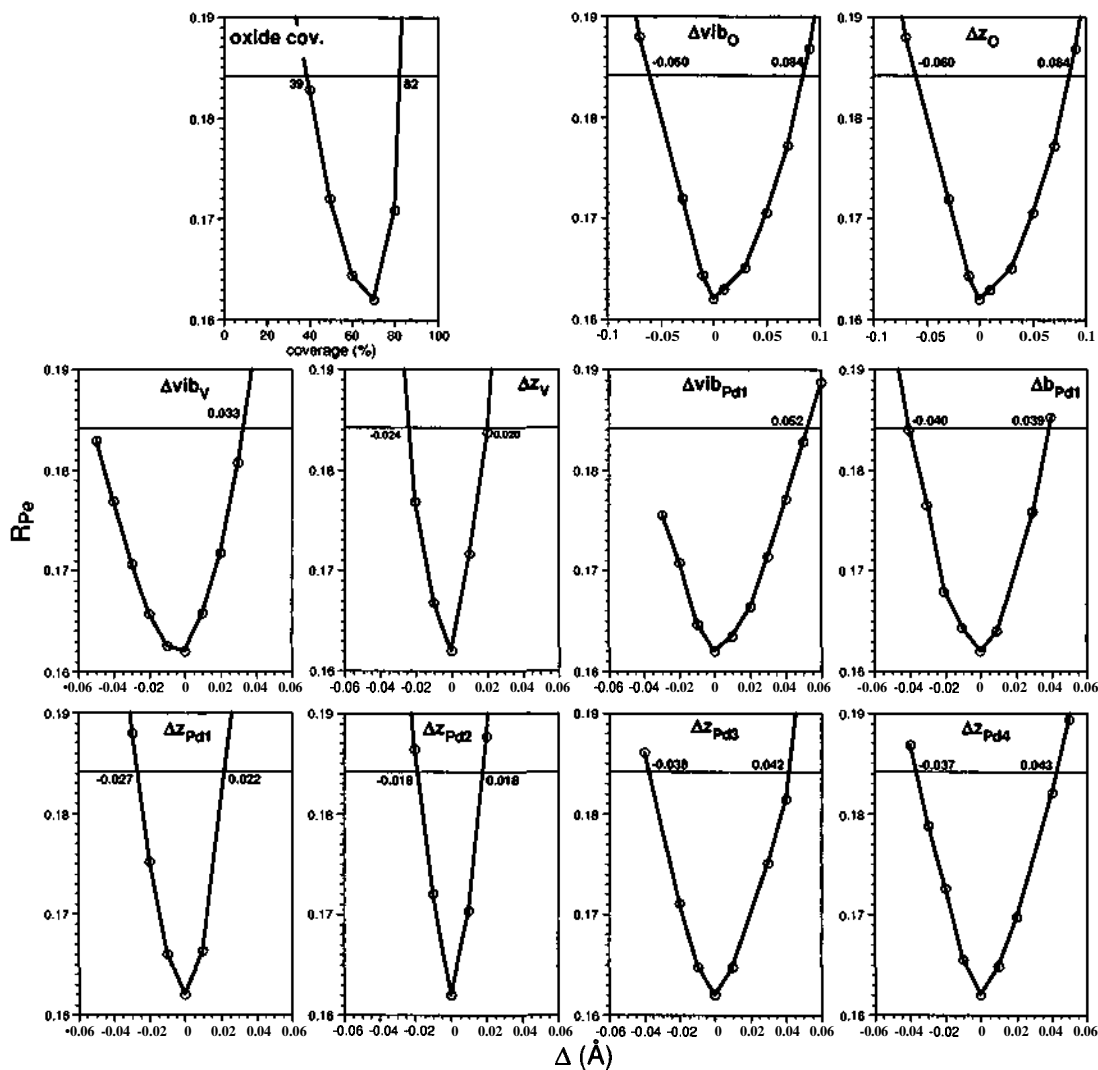


Figure 6.4.4: Error bars of the optimized parameters of the  $p(2 \times 2)$ - $V_2O_3$  surface oxide grown on Pd(111). Deviations from the best-fit structure are given on the x-axis and plotted versus their  $R_{Pe}$ -factors. All models corresponding to  $R_{Pe}$  values below  $R_{Pe} + \text{var}(R_{Pe})$  (black lines) can not be excluded by LEED.

account by domain mixing, results in the final structure with a  $V_2O_3$  surface coverage of 70%, which amounts to an overall  $R$ -factor of 0.16. For this domain mixing all 12 beams (integer and fractional order!) were calculated for an unreconstructed, clean Pd(111) surface, using a (2 x 2) unit cell. Those beams were then mixed with the ones obtained for the surface oxide and compared to the experimental results. For the structural search, the Pd interlayer distances below the clean Pd(111) surface areas and the regions covered with vanadium oxide were assumed to be the same (except for the first Pd-Pd interlayer distance), in order to reduce the number of free parameters, resulting in 12 independently varied parameters in the final structural search. The agreement is indeed excellent, especially considering the problems of LEED in dealing with open structures [23]. The possible errors of this structure determination were obtained according to Pendry's variance ( $var(R_{Pe}) = 0.022$ ) and are shown in Fig. 6.4.4. Obviously, the error bar concerning the vertical position of the O atoms is rather large, while for all other structural parameters the minimum of  $R_{Pe}$  is quite sharp, indicating a very accurate determination. Moreover, the agreement with the DFT values is very reasonable (cf. Table 6.4.1), the only obvious difference being the buckling of the first Pd layer, which might stem from the above mentioned general LEED problem. To allow a direct comparison between theory and experiment, the theoretical positions were scaled by the quotient of the theoretical and experimental Pd lattice constant  $a_{\text{theory}}/a_{\text{exp}} = 1.016$  (experimental in-plane next neighbor distance 2.75 Å, experimental bulk interlayer distance 2.246 Å). The optimized vibrational amplitudes are also given in Table 6.4.1, all others were fixed to the bulk value of 0.12 Å. The best fit values of the inner potential were  $V_{0r} = 6.5$  eV and  $V_{0i} = 5$  eV, respectively.

All in all, the successful determination of the structural parameters of the (2 x 2) structure showed the applicability of quantitative LEED to this kind of surface vanadium oxides and encouraged the analysis of the far more complicated (4 x 4) structure.

## 6.5 (4 x 4)- $V_5O_{14}$

Without any further treatment the above described deposition of 0.3 ML vanadium results in the formation of a perfectly ordered structure with a p(4 x 4) periodicity, which can be directly observed by LEED, showing a very sharp and well pronounced superstructure pattern (Fig. 6.5.1). The quality of the oxide strongly depends on the amount of deposited vanadium (0.31 ML for a perfect layer) as well as on the quality of the vacuum. This surface oxide was found to be stable at room temperature as long as the hydrogen exposure remained well below 1 L. Due to the fact that the experimental results did not deliver enough information, restricting the parameter space sufficiently for a quantitative LEED analysis, a DFT analysis was performed by G. Kresse, which

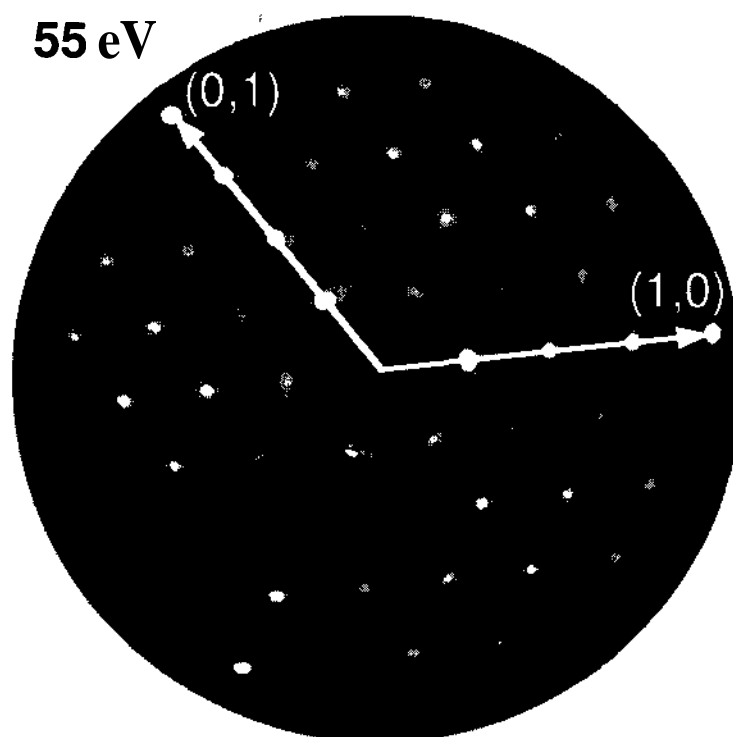


Figure 6.5.1: LEED pattern of the  $p(4 \times 4)$  vanadium surface oxide on Pd(111), recorded at an incident electron energy of 55 eV.

resulted in a reasonable model for the  $p(4 \times 4)$  vanadium surface oxide structure. This theoretical approach is sketched in the next paragraph (cf. Ref. [82]), followed by a detailed description of the quantitative LEED analysis, which confirmed the proposed model.

### 6.5.1 DFT calculations

The determination of a reasonable structural model for the  $p(4 \times 4)$  phase was based on extensive ab initio modeling making use of finite temperature molecular dynamics [83]. Generally speaking, the applied theoretical methods were the same as described in Sec. 5.3.4. The initial ab initio calculations were carried out using three layer thick Pd slabs and a single off-symmetry k-point with the coordinates (0.25, 0.25, 0.0). Such a setup allows for a fairly rapid screening of many conceivable structural models. The information available from experiment was - as mentioned before - rather limited. One crucial hint, however, is that the reduction of the  $p(4 \times 4)$  phase covering the entire surface (i.e. 1 ML oxide coverage) leads to the  $(2 \times 2)$  surface- $V_2O_3$  structure with an oxide coverage of 0.6-0.7 ML [84]. This allows to determine the number of vanadium atoms in the  $p(4 \times 4)$  cell to be either 6 or 5 (the previously mentioned V-coverage

of 0.31 ML for the  $p(4 \times 4)$  phase assumed already the correctness of the structural model). Furthermore, measured core levels suggest that the ratio between oxygen and vanadium atoms should be close to 5:2, similar to the bulk  $V_2O_5$  phase. The only other information available was the honeycomb like image observed in STM.

Screening of possible structural models started with models inspired by the surface  $V_2O_3$  structure, although with a less dense packing and an appropriate number of oxygen atoms coordinated only to a single V instead of two V atoms. This increases the oxygen content of the structure compared to the surface  $V_2O_3$  phase. The stringent requirement for a reasonable candidate is that it should be stable in the surface phase diagrams constructed according to the prescription of Ref. [79]. To meet this criterion the formation energy of the surface oxide must be larger than that of bulk  $V_2O_5$ . However, none of the structures considered initially fulfilled this criterion, on the contrary they were generally rather unfavorable.

In the next step, an attempt was made to interlink octahedral  $VO_6$  building units in such a way that a honeycomb like structure is generated. This attempt, however, failed already at the stage of constructing appropriate models and led to the important conclusion that it is not possible to generate "sparse" two-dimensional (2D) thin oxide films, if the octahedral V coordination is maintained. The octahedral coordination allows only for densely packed 2D or 3D oxides. One-dimensional (1D) chain like units, which are required for a loose packing, can not be assembled using octahedrons, at least not for reasonable oxidation states of vanadium. Partly this is also observed in the bulk oxides, where the less densely packed  $V_2O_5$  structure exhibits a pyramidal instead of octahedral coordination.

To explain the observed structures, a different strategy is required, and a tetrahedral coordination of the V atoms in the oxide is one intriguing possibility. Tetrahedral  $VO_4$  units can be interlinked much more easily in a manner that allows to form open 2D structures and 1D chains. But it is certain that the tetrahedral coordination is less favorable than the octahedral one for vanadium oxides. The larger interaction energy of the open oxide structures with the surface must make up for this energy penalty. Several structures were constructed by interlinking tetrahedrons, and the calculated energies were indeed found to be rather close to those of  $V_2O_5$ , but yet not stable enough to compete with other structures at the surface. In addition, none of these structures exhibited agreement with the observed STM image. In a final attempt, the most stable candidate was subjected to a simple ab initio finite temperature molecular dynamics simulation, in which the temperature was initially set to 1500 K and then gradually decreased to 500 K. Since the model contains around 60 atoms, the simulation time had to be kept short, to a total of 5000 time steps with a time step of 1 fs. Snapshots of this simulation are shown in Fig. 6.5.2. For the initial configuration six tetrahedral

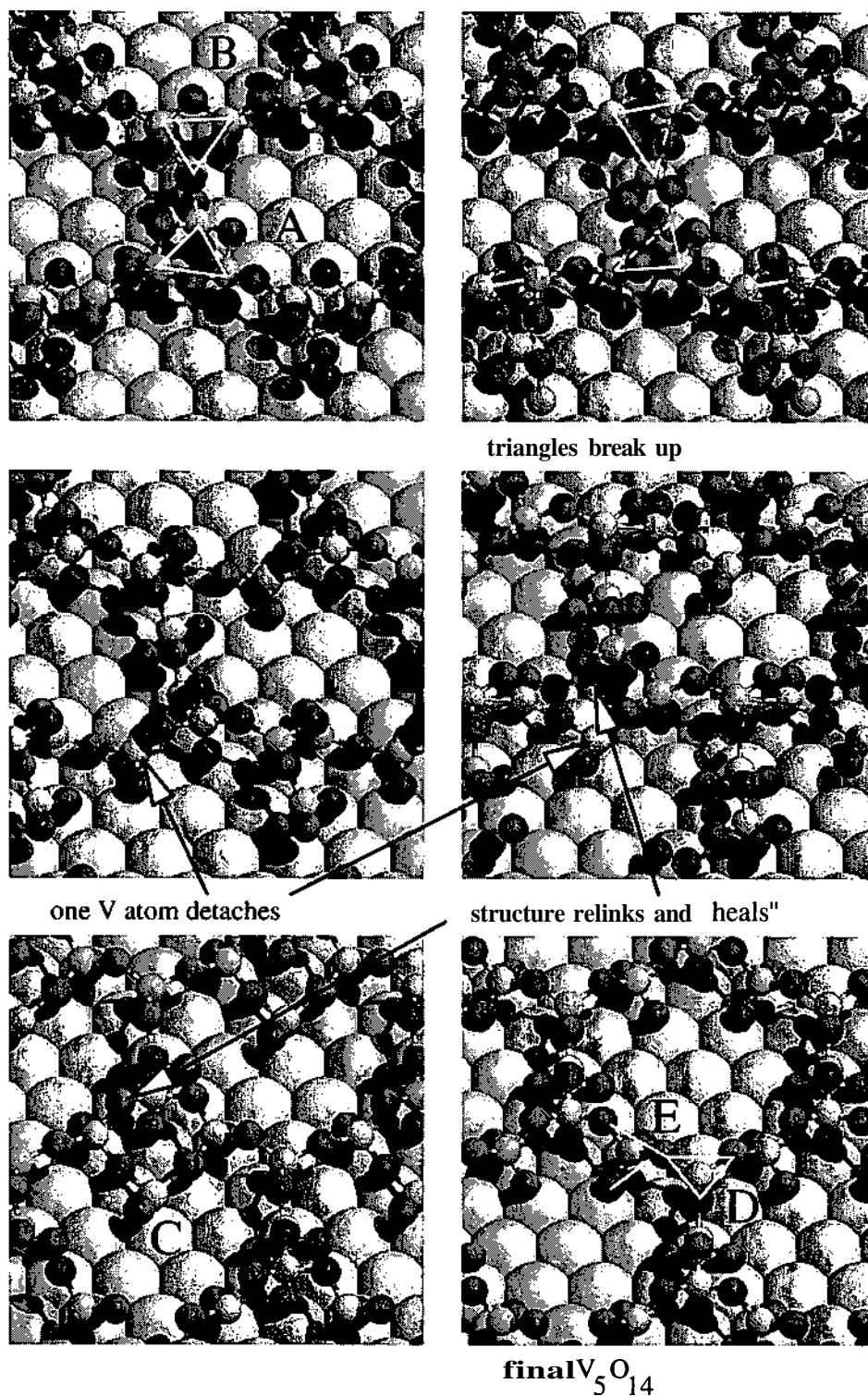


Figure 6.5.2: Snapshots of the finite temperature molecular dynamics simulation of a  $V_6O_{15}$  surface oxide in a  $p(4 \times 4)$  Pd (111) surface cell. Images were taken every 0.4 ps. The final image shows the optimized  $V_5O_{14}$  geometry as determined by DFT. Small light gray and dark gray balls are the vanadium and oxygen atoms, respectively.

units per (4x4) surface cell are visible ( $V_6O_{15}$ ). Three of these units are interlinked to form a triangle (marked A) and the three remaining units are connected to form an inverted triangle (marked B). The triangles A and B are linked in such a manner that a honeycomb like pattern is created. All-together a reasonable structural guess, but the structure is neither sufficiently stable, nor does it reproduce the experimental STM image (each triangle would be visualized as a triangle in the STM). After 0.4 fs, both triangles start to break up (second and third snapshot), next one of the V atoms detaches from the oxide and binds directly to the substrate (third and fourth snapshot), and finally the structure heals to form again a tetrahedrally coordinated network, with five tetrahedral units.

This structure is not yet stable in the phase diagram, but it contains a VO unit (C), which reduces the otherwise high symmetry. When this single unit is removed the final structural model with a stoichiometry  $V_5O_{14}$  is obtained. It has all the desired properties, i.e. its formation energy is sufficiently large that the structure shows up in the surface phase diagram (compare Ref. [84]), the simulated STM images agree very well with the observed images (see Fig. 6.5.6), and the calculated vibrational frequencies match rather well to those measured by EELS [84]. The final structure has in fact rather remarkable properties. It is characterized by  $VO_4$  tetrahedrons, which are interlinked in two different manners. Either the trigonal base of the tetrahedron is parallel to the surface plane with the tip of the tetrahedron pointing towards the substrate (D), or two edges of the tetrahedron are parallel to the surface plane (E). In the latter case, two O atoms are located on top of Pd atoms, binding the oxide to the substrate. The adsorption energy of this oxide on the surface, which is defined as the energy gain for bringing the oxide from the vacuum to the surface, is 10 eV per (4x4) surface cell. Since eight oxygen atoms are coordinated to the surface, one calculates an interaction energy of 1.25 eV per oxygen atom in contact with the surface, which is notably larger than for other oxides [79]. Additionally, the structure allows for a relatively large fraction of the oxygen atoms to be coordinated to the substrate (eight out of 14). Both factors are decisive for the stability of the surface oxide. It is also noted that the oxide is over-stoichiometric, i.e.  $14/5 > 5/2$ ; it contains more oxygen atoms than any known bulk vanadium oxide. This is only possible, because the substrate transfers charge to the oxygen atoms.

### 6.5.2 Quantitative LEED analysis

Due to the large supercell size of the p(4 x 4) structure and the corresponding high number of atoms therein, a parallelization of the full dynamical calculations was necessary in order to be able to compute the corresponding scattering amplitudes in reasonable time. This parallelization was realized by splitting the energy range into small pieces,

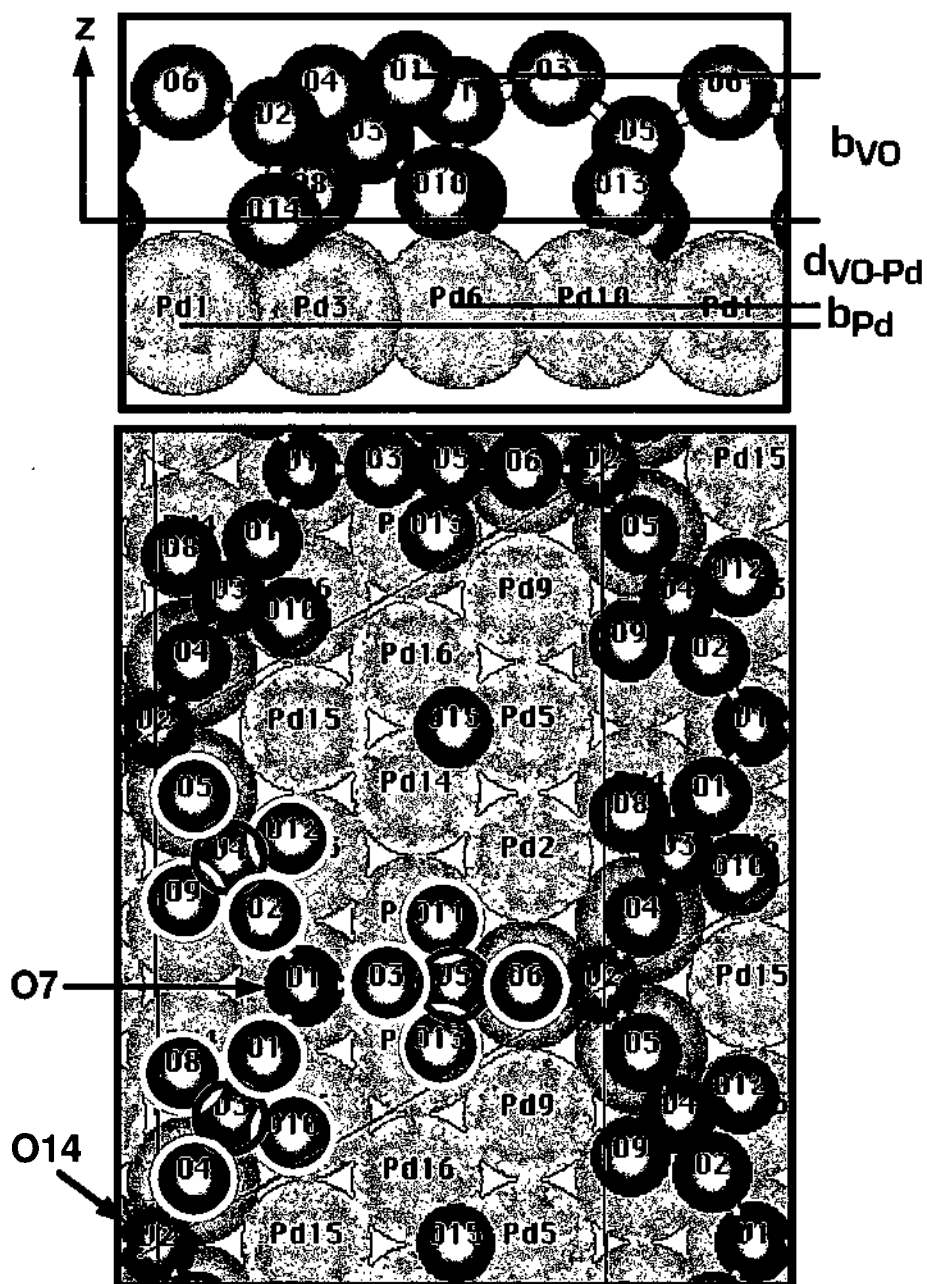


Figure 6.5.3: Structure model of the  $p(4 \times 4)$ - $V_5O_{14}$  surface oxide on Pd(111), consisting of 19 oxide atoms per supercell. Due to the high symmetry of the structure only 8 oxide atoms can be varied independently - symmetry equivalent atoms are encircled with the same color.

Atom	LEED				VASP		
	x (Å)	y (Å)	$\Delta z$ (Å)	vib(Å)	x (Å)	y (Å)	$\Delta z$ (Å)
O1	2.32	4.01	$2.47 \pm 0.18$	0.28	2.32	4.05	2.52
O2	2.32	6.99	$2.47 \pm 0.18$	0.28	2.34	6.96	2.51
O3	4.90	5.50	$2.47 \pm 0.18$	0.28	4.85	5.48	2.52
O4	0.82	1.43	$2.16 \pm 0.18$	0.22	0.84	1.45	2.15
O5	0.82	9.58	$2.16 \pm 0.18$	0.22	0.84	9.54	2.11
O6	7.88	5.50	$2.16 \pm 0.18$	0.22	7.85	5.48	2.13
V1	3.18	5.50	$2.05 \pm 0.05$	0.17	3.18	5.50	2.02
V2	0.00	0.00	$1.66 \pm 0.07$	0.18	0.00	0.00	1.65
V3	1.60	2.76	$1.38 \pm 0.03$	0.20	1.66	2.84	1.37
V4	1.60	8.24	$1.38 \pm 0.03$	0.20	1.66	8.14	1.34
V5	6.34	5.50	$1.38 \pm 0.03$	0.20	6.22	5.47	1.36
O7	3.18	5.50	$0.30 \pm 0.30$	0.20	3.18	5.48	0.40
O8	0.58	3.69	$0.38 \pm 0.10$	0.24	0.58	3.62	0.38
O9	0.58	7.32	$0.38 \pm 0.10$	0.24	0.58	7.33	0.37
O10	2.90	2.34	$0.38 \pm 0.10$	0.24	2.92	2.29	0.42
O11	6.05	6.85	$0.38 \pm 0.10$	0.24	6.07	6.80	0.38
O12	2.90	8.66	$0.38 \pm 0.10$	0.24	2.91	8.67	0.38
O13	6.05	4.16	$0.38 \pm 0.10$	0.24	6.06	4.11	0.41
O14	0.00	0.00	$0.00 \pm 0.30$	0.20	0.02	0.00	0.00
O15	6.35	11.00	-O.xx	0.28	6.38	10.91	-0.56
$d_{O14-Pd}$ (Å)	$1.57 \pm 0.30$				1.64		
$b_{Pd1}$ (Å)	$0.15 \pm 0.25$				0.13		
$b_{Pd2}$ (Å)	$0.13 \pm 0.13$				-		
$\Delta d_{Pd12}$	$+0.02 \pm 0.12$ (Å)				$0.00$ (Å)		
	$(+0.9\%)$				$(0.0\%)$		
$\Delta d_{Pd23}$	$-0.00 \pm 0.14$ (Å)				$0.00$ (Å)		
	$(-0\%)$				$(0.0\%)$		

Table 6.5.1: Comparison between LEED and DFT results concerning the geometry of the  $p(4 \times 4)$ - $V_5O_{14}$  structure. To identify the atoms in the structure see Fig. 6.5.3.

calculating the tensors for every single part, followed by a reassembling of the obtained results. Even by using this computational trick, one full dynamical calculation took about one week.

In the experimental part of the LEED analysis of the p(4 x 4) structure the electron energy was varied between 30 and 300 eV and 15 independent beam-sets were analyzed. The useful data extracted from 5 integer and 10 fractional order beam-sets amounted to a total energy range of 2300 eV. Starting from the oxide structure found by the ab-initio calculation, two different types of stacking were investigated, favoring, after a first optimization step, the one proposed by DFT ( $R_{Pe} = 0.45$  vs.  $R_{Pe} = 0.62$ , for the V2 atoms of Fig. 6.5.3 being located in hcp or fcc sites, respectively). Due to the high symmetry of the structure only 8 out of 19 oxide atoms can be independently varied (cf. Fig 6.5.3), thus reducing the number of parameters considerably, which therefore increases the reliability of the LEED analysis for this extremely complex structure.

By optimizing the vertical coordinates of the independent oxide atoms and the first 2 Pd layers only, already a reasonable agreement between experiment and calculation was achieved, which is represented in the above mentioned Pendry  $R$ -factor of 0.45. Including buckling in the first Pd layer already improved the agreement considerably to  $R_{Pe} = 0.35$ . After a determination of reasonable vibrational amplitudes for the oxide atoms, buckling of the oxide and of the first two Pd layers was optimized independently in several iterations resulting in an  $R_{Pe}$  of 0.27, strongly supporting the proposed model. A dynamical optimization of the vibrational amplitudes of the bulk atoms and the imaginary part of the inner potential was not performed for this structure due to time reasons and because the corresponding values gained from the analysis of the (2 x 2) structure were considered to be sufficiently applicable. Also an optimization of the in-plane coordinates of the oxygen atoms was omitted due to LEED's insensitivity to these parameters and in order to prevent an unnecessary increase in the already rather high number of independent parameters. As a matter of fact, already the exact vertical position of atoms, which don't have any symmetry equivalent partner in the (4 x 4)-cell, can not be determined by LEED with very high accuracy (cf. Fig. 6.5.5). A comparison of all calculated  $I-V$  curves, using the best-fit structure, with the measured ones is presented in Fig. 6.5.4, showing satisfactory agreement for every single beam. It has to be mentioned that for an open structure of this complexity quantitative LEED has never been applied so far - in that respect the achieved agreement is really excellent.

Finally, since this oxide has a very open structure, it is very likely that the above described preparation resulted in additional oxygen adsorbed in the centre of the hexagons. This additional oxygen, which is not a part of the oxide, is depicted in Fig. 6.5.3 and labeled O15. However, it is not possible to verify the existence of this

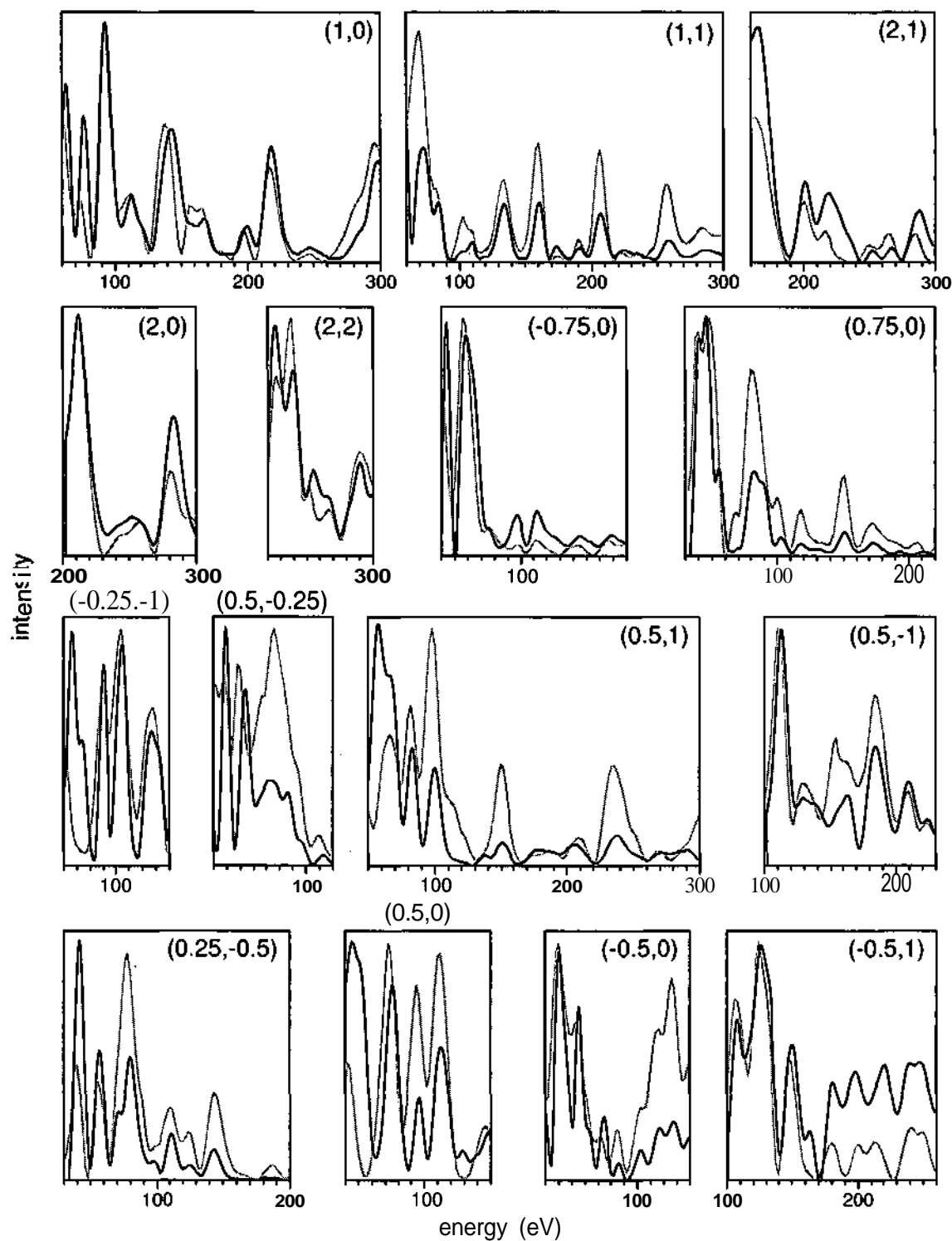


Figure 6.5.4: Comparison between experimental (black) and calculated (gray) LEED  $I$ - $V$  spectra of the best-fit model found for the  $p(4 \times 4)$ - $V_5O_{14}$  surface oxide on Pd(111). The total energy range amounted to 2300 eV and yielded a Pendry  $R$ -factor of 0.27.

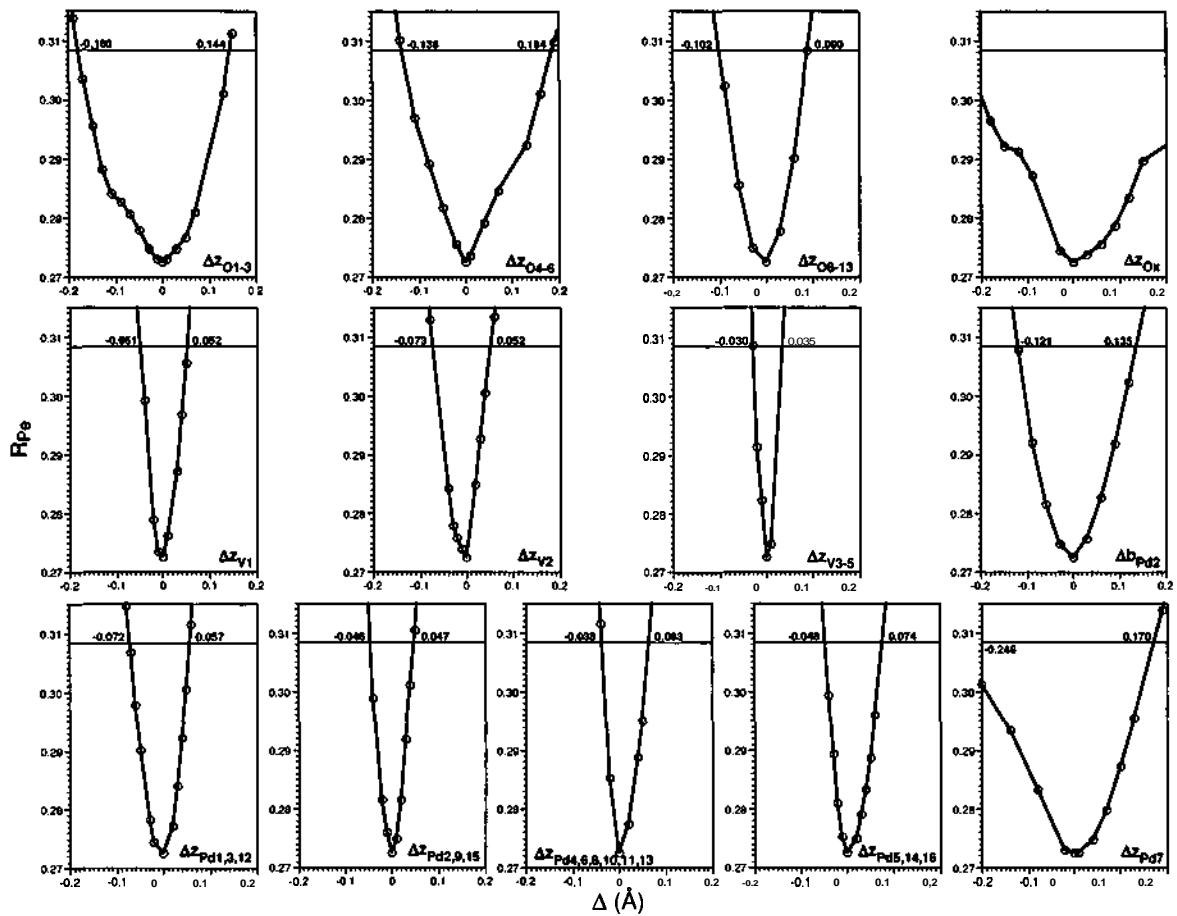


Figure 6.5.5: Possible errors of the atomic positions as determined by LEED, evaluated according to Pendry's variance ( $\text{var}(R_{Pe}) = 0.04$ ). While the location of atoms with symmetry equivalent partners can be determined with reasonable accuracy, this is not the case for single, independent atoms in the  $(4 \times 4)$ -cell ( $\Delta z_{Ox}$  represents the vertical uncertainty associated with 07 and 014, respectively).

atom with LEED, since a correct treatment of the O15 atom would require the computation of a composite layer consisting of the oxide and the first Pd layer, which would involve too many atoms for a LEED calculation. More detailed information on the "pocket"-content, however, is given below. The coordinates of the best-fit structure obtained by LEED and the corresponding DFT values are given in Table 6.5.1 (theoretical values were rescaled to fit the experimental substrate structure as described in Sec. 6.4.2), showing a very good agreement and therefore confirming the structure proposed by the ab-initio calculation. The possible errors involved in this quantitative LEED analysis are presented in Fig. 6.5.5 and were determined based on the atomic positions of the final structure (cf. Table 6.5.1).

Further confirmation of the proposed structure is given by the comparison between

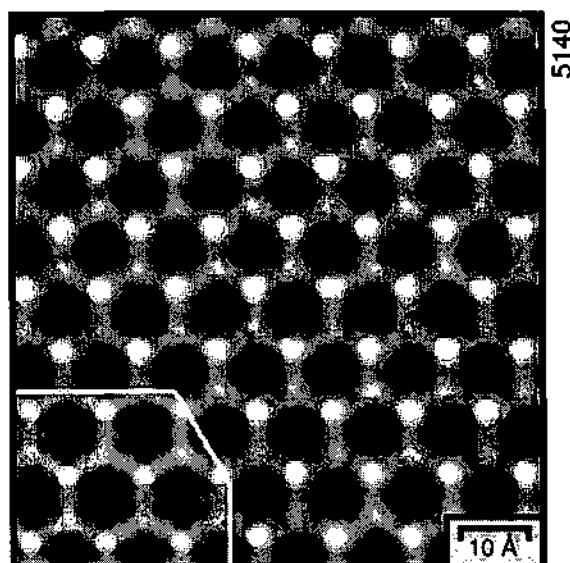


Figure 6.5.6: Comparison of an experimental STM image of the  $(4 \times 4)$ - $V_5O_{14}$  structure ( $77 \times 80 \text{ \AA}^2$ ,  $-1 \text{ V}$ ,  $0.46 \text{ nA}$ ,  $0.3 \text{ ML}$ ) with a simulated image of comparable supercell-size (inset in the bottom left corner).

measured and simulated STM-images (Fig. 6.5.6). The interpretation of those images is very straightforward if one compares them with the structural model. The bright spots depicted by the STM are the vanadium atoms, where the brightness corresponds directly to their height. In that respect, the brightest spots represent the V1 atoms of Fig. 5, the slightly darker ones the V2 atoms. In both cases, an oxygen atom is located between the vanadium atom and the palladium surface lifting the metal atom up considerably. The height difference of  $0.4 \text{ \AA}$  is caused by the different adsorption sites of the oxygen atoms, which are on-top for V1 and in the 3-fold hollow for V2. The lowest vanadium atoms V3, V4 and V5 are symmetrically equivalent and can be seen as gray connections between the corners of the hexagons. The oxygen atoms, however, are not visible in the STM images.

### 6.5.3 Reaction pockets

As pointed out in the last paragraph, the content of the oxide-pockets can not be determined by LEED. DFT calculations and physical reasoning, however, suggest an occupation with one oxygen atom. Further support for this point of view comes from STM images of the  $(4 \times 4)$  structure after an additional deposition of  $0.2 \text{ ML}$  palladium. As shown in Fig. 6.5.7, the Pd atoms tend to agglomerate on the areas covered by the low coverage phases, obviously due to the larger pocket-space, whereas nearly no change of the  $(4 \times 4)$  regions is observable. Taking a closer look reveals the fact that indeed some

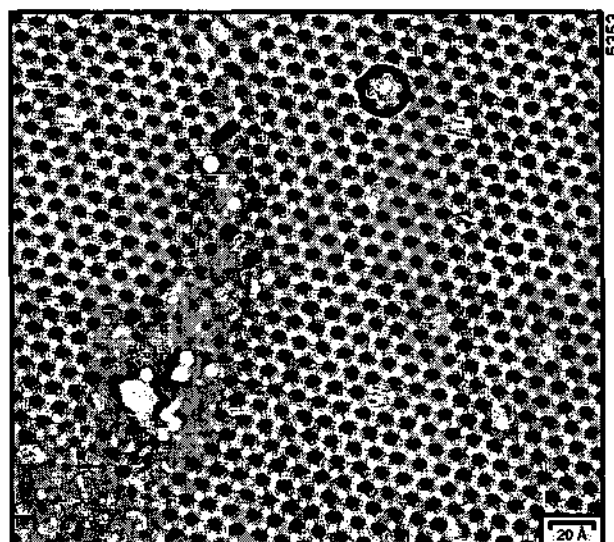


Figure 6.5.7: STM image taken after the deposition of 0.2 ML Pd on a Pd(111) surface, which was nearly completely covered with a  $p(4 \times 4)$  vanadium oxide ( $276 \times 250 \text{ \AA}^2$ ,  $-0.98 \text{ V}$ ,  $0.46 \text{ nA}$ ,  $0.3 \text{ ML}$ ). Within the circle a  $(4 \times 4)$  hexagon is shown, where a Pd atom was able to adsorb.

of the  $(4 \times 4)$ -pockets are filled, indicating former empty pockets. Arguing this way one finds that  $\sim 97\%$  of all pockets are occupied by an oxygen atom, preventing palladium adsorption. Keeping that in mind while taking a closer look at Fig. 6.5.6, one can indeed identify one single hexagon in the middle of the second row of the experimental STM image, which shows a nearly perfect agreement with the simulated one (calculated for an empty pocket), thus providing further evidence for the correctness of the presented analysis.

One interesting fact about these pockets is that they could be very well suited to catalyze oxidation reactions - due to their rather large pocket space - as e.g. the oxidation of CO to  $\text{CO}_2$ . It could be possible, however, that it is necessary to get rid of the adsorbed oxygen (O15) in order to increase the catalytic activity. Further work will be required elucidate these points.

#### 6.5.4 Simple nanostructures — $\text{V}_5\text{O}_{14}$ building blocks

As indicated in Sec. 6.3, the reduction of the  $(4 \times 4)$ - $\text{V}_5\text{O}_{14}$  surface oxide with 2.1 L of hydrogen, followed by a thermal treatment at  $300 \text{ }^\circ\text{C}$  results in a smooth surface, covered by large  $(2 \times 2)$ - $\text{V}_2\text{O}_3$  regions and some clean Pd(III) areas. As shown in Fig. 6.3.6, "nanostructures" consisting of three bright spots arranged in a straight line can be found in the vanadium oxide regions of the obtained surface. Taking a closer

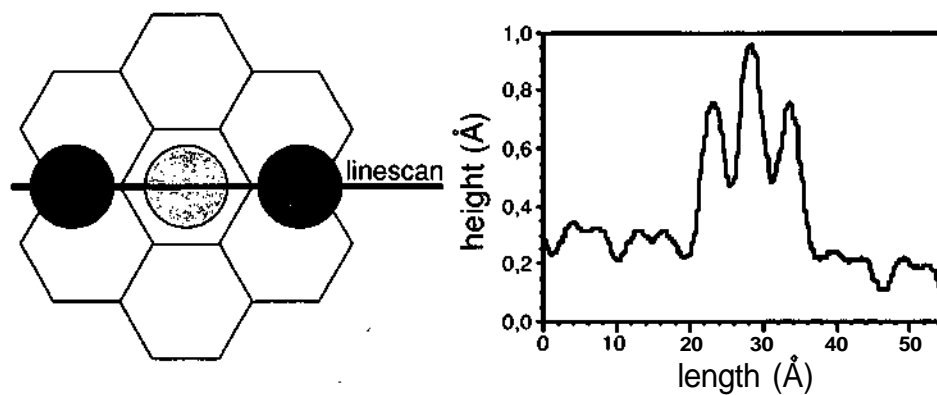


Figure 6.5.8: Linescan along one of the nanostructures shown in Fig. 6.3.6 (right) – left side sketches the position of the maxima with respect to the honeycombs.

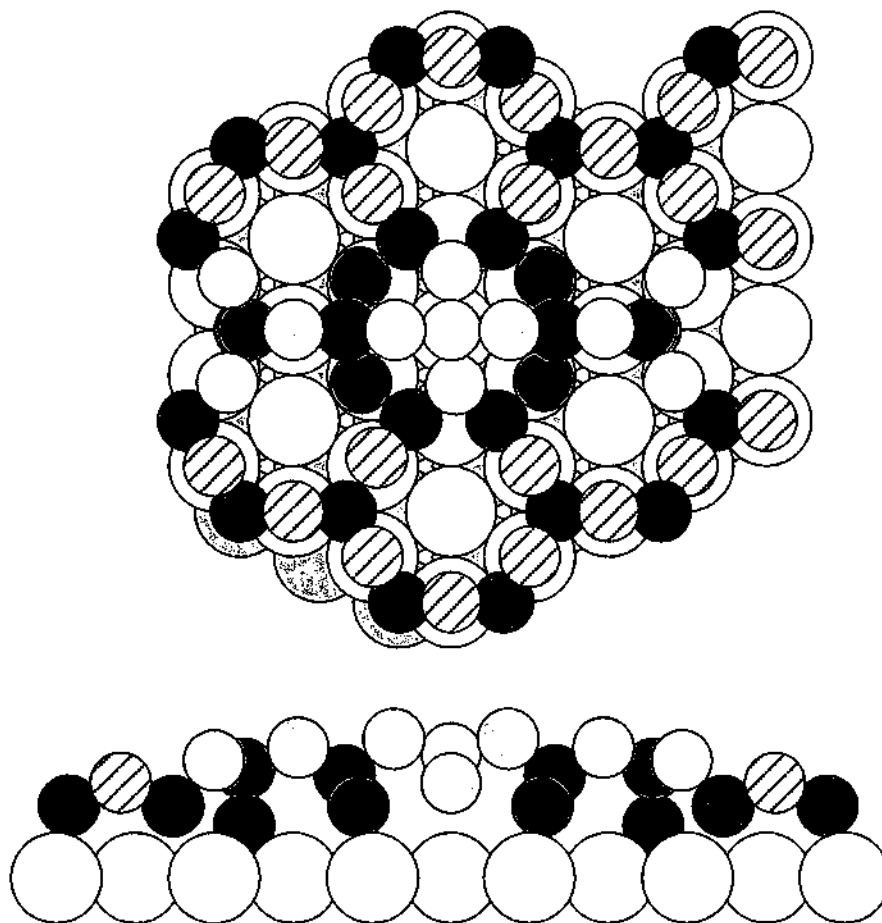


Figure 6.5.9: Structure model for the observed nanostructures, constructed using tetrahedral building blocks of the  $(4 \times 4)\text{-V}_5\text{O}_{14}$  surface oxide. Vanadium atoms are red, oxygen atoms blue.

look, reveals the fact that the maximum in the center of these structures lies in the center of a honeycomb, whereas the other two are located at the end of a former honeycomb edge (cf. Fig. 6.5.8). According to the linescan of Fig. 6.5.8, the central maximum is located about  $0.6 \text{ \AA}$  higher than the  $(2 \times 2)$  structure. The other two maxima are found to be slightly lower than the central one ( $0.2 \text{ \AA}$ ), but still  $0.4 \text{ \AA}$  above the rest of the oxide.

Due to the fact that this structure appears after the reduction of the  $V_5O_{14}$  phase, it is very likely that it can be constructed using tetrahedral building blocks as described in Sec. 6.5.1 and combining them with the regular  $V_2O_3$  structure. Fig. 6.5.9 shows a model, that would explain the observed corrugation by combining a tetrahedral structure named D in Fig. 6.5.2 with the one named E, connecting it to a slightly modified tetrahedron in the middle of the structure and continuing symmetrically. This way it is also possible to create D-E-E-D chains, which can be used to construct large hexagons as observed for the low coverage phases. Consequently, it can be assumed that the building blocks found for the  $V_5O_{14}$  surface oxide are indeed the basic units needed to form one-dimensional or open two-dimensional vanadium oxide structures.

## 6.6 Conclusions

The growth of very low coverages ( $< 0.31 \text{ ML}$ ) of vanadium oxide on Pd(111), prepared by reactive evaporation, has been investigated by scanning tunneling microscopy. First of all, the formation of an unordered, non-periodic structure composed of large hexagons (diameter  $< 22.1 \text{ \AA}$ ) was observed, which partly started to transform into a quasi-ordered phase, consisting of roughly  $(10 \times 10)$  supercells, at about  $0.15 \text{ ML}$ . At a vanadium coverage of  $0.2 \text{ ML}$  an ordered  $p(4 \times 4)$ - $V_5O_{14}$  begins to develop, which eventually covers the entire surface ( $0.31 \text{ ML}$ ). Additionally, the total decomposition of the above described phases due to a reduction caused by the presence of hydrogen was investigated. Already after the exposure to  $2.1 \text{ L}$  of  $H_2$  at room temperature the whole surface changed, showing a network of fractal branches with local  $(2 \times 2)$  symmetry. This structure, however, can be healed by annealing at  $300^\circ\text{C}$ , resulting in a well ordered  $(2 \times 2)$ - $V_2O_3$  structure. The well ordered  $p(2 \times 2)$  and  $p(4 \times 4)$  structures have been analyzed by DFT and quantitative LEED, resulting in a confirmation of the proposed DFT-models by LEED.

One remarkable result, however, is that tetrahedrally coordinated  $VO_4$  units are stabilized at the Pd(111) surface in the low coverage, oxygen rich limit. This is quite surprising since most bulk vanadium oxides exhibit an octahedral (or pyramidal) coordination. The surface, therefore, makes a difference for thin oxides; it is capable to alter the preferential coordination of vanadium, although the vanadium atoms are not

in direct contact to the substrate. The main reason for this behavior is that tetrahedral building units can be assembled into 1D chain like structures, whereas octahedral units require a rather dense packing into 2D or 3D networks. The resulting 1D and open 2D structures facilitate an efficient coordination of oxygen atoms to the surface, as well. The building units determined for the  $p(4 \times 4)\text{-V}_5\text{O}_{14}$  phase, also serve as template for understanding the structures observed at even lower V coverages. It is possible to form 1D chains by interconnecting unit E of Fig. 6.5.2. It is therefore quite likely that chains with the sequence D-E-E-D correspond to the edges of the larger hexagons observed at a coverage below 0.2 ML V.

Generally speaking, the possibility to stabilize open unconventionally coordinated and reactive structures at metal surfaces seems to be an interesting field of research. The catalytic properties of the  $p(4 \times 4)\text{-V}_5\text{O}_{14}$  network are still unknown and require some additional research efforts. Also the role of such tetrahedral  $\text{VO}_4$  units for the catalytic properties of vanadium oxides is unclear and has to be investigated in the future.

## 7 Summary

Two different types of surface oxides that can form on a Pd(111) surface were investigated using local probe (STM), diffraction (LEED, SXRD) and spectroscopic (AES) techniques. This large variety of, partly complementary, experimental methods was supported by the results obtained from a highly sophisticated theoretical method, i.e. molecular dynamics calculations based on DFT (done by G. Kresse). Only the combined effort of all these techniques allowed for a detailed structural determination of the, for the most part very complex, surface oxides.

At first the oxidation of clean Pd(111) surfaces was studied, resulting in the identification of a chemisorbed  $p(2 \times 2)$  overlayer already after exposure to 10 L  $O_2$  at room temperature. As long as the temperature was not increased (and only molecular oxygen was dosed), it was not possible to establish any different surface structure with an oxygen coverage higher than 0.25 ML. Consequently, this rather simple reconstruction was analyzed by quantitative LEED, acting as a warm-up for the real complex structures to come, and resulting in the identification of oxygen atoms being located in every other *fcc* 3-fold hollow site. At higher temperatures ( $\approx 320^\circ\text{C}$ ), however, the formation of a strictly two-dimensional surface oxide was observed (at oxygen partial pressures  $> 4 \times 10^{-6}$  mbar), causing a very complex LEED pattern. This pattern was resolved to be the result of electrons being scattered from three different domains of a square superstructure (side length  $\sqrt{6}$  times the substrate's next neighbor distance) residing on the hexagonal Pd(111) substrate. While one diagonal of a square unit cell of this surface oxide was found to be commensurate, the other one was incommensurate, causing additional difficulties in the structure determination process. The evaluation of STM and AES results led to two in-plane structure models consisting of 5 Pd atoms and 4-5 O atoms per  $\sqrt{6}$ -cell. In the following, both, DFT and SXRD, agreed on the  $Pd_5O_4$  model as being the correct one. Further, more detailed information on the buckling and the coordination of the oxygen atoms, however, could only be obtained from the DFT calculation, wherein a large supercell, consisting of 7  $\sqrt{6}$ -cells, was used, which was compressed by  $\sim 1\%$  to achieve commensurability. Since a slight compression by about 1% was also observed by SXRD, it is quite likely that this supercell indeed represents the exact atomic structure of the surface oxide. The reason for the required elevated temperature for the formation of this surface oxide was found to lie in its lower Pd density compared to a clean Pd(111) surface. Oxygen atoms have to be able to penetrate the Pd surface and to free Pd atoms, which are then diffusing around, eventually forming peninsulas and islands together with oxygen. Since this process involves an extensive mass transport over mesoscopic distances, an elevated temperature is necessary in order to enable the formation of this surface oxide. Although this two-dimensional oxide shows no resemblance to any bulk oxide of Pd, it nevertheless was

found to represent a thermodynamically stable configuration at intermediate oxygen pressures and might consequently play a certain role in catalytic processes mediated by palladium. Since the calculated adsorption energy of the two-dimensional oxide lies between that of a (2 x 2) overlayer and the bulk oxide PdO, it is concluded that its ability to supply oxygen for oxidation reactions will also lie between these phases. One may therefore speculate that kinetics will allow easier oxidation via reduction of the surface oxide as compared to reduction of PdO. In this respect, the oscillatory behavior encountered in CO oxidation reactions catalyzed by Pd at high O<sub>2</sub> to CO ratios could also be explained as being caused by formation-deformation cycles of Pd surface oxides, which would render the subsurface oxygen model obsolete.

The second major topic of this work concerned surface vanadium oxides grown on Pd(111). Here, the ultralow coverage regime was investigated, i.e. vanadium coverages < 0.3 ML. Under appropriate deposition conditions (250 °C substrate temperature,  $p(\text{O}_2) = 2 \times 10^{-7}$  mbar) the formation of more or less one-dimensional structures was observed, arranging in large hexagons with a maximum diameter of  $\sim 22$  Å. With increasing V-coverages the average diameter of these hexagons decreases, eventually leading to the formation of a very well ordered honeycomb-like structure with (4 x 4) periodicity. This kind of vanadium surface oxides, however, was found to be quite sensitive to the presence of hydrogen, because already after having dosed 2.1 L of H<sub>2</sub> the surface structure has changed profoundly, due to the complete disintegration of the above described phases, resulting in a fractal network of branches with local (2 x 2) symmetry. Annealing of the obtained structure at 300 °C yielded a smooth surface with very well ordered regions showing (2 x 2) periodicity and clean Pd(III) areas. This result indicates that the p(2 x 2) vanadium oxide is indeed the most stable one. The ordered p(4 x 4) phase, however, was found to homogeneously cover the whole surface at a V-coverage of 0.31 ML and was structurally analyzed by quantitative LEED and DFT. The resulting atomic structure showed very special features, namely vanadium atoms being surrounded by 4 oxygen atoms in an unusual tetrahedral coordination, in contrast to the regular octahedral coordination observed in most of the bulk vanadium oxides. The whole p(4 x 4) structure, which was found to be of V<sub>5</sub>O<sub>14</sub> stoichiometry, can be build up by simply connecting such tetrahedral building blocks to a hexagonal ring. This changed preferential coordination of vanadium is solely caused by the interaction between oxide and substrate, which now enables the construction of one-dimensional chain-like structures. Taking this result into account, it is possible to explain the observed, non-periodic, low coverage phases as being composed of the same tetrahedral building blocks. Also simple "nanostructures", that were observed in the p(2 x 2)-V<sub>2</sub>O<sub>3</sub> phase after preparation in the above described way, could be described by combining 5 tetrahedral units with the regular V<sub>2</sub>O<sub>3</sub> structure.

Generally speaking, the demonstrated possibility to stabilize unconventional oxide

structures, that show no resemblance to known bulk oxides, at metal surfaces seems to be a very interesting and important field of research, since it could give new insights into the processes involved in real catalysts and/or even help to design new, more efficient ones. The catalytic activity of the unusual, tetrahedrally coordinated vanadium oxide structures, for instance, is still completely unknown and requires further investigations.

## 8 Appendix

### 8.1 Image processing macro

As described in Sec. 2.2.4 the macro LEED macro `tmp` was written in order to improve the quality of LEED measurements, by reducing the negative effects of imperfections of the set-up (LEED optics, CCD camera). At first appropriate *dark frame* and *flat field* images have to be created (cf. Sec. 2.2.4). The best results are usually achieved if several similar images are averaged, therefore a function called `Mitteln` is included in the marco, which simply averages over a given number of equivalent pictures and saves the resulting image as a TIFF-file named `bild.tif`.

```
macro 'Mitteln';

var
  i,n,m,iter,inner: integer;
  bild,bild1,bild2,bildinner: integer;
  str: string;
  extra,extraold: boolean;

begin
  n := GetNumber('Anzahl der Bilder: ',4,0);
  for i:=1 to n do begin
    PutMessage('Bild ',i,' waehlen!');
    Open(' ');
    if i=1 then bild := PidNumber;
    str := concat('bild',i,' - pid: ',PidNumber);
    SetPicName(str);
  end;
  iter := trunc(ln(n)/ln(2));
  inner := trunc(n/2);
  extraold := FALSE;
  extra := FALSE;
  if odd(n) then extra := TRUE;
  for m:=1 to iter do begin
    for i:=1 to inner do begin
      str := concat('bild', (2*i-1),'+',(2*i),'-',m);
      bild1 := bild-(2*i)+2;
      bild2 := bild-(2*i)+1;
      if ((extraold=TRUE) AND (i=inner) AND (extra=FALSE)) then bild2 := bild2-1;
      ImageMath('add',bild1,bild2,0.5,0,str);
      if i=1 then bildinner := PidNumber;
    end;
    bild1:=PidNumber;
    bild2:=bild2-1;
    if (extraold=TRUE) then bild2:=bild2-1;
    if extra=TRUE then begin
      ImageMath('add',bild1,bild2,0.5,0;bonusbild') ;
    end;
    extraold:=extra;
    extra := FALSE;
    if odd(inner) then extra := TRUE;
    inner := trunc(inner/2);
    bild:=bildinner;
  end;
end;
```

```

end;
SetSaveAs('TIFF');
SaveAs('bild.tif');
DisposeAll;
end;

```

In order to be able to run the actual image processing macro called LEED Bildbearbeitung, several pre-conditions have to be fulfilled. First of all, a mask file (the same as the one used for the regular LEED macro) has to be located in the same directory as the LEED image stack. Second of all, the recorded LEED images have to be named `tmpenergy.0.tif`, where *energy* stands for the electron energy of the actual image - this is usually accomplished by running the data evaluation macro once. Third of all, a destination directory labeled `mod` has to exist in the directory of the LEED images. Finally, a *dark frame* and a *flat field* image are required in order to be able to process the images in the way described in Sec. 2.2.4. The starting factor (i.e. a constant multiplier applied to the final images) asked by the program should be sufficiently high (at least higher than the saturation value - e.g. 128) in order to obtain the highest possible resolution, since in this case a second run is started, where the best value is automatically chosen.

```

{ LEED Bildbearbeitung vs. flat-screen }

function modflat(d,f,m,mi: integer): integer;

var
maskint, dminf, dminfmask: integer;

begin
ChoosePic(m);
MultiplyByConstant(0.003921568627451);
maskint := PidNumber;
ImageMath('sub real',d,f,1.0,0,'dark-flat');
dminf := PidNumber;
ImageMath('mul real',dminf,dminf,maskint,1.0,0,'(dark-flat)*mask');
dminfmask := PidNumber;
ImageMath('add real', dminfmask, mi, 1.0, 0, 'modflat');
modflat := PidNumber;
ChoosePic(maskint);
Dispose;
ChoosePic(dminf);
Dispose;
ChoosePic(dminfmask);
Dispose;
end;

macro 'LEED Bildbearbeitung';
var
dark, flat, mask, maskinv, pixel, bild, bild2, bild3, daflma, result, endresult, resultm: integer;
i, size, factor: integer;
Pfad,str,file,type: string;
r, n, mean, most, min, max, realmax: real;
begin
PutMessage('Bitte Maske auswaehlen!');

```

```

Open('');
Pfad := GetPath('window');
ShowMessage('Pfad: ',Pfad);
mask := PidNumber;
Duplicate('Maske inv');
Invert;
maskinv := PidNumber;
PutMessage('Bitte Darkscreen auswaehlen! ');
str := concat(Pfad, 'dark.tif');
Open(str);
dark := PidNumber;
PutMessage('Bitte Flatscreen auswaehlen!');
str := concat(Pfad, 'flat.tif');
Open(str);
flat := PidNumber;
SetNewSize(592,567);
MakeNewWindow('pixel.tif');
Invert;
PutPixel(0,0,0);
pixel := PidNumber;

factor := GetNumber('Starting factor: ',128,0);

NewTextWindow('log',300,200);
MoveWindow(800,200);
daflma := modflat(dark,flat,mask,maskinv);

repeat
  realmax := 255.0;
  r := 0.0;
  file := concat(Pfad,'tmp',r:4:1,'.tiff');
  GetFileInfo(file,type,size);
  while ((size < 1) AND (r < 500.0)) do begin
    r := r + 1;
    file := concat(Pfad,'tmp',r:4:1,'.tiff');
    GetFileInfo(file,type,size);
  end;
  if (r=500.0) then PutMessage('Error 27: Benoetige tmp-Files!!');
  SelectWindow('log');
  Writeln('');
  Writeln('Factor: ',factor);

while size > 0 do begin
  Open(file);
  bild := PidNumber;
  ImageMath('sub real',dark,bild,1.0,0,'dark-bild');
  bild2 := PidNumber;
  ImageMath('div real',bild2,daflma,factor,10,'(dark-bild)/darkflatmask');
  bild3 := PidNumber;

  SelectPic(bild3);
  Measure;
  GetResults(n,mean,most,min,max);
  if (cValue(max) > 255.0) then
  begin
    SelectWindow('log');
    Writeln('Energy: ',r:4:1,' eV - max: ',cValue(max):4:1);

    if (cValue(max) > realmax) then realmax := cValue(max);
  end;
  ImageMath('max real', bild3, maskinv,1.0,0,'result');

```

```

result := PidNumber;
ImageMath('min real', result, pixel, 1.0, 0, 'result mod');
resultm := PidNumber;
SelectPic(resultm);
Invert;
SetSaveAs('TIFF');
str := concat(Pfad, 'mod:tmp', r:4:1, '.tiff');
SaveAs(str);
ChoosePic(bild);
Dispose;
ChoosePic(bild2);
Dispose;
ChoosePic(bild3);
Dispose;
ChoosePic(result);
Dispose;
ChoosePic(resultm);
Dispose;
r:=r+1;
file := concat(Pfad, 'tmp', r:4:1, '.tiff');
GetFileInfo(file, type, size);
end;
factor := trunc((245.0/(realmax-10.0))*factor);

until realmax=255.0;

SelectWindow('log');
Save;
Dispose;
DisposeAll;
end;

```

Since the automatically adjusted contrast of NIH-image can cause some problems for the subsequent data evaluation of the processed image stack, another function named *Referenzbild* is included in the image processing macro. This function simply inverts the white border area of a given reference image and stores a backup copy of the original image as *filename*, orig.

```

macro 'Referenzbild';

var
  bild, maske, erg: integer;
  Pfad, str, filename: string;

begin
  PutMessage('Bitte Referenzbild auswaehlen!');
  Open('');
  Pfad := GetPath('window');
  ShowMessage('Pfad: ', Pfad);
  bild := PidNumber;
  SelectPic(bild);
  filename := WindowTitle;
  str := concat(Pfad, filename, '.orig');
  SetSaveAs('TIFF');
  SaveAs(str);
  str := concat(Pfad, 'maske');
  PutMessage('Bitte Maske auswaehlen!');

```

```
Open(str);
maske := PidNumber;
  Invert;
  ImageMath('add',maske,bild1.0,0,filename) ;
  erg := PidNumber;
SelectPic(erg);
  str := concat(Pfad,filename);
SaveAs(str);
  DisposeAll;
end;
```

## Bibliography

- [1] G. Ertl, H. Knözinger, J. Weitkamp, *Handbook of heterogeneous catalysis*, Wiley, New York, 1997.
- [2] V. E. Henrich, P. A. Cox, *The Surface Science of Metal Oxides*, Cambridge University Press, Cambridge, 1994.
- [3] S. Tauster, S. Fung, R. Garden, *J. Am. Chem. Soc.* 100 (1978) 170.
- [4] S. M. Vesecky, D. R. Rainer, D. W. Goodman, *J. Vac. Sci. Technol. A* 14 (1996) 1457.
- [5] M. Lyubovsky, L. Pfefferle, *Catal. Today* 47 (1999) 29.
- [6] S. Ladas, R. Imbihl, G. Ertl, *Surf. Sci.* 219 (1989) 88.
- [7] M. R. Bassett, R. Imbihl, *J. Chem. Phys.* 93 (1990) 811.
- [8] V. Bondzie, P. Kleban, D. A. Browne, *J. Vac. Sci. Technol. A* 11 (1993) 1946.
- [9] V. A. Bondzie, P. Kleban, D. J. Dwyer, *Surf. Sci.* 347 (1996) 319.
- [10] H. Bosch, F. Janssen, *Catal. Today* 2 (1988) 369.
- [11] G. C. Bond, S. F. Tahir, *Appl. Catal.* 71 (1991) 1.
- [12] C. Davisson, L. Germer, *Nature* 119 (1927) 558.
- [13] J. B. Pendry, *Low Energy Electron Diffraction*, Academic, London, 1974.
- [14] S. Y. Tong, *Prog. Surf. Sci.* 7 (1975) 1.
- [15] J. B. Pendry, *J. Phys. C: Solid State Phys.* 13 (1980) 937.
- [16] E. Zanazzi, F. Jona, *Surf. Sci.* 62 (1977) 61.
- [17] P. J. Rous, J. B. Pendry, D. K. Saldin, K. Heinz, K. Müller, N. Bickel, *Phys. Rev. Lett.* 57 (1986) 2951.
- [18] P. J. Rous, *Prog. Surf. Sci.* 39 (1992) 3.
- [19] E. Platzgummer, *Die thermische Segregation an Pt-(d-Metall) Legierungen im Wechselspiel mit strukturellen Veränderungen*, Ph.D. thesis, TU-Wien, 1999.
- [20] C. Buil, *CCD Astronomy*, Willmann-Bell, Richmond, 1991.
- [21] M. A. Van Hove, W. H. Weinberg, C.-M. Chan, *Low-Energy Electron Diffraction*, Springer Verlag, Berlin, 1986.

- [22] B. Lippman, J. Schwinger, Phys. Rev. **79** (1950) 469.
- [23] R. Koller, Y. Gauthier, C. Klein, M. DeSantis, M. Schmid, P. Varga, Surf. Sci. **530** (2003) 121.
- [24] V. Blum, L. Hammer, W. Meier, K. Heinz, Surf. Sci. **488** (2001) 219.
- [25] M. Sporn, E. Platzgummer, E. L. D. Gruber, M. Schmid, W. Hofer, P. Varga, Surf. Sci. **416** (1998) 423.
- [26] P. J. Rous, J. B. Pendry, Surf. Sci. **219** (1989) 355.
- [27] M. A. Van Hove, W. Moritz, H. Over, P. J. Rous, A. Wander, A. Barbieri, N. Materer, U. Starke, G. A. Somorjai, Surf. Sci. Rep. **19** (1993) 191.
- [28] V. Blum, K. Heinz, Comp. Phys. Comm. **134** (2001) 392.
- [29] P. J. Rous, J. B. Pendry, Comput. Phys. Commun. **54** (1989) 137.
- [30] P. J. Rous, J. B. Pendry, Comput. Phys. Commun. **54** (1989) 157.
- [31] U. Löffler, R. Döll, K. Heinz, J. B. Pendry, Surf. Sci. **301** (1994) 346.
- [32] Y. Gauthier, Y. Joly, R. Baudoing, J. Rundgren, Phys. Rev. B **31** (1985) 6216.
- [33] R. Baudoing, J. R. Y. G. M. Lundberg, J. Phys. Chem. **19** (1986) 2825.
- [34] S. Crampin, P. J. Rous, Surf. Sci. **244** (1991) L137.
- [35] R. Döll, M. Kottcke, K. Heinz, Phys. Rev. B **48** (1993) 1973.
- [36] K. Heinz, R. Döll, M. Kottcke, Surf. Rev. Lett. **3** (1996) 1651.
- [37] E. Platzgummer, M. Sporn, R. Koller, M. Schmid, W. Hofer, P. Varga, Surf. Sci. **453** (2000) 214.
- [38] V. Blum, L. Hammer, W. Meier, K. Heinz, M. Schmid, E. Lundgren, P. Varga, Surf. Sci. **474** (2001) 81.
- [39] M. Kottcke, K. Heinz, Surf. Sci. **376** (1997) 352.
- [40] P. J. Rous, Surf. Sci. **296** (1993) 358.
- [41] M. Schmid, *Experimentelle Methoden der Oberflächenphysik*, lecture script, TU Wien, 2001.
- [42] J. Tersoff, D. R. Hamann, Phys. Rev. B **31** (1985) 805.
- [43] P. Sautet, Surf. Sci. **374** (1997) 406.

- [44] C. Klein, A. Eichler, E. L. D. Hebenstreit, G. Pauer, R. Koller, A. Winkler, M. Schmid, P. Varga, *Phys. Rev. Lett.* **90** (2003) 176101.
- [45] J. Tersoff, D. R. Hamann, *Phys. Rev. Lett.* **50** (1983) 1998.
- [46] T. Carlson, *Photoelectron and Auger Spectroscopy*, Plenum Press, New York, 1975.
- [47] B. E. Warren, *X-Ray Diffraction*, Addison-Wesley, Reading, 1969.
- [48] R. Feidenhans'l, *Surf. Sci. Rep.* **10** (1989) 105.
- [49] I. K. Robinson, in: *Handbook on synchrotron radiation*, North-Holland, Amsterdam, 1991.
- [50] A. Biedermann, *Nanostruktur der Eisenoberfläche*, Ph.D. thesis, TU-Wien, 1995.
- [51] R. Baudoing-Savois, M. DeSantis, M. C. Saint-Lager, P. Dolle, O. Geaymond, P. Taunier, P. Jeantet, J. P. Roux, G. Renaud, A. Barbier, O. Robach, O. Ulrich, A. Mougín, G. Bérard, *Nucl. Instr. Meth. Phys. Res. B* **149** (1999) 213.
- [52] G. Zheng, E. I. Altman, *Surf. Sci.* **462** (2000) 151.
- [53] H. Conrad, G. Ertl, J. Küppers, E. E. Latta, *Surf. Sci.* **65** (1977) 245.
- [54] D. L. Weissman-Wenocur, M. L. Shek, P. M. Stefan, I. Lindau, W. E. Spicer, *Surf. Sci.* **127** (1983) 513.
- [55] F. P. Leisenberger, G. Koller, M. Sock, S. Surnev, M. G. Ramsey, F. P. Netzer, B. Klötzer, K. Hayek, *Surf. Sci.* **445** (2000) 380.
- [56] A. Steltenpohl, N. Memmel, *Surf. Sci.* **443** (1999) 13.
- [57] A. Seitsonen, Y. D. Kim, S. Schwegmann, H. Over, *Surf. Sci.* **468** (2000) 176.
- [58] E. H. Voogt, A. J. M. Mens, O. L. J. Gijzeman, J. W. Geus, *Surf. Sci.* **373** (1997) 210.
- [59] E. Lundgren, G. Kresse, C. Klein, M. Borg, J. N. Andersen, M. D. Santis, Y. Gauthier, C. Konvicka, M. Schmid, P. Varga, *Phys. Rev. Lett.* **88** (2002) 246103.
- [60] H. Over, Y. D. Kim, A. Seitsonen, S. Wendt, E. Lundgren, M. Schmid, P. Varga, A. Morgante, G. Ertl, *Science* **287** (2000) 1474.
- [61] M. Bäumer, H.-J. Freund, *Prog. Surf. Sci.* **61** (1999) 127.
- [62] C. I. Carlisle, D. A. King, M.-L. Bocquet, J. Cerda, , P. Sautet, *Phys. Rev. Lett.* **84** (2000) 3899.

- [63] R. Koller, W. Bergermyer, G. Kresse, C. Konvicka, M. Schmid, J. Redinger, R. Podloucky, P. Varga, *Surf. Sci.* 512 (2002) 16.
- [64] R. Imbihl, J. E. Demuth, *Surf. Sci.* 173 (1986) 395.
- [65] H. Over, *Prog. Surf. Sci.* 58 (1998) 249.
- [66] B. Klötzer, K. Hayek, C. Konvicka, E. Lundgren, P. Varga, *Surf. Sci.* 482 (2001) 237.
- [67] G. Kresse, J. Furthmüller, *Phys. Rev. B* 54 (1996) 11169.
- [68] G. Kresse, J. Furthmüller, *Comput. Mater. Sci.* 6 (1996) 15.
- [69] G. Kresse, D. Joubert, *Phys. Rev. B* 59 (1998) 1758.
- [70] J. P. Perdew, J. A. Chevary, S. H. Vosko, K. A. Jackson, M. R. Pederson, D. J. Singh, C. Fiolhais, *Phys. Rev. B* 46 (1992) 6671.
- [71] E. Vlieg, *J. Appl. Crystallogr.* 33 (2000) 401.
- [72] E. Vlieg, *J. Appl. Crystallogr.* 31 (1998) 198.
- [73] J. Katana-Ngala, P. Y. Zavalij, M. S. Whittingham, *Solid State Chemistry of Inorganic Materials III. Symposium Materials Research Society Symposium Proceedings* 658 (2001) 9.16-1.
- [74] C. Baratto, G. Sberveglieri, I. Ricco, *Chemical and Biological Sensors and Analytical Methods II Proceedings of the International Symposium of the Electrochemical Society* 1 (2001) 470.
- [75] S. Surnev, G. Kresse, M. Sock, M. G. Ramsey, F. P. Netzer, *Surf. Sci.* 495 (2001) 91.
- [76] S. A. Chambers, *Surf. Sci. Rep.* 39 (2000) 105.
- [77] S. Surnev, G. Kresse, M. G. Ramsey, F. Netzer, *Phys. Rev. Lett.* 87 (2001) 86102.
- [78] S. Surnev, L. Vitali, G. Kresse, J. Hafner, M. G. Ramsey, F. P. Netzer, *Phys. Rev. B* 61 (2000) 13945.
- [79] G. Kresse, S. Surnev, M. G. Ramsey, F. Netzer, *Surf. Sci.* 492 (2001) 329.
- [80] S. Surnev, J. Schoiswohl, G. Kresse, M. G. Ramsey, F. P. Netzer, *Phys. Rev. Lett.* 89 (2002) 246101.
- [81] C. Nagl, O. Haller, E. Platzgummer, M. Schmid, P. Varga, *Surf. Sci.* 321 (1994) 237.

- [82] C. Klein, G. Kresse, S. Surnev, F. Netzer, M. Schmid, P. Varga, *Phys. Rev. B.* (2003) submitted.
- [83] G. Kresse, W. Bergermyer, R. Podlucky, E. Lundgren, R. Koller, M. Schmid, P. Varga, *Appl. Phys. A* 76 (2003) 701.
- [84] S. Surnev, M. Sock, G. Kresse, J. Andersen, M. G. Ramsey, F. P. Netzer, *J. Phys. Chem. B* (2003) in press.

## Acknowledgements

Zuallererst möchte ich mich bei Prof. Dr. *Peter Varga* für die Möglichkeit bedanken diese außerordentlich interessante Arbeit durchführen zu können. Dies wäre mir allerdings sicherlich nicht so leicht von der Hand gegangen, wenn das von ihm etablierte Arbeitsklima nicht derart freundschaftlich und motivierend gewesen wäre, was mir weiteren Dank abverlangt. In diesem Zusammenhang sei auch die stets vorhandene Versorgung mit Kaffee von ausgezeichneter Qualität positiv erwähnt, die sicherlich einen nicht unbedeutenden Einfluss auf die Aufrechterhaltung meiner Arbeitskraft hatte - eine taktische Meisterleistung...

Besonders bedanken möchte ich mich des Weiteren bei Prof. Dr. *Michael Schmid* für seine unerläßliche Hilfestellung bei jeglicher Art von Problemen. Seinem oftmals schon gespenstisch anmutenden Fachwissen in allen(!) Bereichen ist es zu verdanken, dass auch wirklich alle Hürden genommen werden konnten.

Prof. Dr. *Wilhelm Hofer* gehört mein Dank für seine bereitwillige Hilfe bei allen EDV-spezifischen Problemen und seinen unentbehrlichen Beitrag zur Aufrechterhaltung der Funktionstüchtigkeit des Netzwerks. Systeme mit vergleichbarer Datensicherheit gibt es aller Wahrscheinlichkeit nach sonst nur in Banken.

Für die Einführung in die Kunst der LEED-Analyse möchte ich mich ganz besonders bei meinem ehemaligen Kollegen Dr. *Robert Koller* bedanken. Seine Unterstützung bei meinen ersten Gehversuchen im reziproken Raum bewahrte mich vor einem möglicherweise recht schmerzhaften Sturz auf die Nase.

Auch Dr. *Christoph Konvicka* sei an dieser Stelle gedankt und zwar nicht nur wegen der Bereitstellung diverser wunderschöner STM Bilder, sondern auch auf Grund der Tatsache, dass ich ohne ihn wahrscheinlich nicht mit dem Kite-surfing angefangen hätte.

Meinem Kollegen und Weggefährten DI *Rupert "Berti" Tscheließnig* gebührt ein nicht unerhebliches Maß an Dankbarkeit unter anderem für die Möglichkeit bei einigen Nachbesprechungen diverse physikalische und private Problemstellungen diskutieren zu können.

Einen wesentlich Beitrag zu dem ausgezeichneten Betriebsklima in der Arbeitsgruppe leisteten auch meine Kollegen Dr. *Albert Biedermann*, DI *Christina Fritscher*, DI *Evelyn Napetschnig*, DI *Hannes Schiechl* und die zwei DIs in spe *Werner Rupp* und *Christoly Biely*, wofür ich wirklich sehr dankbar bin. Im Besonderen muss ich Christoly dafür

danken, dass er mein in mir schlummerndes Interesse am Klettern geweckt hat.

Prof. Dr. *Georg Kresse* vom Institut für Materialphysik der Universität Wien gebührt wahrlich ein sehr großer Anteil meiner Dankbarkeit, denn ohne die Unterstützung durch seine theoretischen Berechnungen wäre ein Großteil dieser Arbeit wohl deutlich schwieriger, wenn nicht gar unmöglich, gewesen.

Für ihre unabdingbare Hilfestellung bei der Durchführung der Röntgenbeugungsexperimente am ESRF in Grenoble danke ich ganz besonders Dr. *Maurizio De Santis* und Dr. *Yves Gauthier*. Auch die Zusammenarbeit mit Dr. *Edvin Lundgren* von der University of Lund und Dr. *Svetlozar Surnev* von der Karl-Franzens-Universität in Graz sei hier dankend erwähnt.

Außerdem möchte ich mich an dieser Stelle recht herzlich bei der Erlanger LEED-Fraktion unter der Leitung von Prof. Dr. *Klaus Heinz* für die zur Verfügungstellung des TensErLEED Programmpakets bedanken, ohne welches die in dieser Arbeit präsentierten Resultate nicht zu Stande gekommen wären. In diesem Zusammenhang sei auch dem *zentralen Informatikdienst* der TU Wien für die Bereitstellung der benötigten Rechenzeit gedankt, sowie dem *Fonds zur Förderung der wissenschaftlichen Forschung* für die Finanzierung dieses Projekts.

Auf das Allerherzlichste möchte ich mich bei meiner Familie für die immerwährende Unterstützung jeglicher Art bedanken, die es mir ermöglichte mich, stets hoch motiviert, vollständig auf meine Arbeit zu konzentrieren. Auch all meinen Freunden möchte ich hiermit meinen tief empfundenen Dank aussprechen für die größeren und kleineren, angenehmen Ablenkungen, die mir halfen mit einem freien, klaren Kopf in die Woche zu starten.

# Resume

## Personal data:

Name: Christof Klein  
Date of birth: 16<sup>th</sup> of July 1974 in Vienna  
Citizenship: Austrian  
Address: Bastiengasse 40/9  
1180 Wien

## Educational data:

1980 - 1981 Elementary school in Birgitz, Tyrol  
1981 - 1984 Elementary school in Vienna, Scheibenbergstraße  
1984 - 1992 High school in Vienna, BRG-19, Krottenbachstraße  
June 1992 Matura, passed with distinction

Oct. 1992 - May 1999 Vienna University of Technology, Physics  
March 1995 1. Diploma examination  
Apr. 1998 - Feb. 1999 Diploma thesis at the Atomic Institute of the  
Austrian Universities:  
*"Kritische Ströme in U-dotierten Bändern des  
Hochtemperatursupraleiters  $\text{Bi}_2\text{Sr}_2\text{Ca}_2\text{Cu}_3\text{O}_x$ "*  
May 1999 2. Diploma examination, passed with distinction

Nov. 2000 - June 2003 Research assistant at the  
Institut für Allgemeine Physik,  
Vienna University of Technology

## Military service:

Sep. 1999 - April 2000 Großmittel, Lower Austria